UNIVERSITÀ DEGLI STUDI DI PADOVA

Dipartimento di Fisica e Astronomia "Galileo Galilei"

Master Degree in Physics

Final Dissertation

Quantum correlations in two-dimensional flux-frustrated lattices with tunable dimerization

Thesis supervisor

Prof. Marco Di Liberto

Thesis co-supervisor

Dr. Lorenzo Maffi

Candidate

Giovanni Bartolucci

Academic Year 2025/2026

Abstract

Models with synthetic gauge fields are central in the development of quantum simulators as they allow to study classes of nontrivial correlated states with broken time-reversal symmetry, as for the case of the long-sought fractional Quantum Hall state. Recent experiments have shown the first steps in this direction with the observation of vortex and Meissner phases with nonvanishing current patterns in the ground state. In recent theoretical studies, vortex phases have also been shown to appear spontaneously via an interaction mediated mechanism that relies on a strong lattice dimerization and onsite interactions. Here we will study the effect of quantum correlations beyond the strongly-dimerized limit construction to identify the impact of emergent processes driven by interactions on the quantum phases.

Index

Chapter 1

Introduction to quantum simulation

The traditional study of interacting quantum systems is fundamentally constrained by the difficulty of capturing long-range quantum correlations. Exact diagonalization methods are limited by the exponential growth of the Hilbert space, and even advanced numerical methods, while powerful in specific regimes, struggle when entanglement becomes extensive or when the relevant physics is intrinsically two- or three-dimensional [1]. These limitations are particularly severe for phases whose defining properties are nonlocal, such as topological states of matter, where long-range order is encoded in global invariants [2] rather than conventional symmetry breaking [3].
Quantum simulation offers a complementary route to access these regimes. By engineering highly controllable quantum platforms, one can reproduce the dynamics of target models under conditions in which geometry, interactions, and gauge fields are tuned with precision. Such systems make it possible to directly probe correlated and topological phenomena, even when classical approaches cannot reliably capture the underlying long-range structure.
Topological phases are especially interesting because their defining properties are protected from local perturbations, and this robustness underlies proposals for fault-tolerant quantum computation [4]. It is also compelling from a fundamental perspective: the persistence of quantum coherence and nonlocal order at macroscopic scales provides insight into how quantum phenomena can remain stable in real materials and under realistic conditions. The hallmark example of topological phase is the Quantum Hall effect [5], which emerges in two-dimensional electron gases under strong magnetic fields, displays quantized transverse conductance, and hosts chiral edge states that are insensitive to disorder.
Neutral atoms in optical lattices have become a promising platform for quantum simulation of many-body quantum systems [6], including lattice analogues of the Quantum Hall effect, as they allow the engineering of synthetic magnetic fields far beyond what is achievable in solid-state systems. In these experiments, periodic light potentials are used to trap the atoms in highly controllable geometries that can be regarded as a "synthetic crystal" made of light. This setup provides a clean environment where the fundamental parameters of the target model, such as the lattice geometry and the strength of particle interactions, can be tuned with a level of precision that is impossible in traditional materials. The resulting systems are accurately described by Hubbard-type models, in particular the Bose-Hubbard model [7], which provides the standard theoretical framework for interacting bosons on a lattice. To provide a formal definition of the Bose-Hubbard model as a starting point of this thesis we describe here its Hamiltonian,

$$\hat{H} \;=\; -t \sum_{\langle i,j \rangle} \big(\hat{b}_i^\dagger \hat{b}_j + \text{h.c.} \big) \;+\; \frac{U}{2} \sum_i \hat{n}_i (\hat{n}_i - 1) \;-\; \mu \sum_i \hat{n}_i \,. \tag{1.1}$$

Each term in this equation represents a specific physical process within the lattice.
The creation operator, $\hat{b}_i^\dagger$ adds a boson to site i, while the annihilation operator $\hat{b}_j$ removes one from

site j. They obey the standard bosonic commutation relations. The first term describes nearest-neighbor hopping processes and is characterized by the amplitude t. The hopping amplitude t represents the kinetic energy of the system, and determines the probability amplitude for a particle to "hop" between nearest-neighbor sites $\langle i, j \rangle$. The second term describes local interactions, where U is the on-site interaction strength and $\hat{n}_i = \hat{b}_i^\dagger \hat{b}_i$ is the number operator. Finally, the last term containing the chemical potential μ, controls the total number of particles in the system.

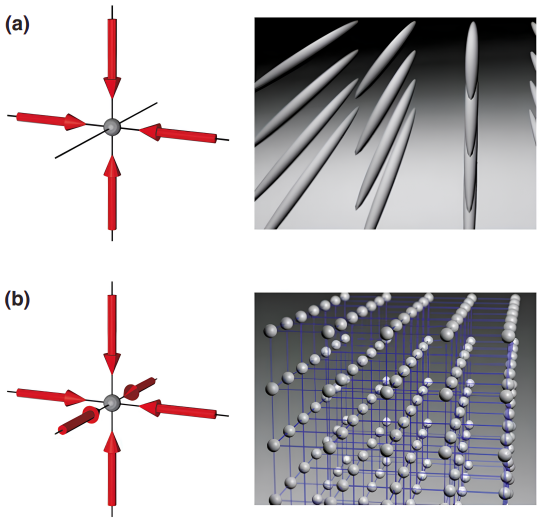

Figure 1.1: Schematic of 2D and 3D optical lattices. (a) A two-dimensional optical lattice created by superimposing two orthogonal standing waves, which confines atoms into an array of one-dimensional potential tubes. (b) A three-dimensional simple cubic lattice generated by three pairs of counter-propagating laser beams. In the limit of deep lattices, each site can be approximated by a harmonic oscillator potential, providing a clean and controllable environment for studying many-body quantum phases. Source: ([8], upscaled).

The theoretical foundation for realizing the Bose-Hubbard model in a laboratory setting was established by Jaksch et al. in 1998 [9], who proposed that ultracold bosonic atoms trapped in the periodic potential of an optical lattice would closely emulate the Hamiltonian's dynamics. When two counter-propagating laser beams of the same frequency and polarization overlap, they form a standing wave. Through the AC Stark effect, the oscillating electric field of the laser induces a dipole moment in the neutral atoms. This results in a conservative potential, the optical lattice (as shown in Fig. 1.1, where the atoms are drawn to either the intensity maxima or minima depending on the detuning of the laser frequency relative to the atomic resonance. The laser intensity is directly proportional to the lattice depth and, in turn, to the ratio U/t. This proposal was remarkably realized in the groundbreaking experiment by Greiner et al. in 2002 [10]. By creating a three-dimensional lattice with counter-propagating laser beams and tuning the lattice depth they observed the quantum phase transition from a coherent superfluid to a Mott insulator. In the superfluid phase the atoms are delocalized across the lattice, while in a Mott insulating regime the strong on-site interactions (U) dominate over the kinetic hopping (t), fixing an integer number of atoms on each site. This breakthrough paved the way to a new generation of optical-lattice experiments [8] that now serve as a central platform for exploring strongly correlated quantum matter.

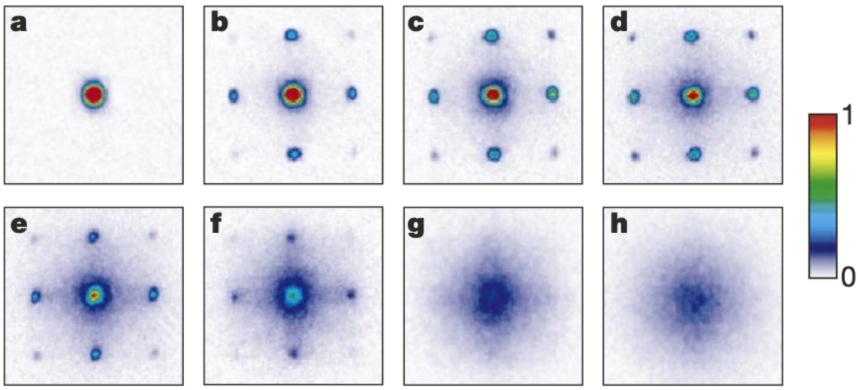

Figure 1.2: Time-of-flight absorption images taken after releasing atoms from a 3D optical lattices of varying depths. Potential depths range from (a) $0\,E_r$ to (h) $20\,E_r$. (a-c) In the superfluid regime, the system possesses long-range phase coherence, resulting in sharp, high-contrast interference peaks after time-of-flight expansion. (d-h) As the lattice depth increases, on-site interactions (U) begin to dominate over tunneling (t). The interference pattern gradually "melts" and disappears, signaling the loss of phase coherence and the entry into the Mott insulating phase, where atoms are localized at individual lattice sites. Source:([10]).

While the standard Bose-Hubbard model already captures a broad range of quantum behaviors, extending the capabilities of optical lattices to more interesting regimes requires, for example, introducing the effects of electromagnetism. Because neutral atoms, unlike electrons, do not couple to external magnetic fields, an artificially simulated magnetic field is needed to study charge-like dynamics. In experimental settings, these synthetic gauge fields are generated through techniques such as laser-assisted tunneling , Raman coupling, or Floquet modulation [11–13]. In the latter case, a rotating reference frame induces a Coriolis force that mimics the Lorentz force acting on charged particles. Because this effective "magnetic field" governs the motion of neutral atoms despite their lack of electric charge, it is referred to as an artificial magnetic field. From a theoretical perspective, the primary consequence of introducing these gauge fields into the lattice is the breaking of time-reversal symmetry, an effect that has profound relevance for the emergence of topology in quantum matter, in particular for Quantum Hall states.

Within the broad landscape of artificial gauge fields, this thesis focuses mainly on a particularly simple and symmetric configuration: a lattice threaded by exactly half a magnetic flux quantum (a π-flux) per elementary plaquette. This setup is uniquely intriguing because the microscopic Hamiltonian with π-flux does not explicitly break time-reversal symmetry. Instead, the phase pattern can be chosen such that the Hamiltonian remains real, even though the system still experiences an effective magnetic field. The addition of on-site interactions to the geometrically frustrated π-flux background dramatically alters the system behavior and opens up to the possibility of spontaneous time-reversal symmetry breaking, giving rise to chiral order. Recent studies have connected this emergent chirality to the appearance of p-band physics at low-energy [14]. Particles are promoted into orbital configurations that mimic the behavior of excited p-states, characterized by intrinsic angular momentum. In this specific lattice context, the stabilized angular momentum directly translates into the spontaneous generation of chiral currents, a necessary ingredient to realize topological behavior. Capturing such physics is remarkable, as genuine p-band phenomena are typically inaccessible in conventional quantum gases due to the short lifetime of excited states, which usually decay before stable many-body effects can manifest [15].

The remainder of the present work is structured into the following three main parts.

Chapter 2 provides the theoretical background. We detail Peierls substitution [16], the mathematical framework to implement a magnetic field on a lattice, illustrate standard gauge choices for the Peierls phases and demonstrate how a finite flux different from π induces the explicit breaking of

time-reversal symmetry. We study the flux-frustrated Bose-Hubbard model and survey some of its known many-body phases, such as the Meissner, Vortex, Charge-Density Wave and Biased-Ladder phases [17, 18]. Finally this chapter reviews the classification of topological phases of matter, ultimately establishing their connection with the model under study, specifically the lattice adaptations of Quantum Hall states.

Moving from the general to the specific, chapter 3 analyzes the core building block of our system: the two-plaquette Benalcazar-Bernevig-Hughes (BBH) [19] cluster. By employing exact diagonalization, we explore the many-body spectrum at half filling and the properties of the ground state as on-site interactions are increased within the weak regime. We identify peculiar non-monotonic behavior of the observables due to many-body effects. Then, we systematically construct two low-energy effective theories with different degrees of complexity, and compare them to show how the non-perturbative treatment of coupling between plaquettes qualitatively recovers the important features observed for the exact diagonalization of the full theory.

The final chapter extends the exact local physics of the isolated cluster to the thermodynamic limit by defining an infinite two-plaquette ladder. Employing a two-plaquette cluster Gutzwiller ansatz [20], we assess whether the local structural and chiral features observed for the studied building block survive in its macroscopic extension. We reconstruct the phase diagram as a function of the on-site interaction in both weak and balanced inter-cluster coupling regimes, detailing the transition from chiral superfluids to chiral Mott insulators. We conclude with a summary of the main results of the chapter, which hint to the presence of a non-trivial superfluid phase in which chiral currents exhibit non-monotonic behavior while the density of bosons gets redistributed within the ladder.

Chapter 2

Synthetic gauge fields in quantum lattice models

The effect of synthetic gauge fields can be integrated into the Bose-Hubbard model by attaching Peierls phases to the hopping coefficients, which carry the dependence on the electromagnetic vector potential. As theorized by Aharonov and Bohm [21], and later confirmed by Tonomura's group [22], a charged wavefunction accumulates a phase equal to the line integral of the electromagnetic vector potential along its path $\mathcal{C}$:

$$\varphi_{\mathcal{C}} \;=\; \frac{q}{\hbar}\int_{\mathcal{C}} \vec{A}\cdot d\vec{\ell}, \tag{2.1}$$

where $\vec{A}$ is the vector potential and q the charge. This phase depends on the gauge choice for $\vec{A}$ and is therefore not directly observable. Instead, the interference between two paths enclosing a region S (in the case of interest, a plaquette $\square$) with magnetic flux Φ, produces a measurable phase difference,

$$\Delta\varphi \;=\; \frac{q}{\hbar}\oint_{\mathcal{C}} \vec{A}\cdot d\vec{\ell} \;=\; \frac{q}{\hbar}\iint_{S}(\nabla\times\vec{A})\cdot d\vec{S} \;=\; \frac{q}{\hbar}\iint_{S}\vec{B}\cdot d\vec{S} \;=\; \frac{q}{\hbar}\,\Phi_S\,, \tag{2.2}$$

accumulated along the closed contour $\mathcal{C}=\partial S$, the boundary of region S.
In a tight-binding lattice model, the continuum minimal coupling prescription $\vec{p}\to\vec{p}-q\vec{A}$ is implemented by the Peierls substitution [16, 23]. The amplitude t_{ij} of the hopping process between sites i and j is modified as follows:

$$t_{ij} \;\longrightarrow\; t_{ij}\,e^{\,\mathrm{i}A_{ij}}, \qquad \text{with} \quad A_{ij} \;=\; \frac{q}{\hbar}\int_{\vec{r}_i}^{\vec{r}_j}\vec{A}\cdot d\vec{\ell}. \tag{2.3}$$

The Peierls phases, A_{ij}, are not unequivocally defined: for a given configuration of the magnetic field, $\vec{B}$, there exist multiple equivalent expressions of the vector potential $\vec{A}$. A gauge choice is valid provided that:

- the Peierls phases reproduce the correct flux through every plaquette $\Phi_{\square}$, namely

$$\sum_{\langle i,j\rangle\in\square} A_{ij} \;=\; \frac{q}{\hbar}\iint_{\square}\vec{B}\cdot d\vec{S} \;=\; \frac{q}{\hbar}\Phi_{\square} \quad \forall \text{ plaquette } \square\,; \tag{2.4}$$

- reverse bonds carry opposite phase, such that the hopping terms produce a hermitian Hamiltonian:

$$A_{ji}=-A_{ij} \implies (t_{ij}e^{\mathrm{i}A_{ij}})^{\dagger}=t_{ji}e^{\mathrm{i}A_{ji}} \implies \hat{H}^{\dagger}=\hat{H}\,, \tag{2.5}$$

  provided that $t_{ji}=t_{ij}^{*}$;

- corresponds to a vector potential that varies smoothly over the lattice scale. For certain magnetic field profiles, a globally smooth gauge field cannot always be defined, and one must introduce branch cuts: lines across which the vector potential jumps by multiples of 2π. Since Peierls phases dictate particle hopping modulo 2π, these artificial discontinuities do not change the physical content of the system. While local gauge transformations allow one to arbitrarily reshape or move these branch cuts, their inherent existence is tied to global topological constraints. Specifically, on lattices with periodic boundary conditions or other topologically non-trivial geometries, the requirement of a single-valued many-body wavefunction imposes global flux restrictions. Consequently, the sum of the Peierls phases accumulated along any non-contractible loop $\mathcal{L}$ must satisfy

$$\sum_{\langle i,j\rangle\in\mathcal{L}} A_{ij} = \Theta_{\mathcal{L}} \quad (mod\ \ 2\pi)\,, \tag{2.6}$$

  where $\Theta_{\mathcal{L}}$ is the Aharonov-Bohm phase associated with the net magnetic flux threading the hole enclosed by $\mathcal{L}$. This construction is the lattice analogue of defining a smooth gauge field on a continuum manifold: local gauge freedom allows arbitrary rearrangements of phases on bonds, but global flux constraints enforced by the smoothness of the gauge field are necessary conditions for a physically meaningful structure;

- the magnetic unit cell determined by the given Peierls phases pattern is invariant under any lattice symmetry chosen to be preserved.

Under a local $U(1)$ gauge transformation of the site annihilation and creation operators,

$$\hat{b}_i \;\mapsto\; \hat{b}'_i \;=\; e^{\,\mathrm{i}\chi_i}\,\hat{b}_i\,, \qquad \hat{b}_i^\dagger \;\mapsto\; \hat{b}_i'^\dagger \;=\; e^{-\mathrm{i}\chi_i}\,\hat{b}_i^\dagger\,, \tag{2.7}$$

where χ_i is an arbitrary site-dependent gauge phase, the Peierls phases transform as

$$A_{ij} \mapsto A_{ij} + \chi_i - \chi_j\,, \tag{2.8}$$

in analogy with the continuum rule $\vec{A}(\vec{r}) \mapsto \vec{A}(\vec{r}) + \nabla\chi(\vec{r})$, where $\chi(\vec{r})$ is a scalar field.
For the physical flux through each plaquette to be gauge-invariant, the transformed Peierls phases must satisfy

$$\sum_{\langle i,j\rangle\in\square} (A_{ij} + \chi_i - \chi_j) \;=\; \sum_{\langle i,j\rangle\in\square} A_{ij}\,. \tag{2.9}$$

which holds modulo 2π for any choice of the local gauge parameters χ_i. Consequently, if a model is invariant under local $U(1)$ gauge transformations, the addition of a synthetic gauge field preserves such symmetry, and all gauge-related sets of Peierls phases describe the same physical situation.

2.1 Standard gauge choices for Peierls phases

Henceforth, we turn our attention specifically to the configuration where the total flux per plaquette is uniform, namely:

$$\Phi_\square = \Phi \quad \forall \text{ plaquette } \square\,. \tag{2.10}$$

We summarize the standard lattice prescriptions used to implement a homogeneous magnetic field perpendicular to a two-dimensional lattice. Lattice sites are labeled by integer coordinates (x, y). Peierls phases $A_{(x,y)\to(x',y')}$ are given in units where $q/\hbar$ is absorbed, and their sum around each plaquette yields a constant flux Φ.
For a uniform magnetic field there are two typical gauge choices.

1. **Landau gauge** (rectangular lattice). Continuum form: $\vec{A} = (0\,,\ Bx)$.

$$\text{Lattice prescription:} \qquad A_{(x,y)\to(x+1,y)} \;=\; 0\,, \quad A_{(x,y)\to(x,y+1)} \;=\; \Phi\, x\,. \tag{2.11}$$

   Landau gauge is widely adopted in Hubbard models [24] because it preserves translation invariance in one lattice direction, making momentum along that axis a good quantum number. All non-trivial Peierls phases reside on a single set of bonds, which minimizes the complexity of the hopping pattern and simplifies the construction of both the Bloch Hamiltonian and the magnetic unit cell. This structure enables efficient block-diagonalization for rational flux $\Phi = 2\pi p/q$, and allows straightforward implementation of twisted boundary conditions (flux insertion) for many-body Chern-number computations [25, 26]. This gauge is computationally convenient and connects transparently to continuum Landau levels, at the cost of hiding rotational symmetry, which can be restored by examining gauge-dressed symmetry transformations.

2. **Symmetric gauge** (square lattice). Continuum form: $\vec{A} = (-\frac{B\,y}{2}\,,\ \frac{B\,x}{2})$.

$$\text{Lattice prescription:} \qquad A_{(x,y)\to(x+1,y)} \;=\; -\frac{\Phi}{2}y\,, \quad A_{(x,y)\to(x,y+1)} \;=\; \frac{\Phi}{2}x\,. \tag{2.12}$$

   This gauge is often convenient to display rotational symmetry and to construct finite clusters with symmetric flux distribution.

For rational values of p/q in $\Phi = 2\pi p/q$, both Landau and symmetric gauges require an enlarged magnetic unit cell of q sites.
In practice, one chooses the gauge that yields the simplest magnetic unit cell and the most convenient numerical implementation for the geometry under study. For the above stated reasons, in this work we employ Landau gauge.

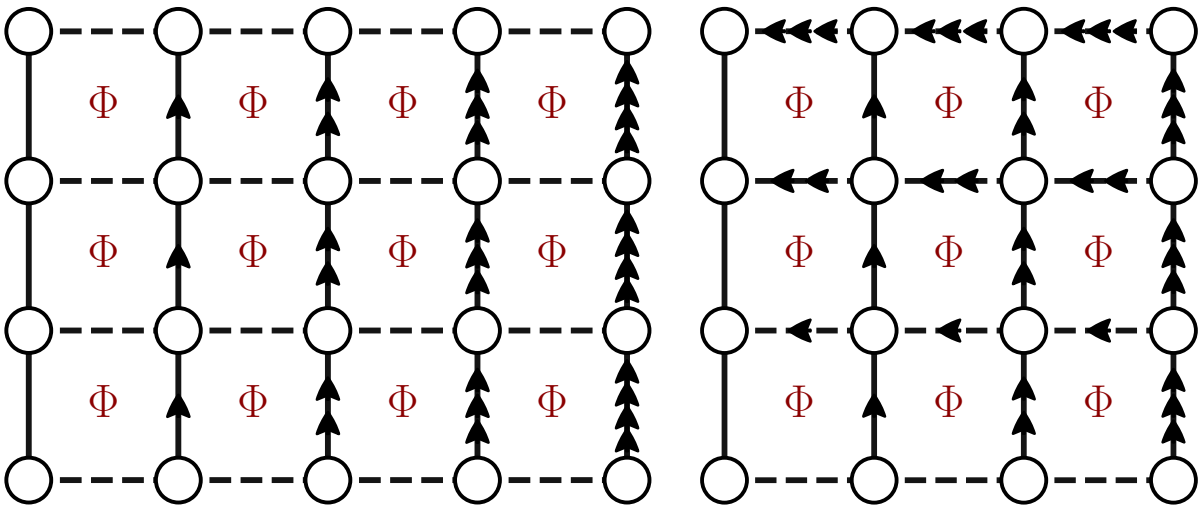

Figure 2.1: Left: Rule for Peierls phase arrangement in Landau gauge, where each arrow corresponds to an added phase Φ. Right: Peierls phase pattern in the symmetric gauge, where each arrow contributes a phase $\Phi/2$. Horizontal bonds are shown as dashed lines, vertical bonds as solid lines, and lattice sites are represented by empty circles. Arrows pointing upward or to the right indicate a positive phase contribution.

2.2 Flux-frustrated Bose-Hubbard minimal model

The simplest model describing interacting bosons subject to a magnetic field takes the form of a Bose-Hubbard model 1.1.

$$\hat{H} \;=\; -\sum_{\langle i,j\rangle}\Big(t_{ij}\, e^{\,\mathrm{i}A_{ij}}\,\hat{b}_i^\dagger\hat{b}_j + \mathrm{h.c.}\Big) \;+\; \frac{U}{2}\sum_i \hat{n}_i(\hat{n}_i-1) \;-\; \mu\sum_i \hat{n}_i\,, \tag{2.13}$$

where $\hat{n}_i = \hat{b}_i^\dagger\hat{b}_i$ is the local density operator on site i, U the on-site interaction and μ the chemical potential.
The magnetic field biases the particles toward closed-loop trajectories, and can promote net particle flow between lattice sites. This tendency is reflected in the expectation values of current operators, which are obtained from the continuity equation for the density. In the Heisenberg picture we have:

$$\frac{d\hat{n}_i}{dt} = \frac{\mathrm{i}}{\hbar}\big[\hat{H},\hat{n}_i\big] = -\sum_j \hat{J}_{i\to j}\,. \tag{2.14}$$

This equation describes the local time evolution of the particle density at a given site i, which amounts to the sum of currents from that site toward its neighbors, with a negative sign accounting for the outflow. The current operator from a site i to one of its neighbors j is expressed as

$$\hat{J}_{i\to j} \;=\; \mathrm{i}\,t_{ij}\big(e^{\,\mathrm{i}A_{ij}}\hat{b}_i^\dagger\hat{b}_j - e^{-\mathrm{i}A_{ij}}\hat{b}_j^\dagger\hat{b}_i\big)\,. \tag{2.15}$$

At fixed time, $\hat{J}_{i\to j}$ measures the quantum probability flux between two lattice sites, which is positive if the net flow is from i to j and vise versa. The current operator is gauge invariant, since under a local $U(1)$ transformation [Eq. (2.7)] it transforms as

$$\hat{J}_{i\to j} \mapsto \hat{J}'_{i\to j} = \mathrm{i}\,t_{ij}\big[e^{\,\mathrm{i}(A_{ij}+\chi_i-\chi_j)}\,e^{-\mathrm{i}\chi_i}\,\hat{b}_i^\dagger\,e^{\,\mathrm{i}\chi_j}\,\hat{b}_j - \mathrm{h.c.}\big] = \mathrm{i}\,t_{ij}\big[e^{\,\mathrm{i}A_{ij}}\hat{b}_i^\dagger\hat{b}_j - \mathrm{h.c.}\big] = \hat{J}_{i\to j}\,. \tag{2.16}$$

Its expectation value, namely the current between sites i and j, takes the form

$$J_{i\to j} \equiv \langle\hat{J}_{i\to j}\rangle = 2\,t_{ij}\,\mathrm{Im}\big[e^{\mathrm{i}A_{ij}}\langle\hat{b}_i^\dagger\hat{b}_j\rangle\big]\,. \tag{2.17}$$

Expressing the one-body correlator in polar representation,

$$\langle\hat{b}_i^\dagger\hat{b}_j\rangle = R_{ij}\,e^{\mathrm{i}\theta_{ij}}, \qquad R_{ij} = |\langle\hat{b}_i^\dagger\hat{b}_j\rangle|\,,$$

isolates the amplitude and phase dependencies of the current expectation value:

$$J_{i\to j} = 2\,t_{ij}\,R_{ij}\,\sin\big(A_{ij}+\theta_{ij}\big)\,. \tag{2.18}$$

The magnitude of the current is the product of three factors: the hopping strength t_{ij}, setting the kinetic energy scale; the coherence amplitude R_{ij}, quantifying the amount of phase-coherent density available to participate in transport; and the sine of the total phase difference along the link, $\sin(A_{ij}+\theta_{ij})$, converting the available coherence to net flow. A phase difference (modulo 2π) near 0 or π suppresses the current, while near $\frac{\pi}{2}$ or $\frac{3\pi}{2}$ maximizes the current for a given amplitude. The sign of this factor fixes the direction of the current.
Thus, the current reflects both the actual particle motion, accessible through dynamical observables, and the underlying phase coherence, encoded in equal-time correlations.

2.3 Flux-induced explicit time-reversal symmetry breaking

In the context of quantum mechanics, time-reversal $\mathcal{T}$ is an anti-unitary operator, typically expressed as $\mathcal{T} = \mathcal{U}\mathcal{K}$, where $\mathcal{U}$ is a unitary transformation and $\mathcal{K}$ denotes complex conjugation. Under the action of $\mathcal{T}$, the time coordinate transforms as $t \mapsto -t$.
To maintain the invariance of the Lorentz force, the electromagnetic vector potential $\vec{A}$ must transform as a t-odd quantity. For a static field configuration, this implies

$$\vec{A}(\vec{r}, t) \overset{\mathcal{T}}{\mapsto} -\vec{A}(\vec{r}, -t) \implies \vec{A}(\vec{r}) \overset{\mathcal{T}}{\mapsto} -\vec{A}(\vec{r})\,. \tag{2.19}$$

In a discrete lattice model, this transformation law extends to the Peierls phases, following Eq. (2.3). Consequently, the hopping parameters $t_{ij}e^{iA_{ij}}$ undergo complex conjugation, $t_{ij}e^{iA_{ij}} \to t_{ij}^* e^{-iA_{ij}}$, effectively mapping the Hamiltonian to its time-reversed counterpart:

$$A_{ij} \overset{\mathcal{T}}{\mapsto} -A_{ij} \implies \hat{H}(\{A_{ij}\}) \overset{\mathcal{T}}{\mapsto} \hat{H}(\{-A_{ij}\})\,. \tag{2.20}$$

The physical consequence of this transformation is most clearly observed in the magnetic flux $\Phi_\square$ piercing a plaquette. Since the flux is defined by the oriented sum of the gauge fields along a closed loop, the time-reversal operation flips its sign:

$$\Phi_\square = \sum_{\langle i,j\rangle \in \square} A_{ij} \overset{\mathcal{T}}{\mapsto} -\Phi_\square \implies \hat{H}(\Phi_\square) \overset{\mathcal{T}}{\mapsto} \hat{H}(-\Phi_\square)\,. \tag{2.21}$$

If the flux per plaquette is not vanishing or π, the Bose-Hubbard Hamiltonian with synthetic gauge field becomes complex and breaks time-reversal symmetry explicitly:

$$\Phi_\square \neq -\Phi_\square \pmod{2\pi} \implies \hat{H}(\Phi_\square) \neq \hat{H}(-\Phi_\square) = \mathcal{T}[\hat{H}(\Phi_\square)]\,. \tag{2.22}$$

The explicit breaking of this symmetry is reflected in the ground state, which can develop finite loop currents with a well-defined circulation direction. The loop current in a given plaquette $\square_k$ is defined as:

$$\hat{J}_\square^k = \sum_{\langle i,j\rangle \in \square_k} s_{ij}\,\hat{J}_{i\to j}\,, \qquad s_{ij} = \begin{cases} +1 & \text{if } i \to j \text{ follows the chosen orientation of } \square_k\,, \\ -1 & \text{otherwise.} \end{cases} \tag{2.23}$$

In this work, we adopt the clockwise direction as the positive convention for currents.
A loop current can also extend across multiple plaquettes. Whenever a nonzero circulating current encloses a region, the many-body wavefunction acquires a full phase winding around it, thereby defining a vortex. Since the current operator is odd under time reversal, $\mathcal{T}\,\hat{J}_{i\to j}\,\mathcal{T}^{-1} = -\hat{J}_{i\to j}$, any state with a finite current expectation value (or long-range current-current correlations) necessarily breaks time-reversal symmetry.

2.4 Many-body phases in the flux-frustrated Bose-Hubbard model

In the absence of flux, the Bose-Hubbard model exhibits two phases [7, 9]: a uniform superfluid (SF) with a gapless charge sector, and a uniform Mott insulator (MI) with a gapped charge sector. As shown in Fig. 2.2, the phase diagram in the t/U-μ/U plane exhibits the characteristic "Mott lobes" where the particle density is pinned to integer values n, representing an incompressible, gapped insulator phase. Inside the lobes, strong on-site interactions U dominate over the hopping parameter t, effectively localizing bosons to individual lattice sites. As t/U increases, the system undergoes a quantum phase transition into a compressible, phase-coherent superfluid state characterized by off-diagonal long-range order (OLDRO) in two or more spatial dimensions, and gapless excitations.

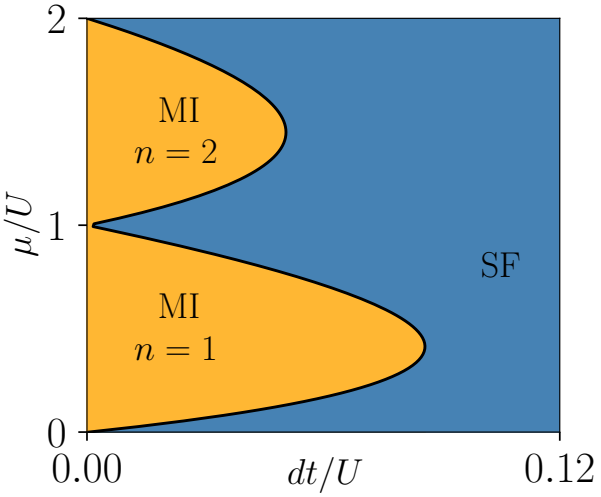

Figure 2.2: Ground-state phase diagram of the standard Bose-Hubbard model in a d-dimensional square lattice, within mean-field approximation. The plot illustrates the quantum phase transition between the Mott insulator (MI) and superfluid (SF) phases as a function of the dimensionless chemical potential μ/U and the hopping parameter t/U. Here $t_{ij} = t \ \ \forall \langle i, j \rangle$. The characteristic Mott lobes represent regions of the parameter space the particle density is pinned to $n = 1, 2, ...$ In the small t/U regime (the atomic limit), the system is dominated by on-site repulsive interactions, resulting in localized bosons. As t/U increases beyond a critical value, quantum fluctuations favor delocalization, driving the transition into the gapless superfluid phase. For states at specified integer filling, the critical value $(t/U)_c$ is the tip of the corresponding Mott lobe.

The introduction of a magnetic field does not alter the locality of the interaction structure but frustrates the kinetic energy, thereby splitting both the SF and the MI into several symmetry-distinguished sub-phases. The flux unlocks the relative phase sector, which may remain gapped or become gapless depending on the system parameters. In a standard, uniform Bose-Hubbard model, the Mott insulator phase requires integer filling at the single-site level. However, because the addition of flux enlarges the unit cell, in the flux-frustrated model certain fractional fillings correspond to an integer number of bosons per unit cell. This commensurability allows for the opening of a many-body gap, making the insulating phases possible at fractional filling, even with purely on-site interactions.

Below we summarize the resulting sub-phases for the ladder geometry, a widely studied setup in both theory and experiment, as it is the simplest possible extended lattice allowing non-trivial orbital effects in the presence of a synthetic magnetic field.
A ladder is a quasi-one-dimensional lattice embedded in a two-dimensional plane, extending predominantly along one direction. As depicted in Fig. 2.3, bonds parallel to this direction form the legs, while the perpendicular bonds constitute the rungs. In this chapter, we distinguish the hopping strength between legs and rungs:

$$t_{ij} = \begin{cases} J & \text{if } \langle i, j \rangle \in \text{leg}\,, \\ K & \text{if } \langle i, j \rangle \in \text{rung}\,. \end{cases} \tag{2.24}$$

The Hamiltonian of the model reads:

$$\hat{H} = -J\sum_{r=1}^{L}\sum_{l=1}^{2}(e^{\mathrm{i}A_{ij}}\,\hat{b}^{\dagger}_{r+1,l}\,\hat{b}_{r,l} + \mathrm{h.c.}) - K\sum_{r=1}^{L}(e^{\mathrm{i}A_{ij}}\,\hat{b}^{\dagger}_{r,1}\,\hat{b}_{r,2} + \mathrm{h.c.}) + \sum_{r=1}^{L}\sum_{l=1}^{2}\left[\frac{U}{2}\hat{n}_{r,l}(\hat{n}_{r,l}-1) - \mu\,\hat{n}_{r,l}\right],$$
$$\text{with} \quad \sum_{\langle i,j\rangle\in\square} A_{ij} = \phi \quad \forall \text{ plaquette } \square\,, \tag{2.25}$$

and where ϕ is the flux density, namely the flux per plaquette.

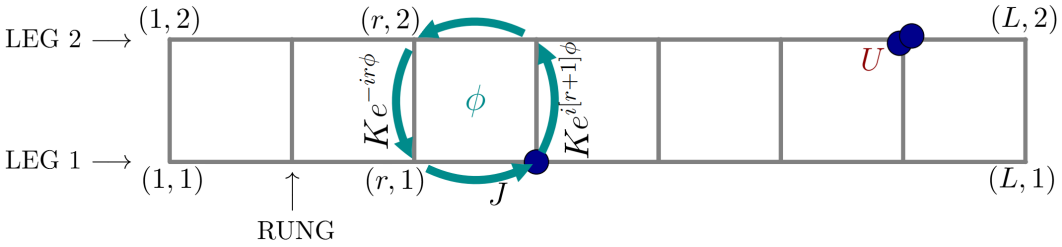

Figure 2.3: Schematic representation of the model on a two-leg ladder of length L with ϕ flux per plaquette, leg-hopping J and rung hopping K. Peierls phases are distributed along the rungs as specified by Landau gauge. On-site interaction is represented as an increase U in energy for a configuration with two particles on the same site. Lattice sites are labelled by (r, l), where r is the rung index and l the leg index.
Source: (Adapted from: [17]).

The phases are characterized by the following observables:

- central charge c, extracted from entanglement scaling. The central charge is a universal parameter of the low-energy conformal field theory (CFT) that describes the gapless sector(s) of a one-dimensional quantum system [27]. It is an extensive measure of the number of independent critical (gapless) degrees of freedom: each gapless free bosonic mode contributes $c = 1$, while a fully gapped sector contributes $c = 0$. For a critical 1D system whose continuum limit is a CFT, the von Neumann entanglement entropy $S(\ell)$ of a subsystem of length ℓ embedded in a system of length L obeys a universal scaling law [28]:

$$S(\ell) = \frac{c}{a}\ln\left[\frac{L}{\pi}\sin\left(\frac{\pi\ell}{L}\right)\right] + s_0\,. \tag{2.26}$$

  Here, $a = 6$ for open boundary conditions, while $a = 3$ for periodic boundary conditions; s_0 is a non-universal constant, and

$$S(\ell) \coloneqq -\mathrm{Tr}[\hat{\rho}_\ell\,\ln(\hat{\rho}_\ell)]\,, \tag{2.27}$$

  with $\hat{\rho}_\ell$ the reduced density matrix of the subsystem of length ℓ.
  A two-leg bosonic ladder has two low-energy bosonic fields: the total charge (symmetric) mode ($\mathfrak{c}$) and the relative phase (antisymmetric) mode (rp) [29]. When these sectors are independent at low energy, their contributions to the central charge add, such that: $c = c_{\mathfrak{c}} + c_{rp}$ Whether this separation holds depends on the specific Hamiltonian under study. For instance, a density-assisted hopping along the rungs may produce mixing of the two sectors. Under the conditions described in this work, the two modes remain independent and their contributions can be treated separately.

- vortex density ρ_v, generally defined as the number of vortices divided by the number of plaquettes. A microscopic, universally valid definition of ρ_v does not exist, because different operational definitions are not equally stable across all phases. As emphasized in [18], the

vortex density is not a fundamental local observable but a derived quantity that must be extracted numerically. In practice, ρ_v can be inferred in several ways, most commonly from the pattern of local currents, from the phase winding around plaquettes, or from characteristic features in the momentum distribution. These different approaches generally agree in regimes with well-formed vortex structures, but they may diverge or become ambiguous in phases where vortices are strongly fluctuating.

- number of plaquettes q that constitute the unit magnetic cell of the ground state, indicating the periodicity of the current pattern.
- average rung current $\langle \hat{J}_\perp \rangle$, which measures how much current penetrates the bulk of the ladder.

$$\langle \hat{J}_\perp \rangle = \frac{1}{L} \sum_r \langle \hat{J}_{(r,1)\to(r,2)} \rangle \tag{2.28}$$

- density imbalance between legs $\Delta n = \langle \hat{n}_{LEG\,1} - \hat{n}_{LEG\,2} \rangle$, which signals the spontaneous breaking of the discrete $\mathbb{Z}_2$ leg-exchange symmetry. Here, $\hat{n}_{LEG\,j} = \sum_r \hat{n}_{r,j}$.

In the table below the phases of the Bose-Hubbard model with Peierls substitution are classified according to these quantities [17, 18]. The phases are generally obtained by introducing hopping anisotropy ($J \neq K$), without the need for extended interactions or higher-order terms.

Sub-phase	$c_\mathfrak{c}$	c_{rp}	ρ_v	q	$\langle \hat{J}_\perp \rangle$	Δn
Meissner (M)	0 or 1	0	0	1	0	0
Vortex Lattice (VL)	0 or 1	0	$1/m$	$m \in \mathbb{N}_{>1}$	$\neq 0$	0
Vortex liquid (V)	0 or 1	1	> 0	1	0	0
Charge-Density Wave (CDW)	0	0	0	$m \in \mathbb{N}_{>1}$	0	0
Biased-Ladder (BLP)	1	0	0	1	0	$\neq 0$

Table 2.1: Many-body quantum phases of the flux-frustrated Bose-Hubbard model on a 2-leg ladder lattice. Source: (Adapted from [18])

Current and density patterns for VL, BLP and CDW phases are reported in Fig. 2.7. Meissner and Vortex liquid phases are the subject of the next subsection.

In a **Meissner (M) phase** [30], vortices are expelled, and the system develops a smooth, monotonic phase twist along the ladder. The chiral current is uniform around the border, and the flow remains coherent and unidirectional. This phase is especially relevant because a boundary current coexisting with an insulating bulk is a key feature of Quantum Hall systems. This phase has been experimentally observed in ultracold atom ladder systems [31]. As shown in Fig. 2.4, Meissner phases are robust across weak, intermediate, and strong interactions and emerge by introducing spatial anisotropy in the hopping strengths ($K > J$). Meissner states are further stabilized by introducing on-rung repulsive interactions:

$$\hat{H}_V = V \sum_r \hat{n}_{r,1} \hat{n}_{r,2}, \tag{2.29}$$

where the number operator $\hat{n}_{r,l}$ acts on sites labeled by r, the rung index, and $l = 1, 2$, the leg index. Such interactions naturally arise in synthetic-dimension experimental implementations [11], where Raman lasers drive transitions among selected hyperfine states of bosonic (or fermionic) atoms arranged in an actual one dimensional optical lattice. Because the underlying atomic interaction is contact-like, all atoms occupying the same real-space lattice site interact irrespective of their hyperfine state. As a result, particles on different legs of the same rung, namely atoms in different hyperfine states and on the same real-space lattice site, naturally experience a repulsive interaction

of the form above.

In a **Vortex Lattice (VL) phase**, vortices enter the system but are regularly arranged. This produces a static pattern of circulating currents with a well-defined periodicity q. VL phases with $\rho_v > 1/2$ also exhibit strong density modulations commensurate with the magnetic unit cell. Vortex lattices thus spontaneously break discrete translational symmetry. In low density regimes, with filling up to one, VL phases have been reported only for weak and intermediate interaction strengths. The phase diagram in Figure 2.4 displays Vortex Lattice phases for intermediate $K/J > 1$ and interaction strengths up to $U/J = 15$. Interactions can also induce non-trivial dynamical effects. In particular, certain Vortex Lattice states have been shown to exhibit a spontaneous reversal of the boundary chiral current [18]: the circulating flow switches direction as if the sign of the applied flux had been inverted, "screening" the Meissner effect. This behavior follows from the enhancement of the effective flux per unit cell from ϕ to $q\phi$, since in vortex lattices the unit cell gets enlarged to q plaquettes. Given the 2π-periodicity of the chiral current, only vortex lattices stabilized in the regime $\pi < q\phi < 2\pi$ display this reversal [17]. The effect remains robust at experimentally accessible temperatures, making it a practical probe for identifying Vortex Lattice order.

A **Vortex liquid (V) phase** contains vortices, but lacks long-range vortex order. The vortices fluctuate strongly and do not form a periodic pattern, producing a disordered arrangement of plaquette currents that preserves all lattice symmetries while still reflecting the underlying magnetic frustration. Because their positions are not locked into an ordered structure, vortices behave as gapless excitations, and the system supports low-energy rearrangements of the current pattern. This phase can be viewed as the intermediate regime between the Meissner state, where vortices are expelled, and Vortex Lattice phases, where they crystallize. Its properties are analogous to vortex liquids in type-II superconductors [32], where thermal or quantum fluctuations melt the vortex lattice and restore translational symmetry. In the phase diagram Fig. 2.4, Vortex liquids occupy regions around $K \simeq J$. For low interactions they are superfluids; increasing U they transition to V-Mott insulator.

The Meissner, vortex liquid, and vortex lattice phases should be understood as different regimes of the same underlying mechanism: the competition between magnetic flux, which favors circulating currents and vortex formation, and inter-leg coherence, which tends to lock the relative phase and suppress vortices. Increasing flux or reducing hopping anisotropy drives the system from a vortex-free Meissner state to a fluctuating vortex liquid and, in certain commensurate regimes, to ordered vortex lattices. These three sub-phases can occur in both the superfluid and Mott insulating regimes. The distinction is encoded in the charge sector: when the total charge sector is gapless ($c_{\mathfrak{c}} = 1$), the phase is superfluid; when it is gapped ($c_{\mathfrak{c}} = 0$), the system is a Mott insulator.

In addition to vortex-related phases, for strong interactions the model admits further types of order that involve density rearrangements or internal symmetry breaking.

A **Charge-Density Wave (CDW) phase** exhibits a spatial modulation of the particle density with a definite period. Here the system lowers its energy by reorganizing the density rather than by arranging vortices. The unit cell is enlarged like in the VL phase, therefore breaking discrete translational invariance. The ground state currents usually appear to be Meissner-like, since rung currents are suppressed. This is a fully gapped phase and in the model under study is connected only to the Mott insulator [17]. CDW phases emerge for sufficiently strong interactions and high anisotropy between leg and rung hopping. Fig. 2.5 shows the transition from $\mathrm{VL}_{1/2}$-MI to $\mathrm{CDW}_{1/4}$ when interactions increase beyond $U = 30J$, for fixed flux per plaquette $\phi = 0.98\pi$ and $K = 3.2J$. The subscript 1/4 specifies the filling (particle density) of the system in this phase.

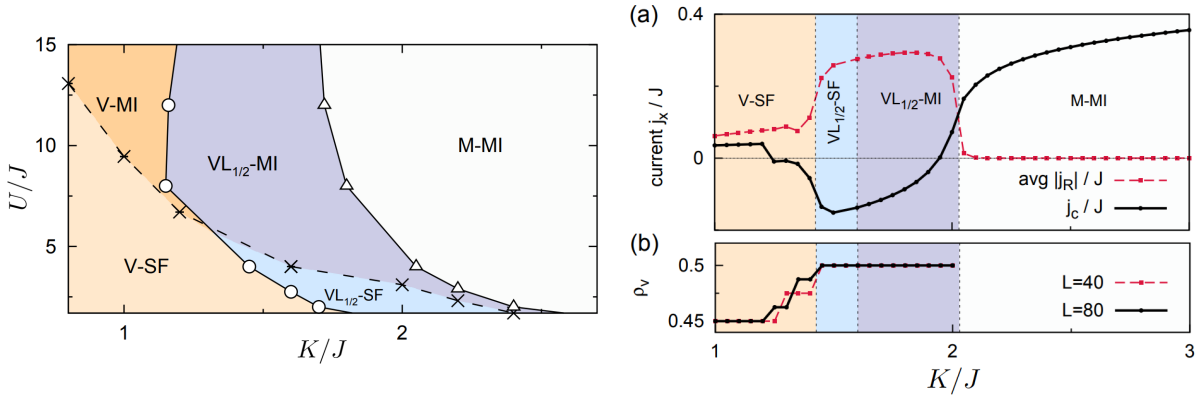

Figure 2.4: Phase diagram of the Bose-Hubbard model on a two-leg ladder with $\phi = 0.9\pi$ flux per plaquette at half filling ($n = 0.5$). The 1/2 in $\mathrm{VL}_{1/2}$ specifies the vortex density of such Vortex Lattice state: $\rho_v = 1/m = 1/2$. Left: phase diagram in the U/J versus K/J plane. Symbols denote estimated points of the respective phase transitions: '$\times$' marks superfluid to Mott insulator phase transition, '$\circ$' Vortex liquid to $\mathrm{VL}_{1/2}$, '$\triangle$' $\mathrm{VL}_{1/2}$-MI to Meissner Mott insulator. Right: cut through the phase diagram at $U/J = 4$. (a) chiral current j_c/J and average rung current $\mathrm{avg}|j_R|$ as a function of K/J. Here, $j_c = \frac{1}{N}\sum_r \langle \hat{J}_{(r,1)\to(r+1,1)} - \hat{J}_{(r,2)\to(r+1,2)} \rangle$, key observable to quantify the chiral border current typical of the Meissner phase. (b) vortex density versus K/J. Dashed lines indicate the positions of the phase transitions. Source: (Adapted from [18]).

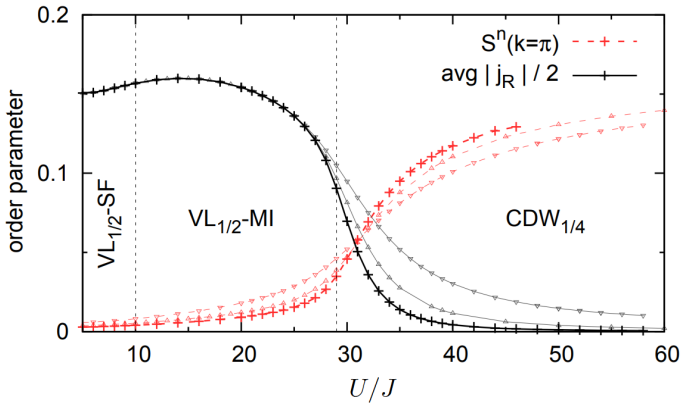

Figure 2.5: Phase diagram of the Bose-Hubbard model on a two-leg ladder with $\phi = 0.98\pi$ flux per plaquette and $K = 3.2J$ at quarter filling ($n = 0.25$). Average rung current $\mathrm{avg}|j_R|$ and CDW order parameter $S^n(k = \pi)$ as a function of U/J for several system sizes: $L = 80$ ('+' symbols), $L = 60$ ('Δ'), $L = 40$ ('∇'). Here, $S^n(k = \pi) = \frac{1}{L}\sum_{i,j} e^{\mathrm{i}(i-j)\pi}\langle \hat{n}_i \hat{n}_j \rangle$. Source: (Adapted from [18])

The **Biased-Ladder phase (BLP)** spontaneously breaks the discrete $\mathbb{Z}_2$ symmetry that exchanges the two legs of the ladder: it develops a density imbalance even though the Hamiltonian treats the legs symmetrically. Translational symmetry is preserved, thus there is no density modulation along the ladder, only between the legs. In addition, this typically leads to currents arranged along the border and vanishing on the rungs (zero vortex density ρ_v), similar to a Meissner phase. The charge sector is gapless, so the BLP is a superfluid phase. BLP has been found for weak and intermediate interactions, with larger U range for the flux approaching π. BLP is stabilized by strong anisotropies that favor rung hopping. The range of parameters for which BLP is found in the dilute limit ($n \ll 1$), for two different values of the flux ϕ, can be observed in Fig. 2.6.

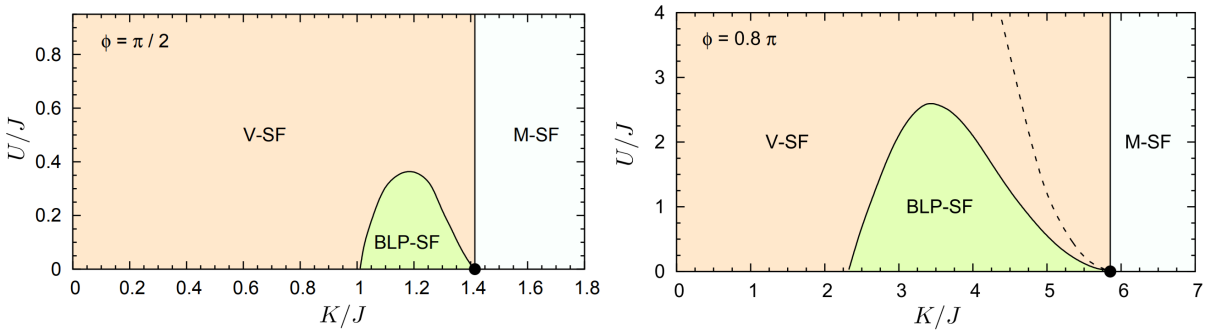

Figure 2.6: Phase diagram in the U/J versus K/J plane of the Bose-Hubbard model on a two-leg ladder with $\phi = 0.5\pi$ (left) and $\phi = 0.8\pi$ (right) flux per plaquette in the dilute limit ($n \ll 1$). Notice how increasing the magnetic flux considerably widens the domain of on-site interaction strengths for which BLP is present. Incrementing the flux also shifts the BLP phase region to higher values of K/J. Source: (Adapted from [18]).

Under specific adjustments of the Hamiltonian, the model supports a variety of secondary phases; however, as these are not the central object of this work, they are not analyzed in detail here.
One can actively break translational symmetry by selecting non-periodic hopping strengths in order to form quasi-periodic ladders or superlattices. This leads to the manifestation of phases mixing vortex and Meissner characteristics (Strong Vortex-Meissner, Weak Vortex-Meissner) and the appearance of incompressible domains for specific fillings of the lattice [33].
Including nearest neighbor interactions in the flux-frustrated Bose-Hubbard model leads to the stabilization of a supersolid state [34, 35]. A supersolid (SS) combines superfluid coherence (ODLRO) with static density modulation (density-wave diagonal long-range order), which breaks translational invariance.

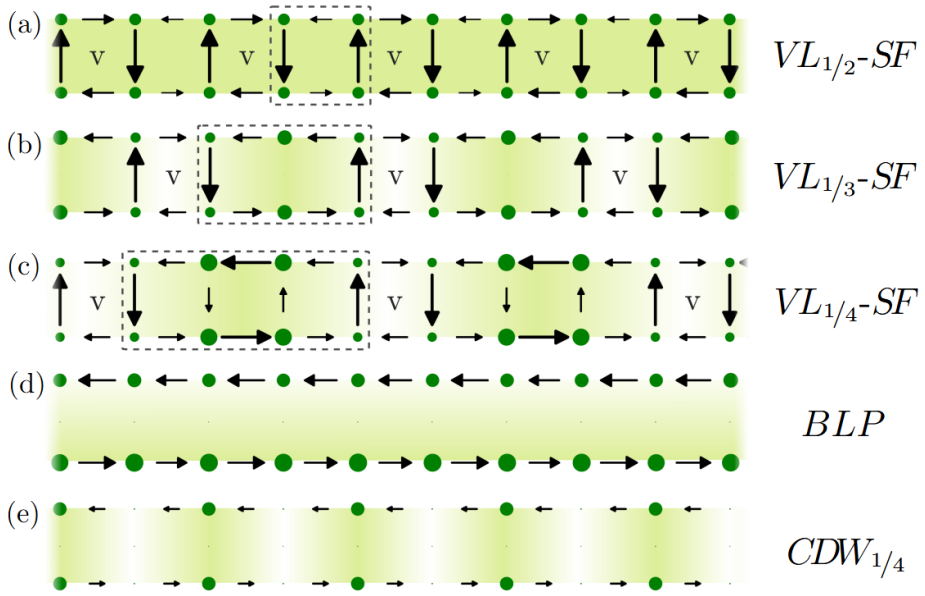

Figure 2.7: Current and density patterns for the different phases of the flux-frustrated Bose-Hubbard model on a two-leg ladder. First three are different Vortex Lattice phases, with vortex densities $\rho_v = 1/2$ (a), $\rho_v = 1/3$ (b) and $\rho_v = 1/4$ (c). (d) is the Biased-Ladder phase and (e) the Charge-Density Wave at quarter filling ($n = 0.25$). Source: (Adapted from [18]). Current patterns for the Meissner and Vortex liquid phases are reported in the next section.

2.4.1 DMRG simulation of the M-MI to V-MI phase transition

To illustrate the physics of flux-frustrated Bose-Hubbard model, we perform a small scale DMRG calculation of the quantum phase transition between the Meissner Mott insulator and the vortex Mott insulator on a two-leg ladder. An illustrative sketch of the model is shown in Fig. 2.3. Although the simulation is not intended as a full numerical study, it captures the essential features of the transition and provides a clear, didactic example of how magnetic frustration reorganizes current patterns in an interacting system. We scan ladders of length L up to 14 rungs with open boundary conditions. here we consider hardcore bosons ($U \to \infty$) at half filling ($n = 0.5$), and distinguish the hopping strength between legs and rungs [Eq. (2.24)]. Hardcore bosons are convenient to simulate because each site has a two-dimensional local Hilbert space, spanned by the empty state $|0\rangle$ and the singly occupied state $|1\rangle$. On the other hand, for finite on-site interactions, multiple bosons can occupy the same site with nonzero probability; therefore, truncating the local Hilbert space to a few occupation states becomes an approximation whose accuracy depends on the interaction strength. In this section only, we fix the flux per plaquette to $\pi/2$, and implement it via Landau gauge. The resulting Hamiltonian is:

$$\hat{H} \;=\; -J\sum_{r=1}^{L}\sum_{l=1}^{2}\big(\hat{b}^{\dagger}_{r+1,l}\,\hat{b}_{r,l}+\text{h.c.}\big) - K\sum_{r=1}^{L}\big(e^{-ir\frac{\pi}{2}}\hat{b}^{\dagger}_{r,1}\,\hat{b}_{r,2}+\text{h.c.}\big) + \frac{U}{2}\sum_{r=1}^{L}\sum_{l=1}^{2}\hat{n}_{r,l}(\hat{n}_{r,l}-1)\,, \quad (2.30)$$

where we omit the chemical potential term because we are working in a fixed particle-number sector.

Parameter	J	K	Φ	L	n	U	BC
Value	1	[0, 2]	$\frac{\pi}{2}$	$\{4, 6, 8, 10, 12, 14\}$	0.5	$\to \infty$	open

Table 2.2: Summary of the model parameters adopted in this section. J is the leg coupling, K the rung hopping parameter, Φ the (uniform) magnetic flux per plaquette, L the ladder length, n the filling fraction (particle density), U the on-site interaction strength, and BC the boundary conditions.

We use standard two-site finite-DMRG sweeps employing the TeNPy package [36]. The DMRG algorithm [37] is a variational method for finding ground states (and, with suitable modifications, low-lying excited states) of quantum lattice Hamiltonians. It represents the many-body wavefunction as a matrix-product state (MPS) and optimizes the local tensors through iterative sweeps. At each step, the algorithm performs a Schmidt decomposition of the many-body density matrix reduced across a given bond and truncates the Hilbert space by discarding Schmidt states with the smallest singular values. These states contribute least to the entanglement structure of the wavefunction and therefore have minimal weight in the variational approximation. The number of Schmidt states retained after truncation defines the bond dimension χ_{bond} of the MPS. DMRG is most effective for one-dimensional or quasi-one-dimensional systems with short-range interaction and low entanglement, where the ground state can be accurately represented by an MPS with moderate bond dimension, allowing accurate simulations with tractable computational cost [1]. In our implementation, the bond dimension χ_{bond} of the MPS is adaptively increased during sweeps, up to a maximum value $\chi^{\text{max}}_{\text{bond}} = 1200$. The truncation of the Schmidt spectrum is controlled through a minimum singular-value threshold: we set $\text{SVD}_{\text{min}} = 10^{-10}$, so that Schmidt coefficients smaller than this cutoff are discarded. This criterion removes states whose weight lies below numerical precision and typically leads to convergence at bond dimensions far below the imposed maximum. In practice, the entanglement in the gapped Mott phases remains sufficiently small that the actual bond dimensions in our simulations never exceed $\chi_{\text{bond}} \sim 200$. The simulation halts if two consecutive iterations converge to ground state energies that differ by at most $E^{\text{max}}_{\text{err}} = 10^{-10}$, or if the maximum number of sweeps is reached: $\text{SWEEPS}_{\text{max}} = 10$.

DMRG spec	$\mathrm{SVD}_{\mathrm{min}}$	$\chi_{\mathrm{bond}}^{\mathrm{max}}$	$E_{\mathrm{err}}^{\mathrm{max}}$	$\mathrm{SWEEPS}_{\mathrm{max}}$
Value	10^{-10}	1200	10^{-10}	10

Table 2.3: Summary of the chosen DMRG simulation specifics. $\mathrm{SVD}_{\mathrm{min}}$ is the minimum singular-value threshold for the truncation of the MPS Schmidt spectrum, $\chi_{\mathrm{bond}}^{\mathrm{max}}$ the maximum allowed MPS bond dimension during the simulation, $E_{\mathrm{err}}^{\mathrm{max}}$ the ground state energy threshold for convergence, and $\mathrm{SWEEPS}_{\mathrm{max}}$ the maximum number of sweeps allowed in the DMRG process.

By tuning the hopping strength ratio K/J while keeping the flux and interaction strength fixed, we track observables such as the chiral current, the rung currents and the local densities. These quantities reveal how the system evolves from a Meissner state with uniform boundary currents and no vortices (see Fig. 2.8 (top)) to a vortex Mott insulator where vortices proliferate (see Fig. 2.8 (bottom)).

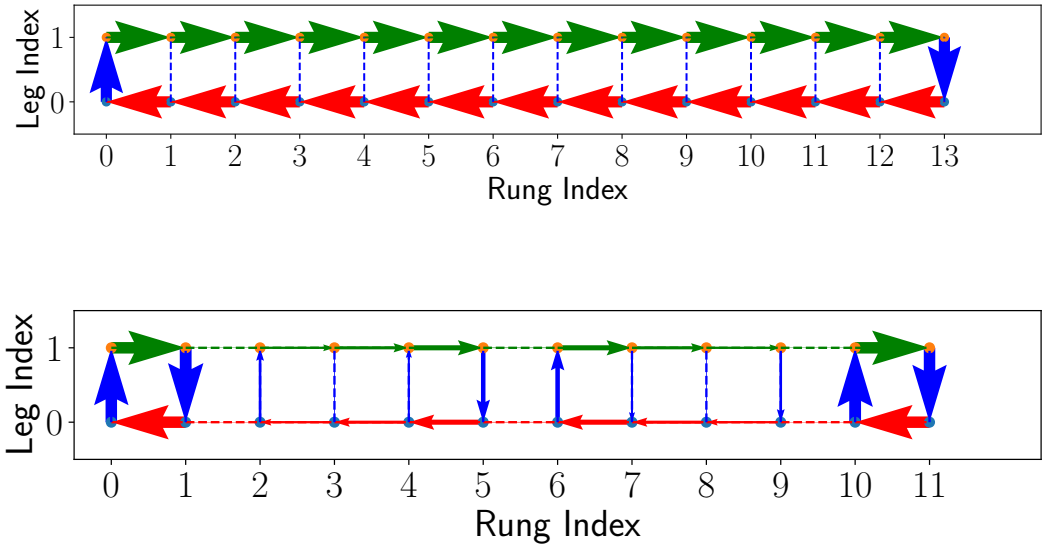

Figure 2.8: Current patterns obtained from DMRG simulations of hardcore bosons on a two-leg ladder with flux per plaquette $\phi = \pi/2$ in different phases. Colors distinguish up-leg coupling (green), down-leg coupling (red), rung coupling (blue). Arrow width is proportional to the current magnitude in units of J and arrow direction accounts for the current sign.
Top: Meissner currents for $K = 2J$ on a ladder of length $L = 14$, showing a uniform edge current with no penetration into the bulk. The edge current has a value of approximately $0.23J$, while the average rung current is of order $10^{-16}J$, fully compatible with zero within numerical precision.
Bottom: vortex currents for $K = 0.05J$ on a ladder of length $L = 12$; currents are magnified by a factor of 500 for visibility: here the average order of magnitude is $10^{-4}J$. Circulating patterns enclosing one or more plaquettes are clearly visible.

Even at small system sizes, the DMRG results clearly display the qualitative change in current structure and the emergence of vortex order, providing an intuitive picture of the underlying quantum phase transition and illustrating why ladder geometries are particularly well suited for numerical studies with DMRG.
Another quantity that helps distinguish between the two phases is the central charge, which, as discussed in the previous section, can be extracted from the entanglement entropy scaling of Eq. (2.26).

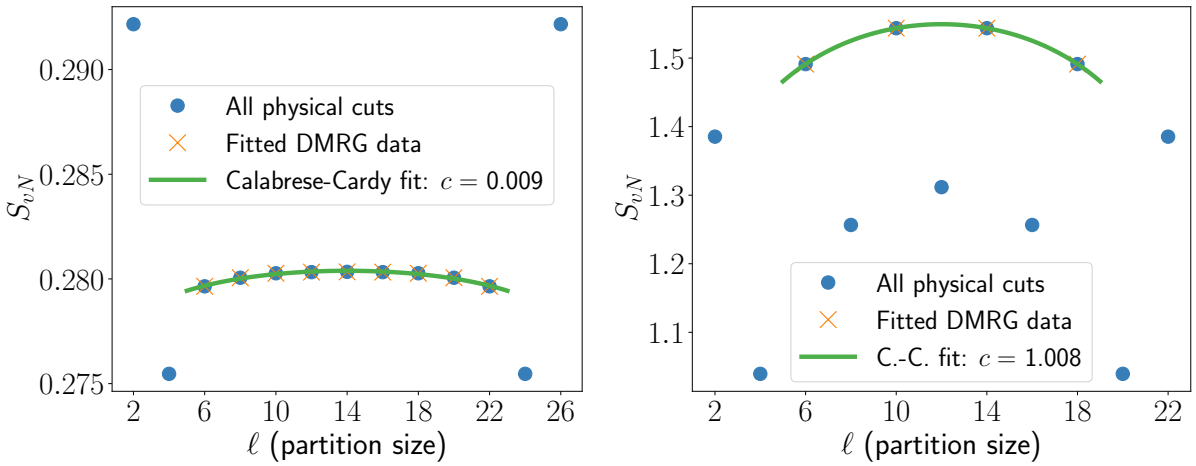

Figure 2.9: Von Neumann entanglement entropy (S_{vN}) as a function of system bipartition size (ℓ). Only physical bipartitions are shown, i.e. cuts that split the ladder into two subsystems with an even number of sites each, leaving all rungs intact. Left: $S_{vN}(\ell)$ in the Meissner Mott insulator phase ($K = 2J$, $L = 14$). Data follow the expected area-law/CFT baseline with deviations only for the boundaries.
Right: $S_{vN}(\ell)$ in the Vortex liquid MI phase ($K = 0.05J$, $L = 12$). A clear logarithmic envelope consistent with a single gapless relative-phase mode ($c \simeq 1$) is modulated by a pronounced oscillatory correction produced by a boundary-pinned finite-wavevector mode, which splits the entropies into two branches.

The observed two alternating branches in Fig. 2.9 correspond to an even-odd effect in the bipartition lengths and it arises from a boundary induced oscillatory corrections analogous to Friedel oscillations. Open boundary conditions select and lock the phase of an incommensurate relative-phase mode (vortex) into a standing wave whose wavelength equals half the system length. Thus, as one can notice in the current patterns in Fig. 2.8 (bottom), the ground state is composed of two mirror-related halves rather than a smaller unit cell. The standing wave fixes a spatial phase, so bipartitions that sample different phases of that modulation measure different amounts of local entanglement [38]. This is why the von Neumann entropy data split into two branches even after removing un-physical (rung-cutting) partitions. This pattern is not evidence of spontaneous translational symmetry breaking, but of a finite-size, boundary-pinned modulation. For scaling analysis one must therefore consider boundary-induced oscillatory corrections ($\cos(k\ell + \varphi)$) to the universal Calabrese-Cardy term, or, as done here, restrict the fit to a single phase subsequence. Nonetheless, when interpolating the entanglement entropy for cuts in the bulk of the system we find fit parameters compatible with the expected values of the total central charge for both phases:

$$c_{\text{M-MI}} = 0\,, \quad c_{\text{V-MI}} = 1\,.$$

To locate the transition more systematically, we complement these observables with the fidelity susceptibility χ_f, which offers a sensitive probe of ground-state rearrangements.

$$\chi_f(K/J) = \lim_{\delta K/J \to 0} \frac{-2 \ln |\langle \Psi_0(K/J) | \Psi_0(K/J + \delta K/J) \rangle|}{(\delta K/J)^2} \tag{2.31}$$

By computing the overlap between ground states $|\Psi_o(K/J)\rangle$ at neighboring values of K/J we extract the corresponding susceptibility peak, which serves as an indicator of the critical point in finite systems. We estimate this quantity for fixed δK.

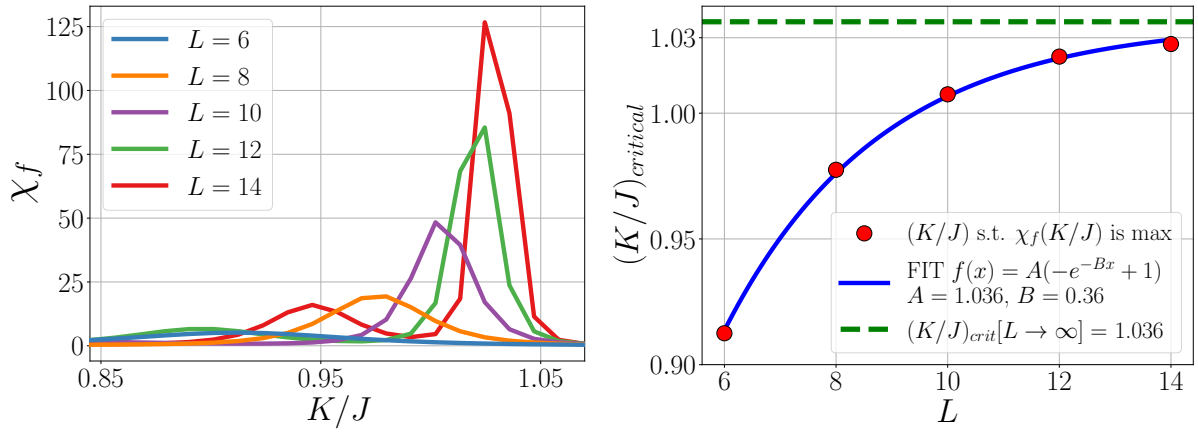

Figure 2.10: Left: normalized fidelity susceptibility χ_f/L as a function of K/J for $L = \{6, 8, 10, 12, 14\}$, with colors distinguishing system sizes. Right: exponential finite-size scaling of the peak positions versus L to estimate the critical point in the thermodynamic limit ($L \to \infty$). Because the simulated ladder lengths are too small to access the standard algebraic scaling regime, the exponential function is used here simply as an empirical fit to the data subject to strong finite-size effects.

Taken together, the current patterns, entanglement scaling, and fidelity-based diagnostics provide a coherent picture of the crossover from the Meissner Mott insulator to the vortex Mott insulator. Although our calculations are limited to modest system sizes, they are able to capture the essential physics of the transition and illustrate how tensor-network methods can efficiently resolve competing orders in frustrated ladder systems. We confirm that spatial anisotropy favoring rung hopping ($K > J$) drives the system out of the vortex regime and stabilizes the Meissner phase.

2.5 Connection to topological phases of matter

The purpose of this section is to briefly review the definitions and main concepts of topological phases of matter as presented in Wen's Colloquium [39]. These notions will be used in the next section to identify which types of topological phenomena can arise in the system under study, namely the Bose-Hubbard model with magnetic flux introduced in the previous sections.
Topological phases of matter are zero-temperature gapped quantum phases whose essential features are not captured by local symmetry breaking [3] but by global, many-body entanglement patterns. They are characterized by topological invariants: non-local quantities defined from the ground state wavefunction (or its effective band structure) that remain unchanged under any gap-preserving smooth local deformation of the Hamiltonian [2]. Fundamental examples are the Berry phase [40] and the Chern number. For a pedagogical review of these invariants see [41].
We distinguish between two kinds of topological phases [39, 42]: intrinsic topologically ordered phases and symmetry protected topological (SPT) phases. Intrinsic topological order is a gapped phase of a local many-body Hamiltonian whose ground state manifold cannot be transformed into a trivial product state by any finite-depth local unitary circuit [43] without closing the gap. The ground state exhibits long-range entanglement: correlations of non local operators persist at arbitrarily large length scales and cannot be removed by local unitary transformations. This definition is symmetry-independent. Signatures of this type of order in two spatial dimensions are:

- Ground state degeneracy on closed manifolds [44]. The number of degenerate ground states depends only on the topology of the spatial manifold and cannot be lifted by any local perturbation in the thermodynamic limit;
- Fractionalized excitations and anyonic statistics. Intrinsic topological order supports topo-

logical excitations in the bulk of the system. Topological excitations are local changes of the ground states near a spatial point $\vec{x}$ that cannot be created individually by local operators. Such excitations are created in pairs or along strings, and may carry fractional quantum numbers (for example fractional charge [45]) and obey Abelian or non-Abelian exchange statistics [4]. When such fractional excitations are point-like quasiparticles confined in two spatial dimensions, they are called anyons [46].

- Topological entanglement entropy. In this type of systems, entanglement entropy area law scaling has to be modified to acquires an additional constant correction. In 2D for instance, this subleading universal relates to the logarithm of the total quantum dimension. This term is called topological entanglement entropy (TEE or γ) [47] and its value provides an estimate of long-range entanglement.

$$S_A = \alpha L - \gamma + \dots$$

  where S_A is the entanglement entropy of a simply connected region A and L the length of the boundary of A.

- Edge physics and chiral central charge. When a boundary exists, it may host protected gapless edge modes linked to the topological properties of the bulk (bulk-edge correspondence [48]). Their chiral central charge controls the thermal Hall response [49] and is a topological invariant.

Fractional Quantum Hall (FQH) phases, which are realized by strongly-interacting 2D electron gases in a magnetic field and display fractionalized Hall response [45, 50], are canonical realizations of intrinsic topological order.

A symmetry protected topological (or trivial) phase is a gapped, short-range entangled phase that is not adiabatically connected to a trivial product state while preserving a specified global symmetry. If the protecting symmetry is broken explicitly, a SPT state can be continuously deformed to a trivial product state without closing the gap. Thus, SPT phases are distinguished from intrinsic topological order by their reliance on a symmetry for non-triviality. Signatures of this type of order are:

- Protected boundary states. A SPT phase typically hosts gapless or symmetry-breaking boundary modes and that cannot be removed without either breaking the protecting symmetry or closing the bulk gap. The edge can also exhibit topologically ordered phases itself.

- The absence of bulk topological excitations. The bulk of a SPT state is short-range entangled and cannot support deconfined excitations: any non-trivial response resides in the boundary of the system.

- Symmetry-based classification. SPT phases can be classified according to the protecting symmetry and distinct phases cannot be connected without symmetry breaking or gap closing. One result in this direction is the classification of noninteracting fermionic SPT phases, namely topological insulators and superconductors, within the so-called "tenfold way", based on Altland-Zirnbauer symmetry classes [51, 52].

Examples of this class of phases include the spin-1 Haldane chain [53] and topological insulators [51]. A generalization of SPTs can be made by invoking the definition of invertible topological order. An invertible topological phase is gapped, short range entangled and its many-body state yields a trivial product state when stacked with a suitable "inverse" state [54]. It is described at low energy by an invertible topological quantum field theory [55]. As SPTs, invertible topological phases are characterized by non-trivial boundaries while lacking the presence of topological excitations in the bulk, of topological ground state degeneracy, and of the TEE term in the entanglement

scaling. However, in a more general way, invertible topological phases do not necessitate the presence of a global (protecting) symmetry to display this behavior. For example, Integer Quantum Hall (IQH) states are, in general, topologically invertible. In specific cases their non-triviality relies on the presence of a global symmetry (for example $U(1)$ or lattice symmetries), satisfying the SPT definition [54].

The two classes of topological phases are linked: gauging a global symmetry of a SPT phase can produce an intrinsically topologically ordered phase (hosting bulk topological excitations) [56]. As a consequence, some topologically ordered phases can be viewed as gauged versions of SPTs or other short range entangled states.

2.6 Quantum Hall states: from the continuum to the lattice

Quantum Hall (QH) states are two-dimensional, gapped phases that appear in charged systems under strong perpendicular magnetic fields and at low temperature. They are defined by quantized transverse (Hall) conductance and insulating longitudinal response. The Hall conductance is the DC transverse conductivity of quantum systems: it relates an applied in-plane electric field E_y to the induced transverse current density $\jmath_x$ via the following:

$$\jmath_x = \sigma_{xy} E_y. \tag{2.32}$$

In Quantum Hall systems:

$$\sigma_{xy} = \nu \frac{e^2}{h}, \quad \text{with } \nu = \frac{n}{n_\Phi} \tag{2.33}$$

where the filling factor ν is the ratio of the particle density n and of the magnetic flux density Φ in units of the flux quantum $n_\Phi = \Phi/2\pi$ (in natural units $\hbar = e = 1$).
In Quantum Hall systems, particles organize themselves into highly degenerate, dispersionless energy levels known as Landau levels. A Landau level is a flat band of quantized kinetic energy that arises when charged particles move in a two-dimensional plane under a uniform perpendicular magnetic field. Each level hosts a macroscopic number of states with continuous degeneracy associated with angular momentum quantum numbers. This lies at the core of the topological robustness and quantized transport observed in QH phases. The filling factor ν measures how many Landau levels are filled by the particles and is equal to the total Chern number for completely occupied bands in the lattice version.

Integer Quantum Hall (IQH) states arise already in noninteracting (or weakly interacting) electron systems: the single-particle spectrum organizes into Landau levels, and the Hall conductance is given by an integer multiple of the conductance quantum [5], $\nu \in \mathbb{Z}$.
IQH phases are therefore characterized by a single-particle topological invariant (the Chern number), and protected chiral edge modes, whose number equals ν (bulk-edge correspondence).

Fractional Quantum Hall (FQH) states are intrinsically interaction-driven: at partial Landau-level filling, strong correlations stabilize incompressible liquids with fractional Hall conductance [45], $\nu \in \mathbb{Q}$. FQH phases exhibit hallmark many-body phenomena absent in IQH systems: bulk anyonic quasiparticles carrying fractional charge and fractional (Abelian or non-Abelian) exchange statistics, a ground-state degeneracy that depends on spatial topology, and the universal subleading contribution to entanglement entropy. Edge excitations are described by chiral conformal field theories whose structure reflects the bulk topological order.
Experimentally, QH physics was first observed in high-mobility two-dimensional electron gases

(GaAs heterostructures) [50] and later in graphene [57, 58] and engineered Moiré systems [59, 60]. Lattice analogues (Chern insulators and fractional Chern insulators) realize the same topology without a continuum Landau level [61, 62]. Peculiar features are extreme robustness to disorder (quantization persists as long as the bulk gap remains open), quantized transport as a topological response, and the possibility of nonlocal ground-state degeneracy and protected edge phenomena. Unlike fermions, which can form Interger Quantum Hall states by simply filling noninteracting Chern bands thanks to the Pauli exclusion principle, free bosons in a magnetic field can only condensate into the lowest energy single-particle state. Therefore, for lattice boson models with flux, strong interactions are strictly necessary to stabilize any incompressible topological liquid. Depending on the filling factor and interaction strength, bosons can form a Bosonic Integer Quantum Hall (BIQH) state [63], a SPT phase, or a bosonic Fractional Quantum Hall (FQH) phase. The latter, being an intrinsic topological order, imposes additional stringent requirements on the band geometry (nonzero Chern number for the lowest bands, band flatness, and quasi-constant Berry curvature [64]) to prevent condensation and stabilize the long-range entangled fluid analogous to electronic FQH liquids.

Several papers have explored the emergence of topologically non-trivial phases in the Bose-Hubbard model frustrated with uniform magnetic flux [65, 66]. On the lattice, Peierls phases accumulated along hopping paths interfere destructively, leading to single particle bands that may acquire nonzero Chern number and, in suitable regimes, become nearly dispersionless. This band-flattening mechanism enhances the relative importance of interactions and provides a route toward strongly correlated topological phases.
Knap et al. [67] numerically investigate the model with $\Phi = \pi/3$ near the first Mott lobe and identify several topologically non-trivial phases using infinite DMRG (iDMRG) on cylinder geometries. In contrast with the algorithm we employed in the previous section, iDMRG extends DMRG to the thermodynamic limit by iteratively enlarging and optimizing a repeating unit cell. Their study is of particular interest because no spatial anisotropy is introduced in the Hamiltonian: hopping strength is the same for every bond and only on-site interactions are considered. Their characterization relies on three many-body diagnostics: flux-threading (charge-pumping) to extract the quantized Hall conductance, finite-size scaling of von Neumann entropies to estimate the topological entanglement entropy (TEE), and momentum-resolved entanglement spectrum counting to be compared with the multiplicity sequence of the candidate chiral edge CFT. The main candidate phases reported are the following.

1. a Laughlin-type FQH state at bosonic filling $\nu = 1/2$ (and its hole conjugate near the $n = 1$ Mott lobe), identified by half-charge pumping per flux quantum and a TEE consistent with the expected value of $\ln \sqrt{2}$. This is an intrinsically topologically ordered phase with Abelian statistics;

2. a Bosonic Integer Quantum Hall (BIQH) candidate at $\nu = 2$, signaled by an integer Hall response but vanishing TEE, consistent with a SPT/invertible identification;

3. Moore-Read (MR) state [68] candidate at $\nu = 1$ in selected parameter regimes (low-intermediate interactions), supported by an entanglement spectrum counting compatible with the appropriate topological sector. This is an example of intrinsic topological order with non-Abelian statistics (due to its Ising anyon content).

The authors emphasize finite-circumference and bond-dimension limitations: entanglement-based extrapolations and entanglement-spectrum counting are fragile for non-Abelian candidates and for hole states at weaker interactions. Because of these constraints, the mapping between these microscopic states and the macroscopic phases is best viewed as a plausible interpretation rather than an unequivocal fact. Nevertheless, this and related studies on 2-leg ladders [69, 70] provide

strong evidence that the flux-frustrated Bose-Hubbard model can host Quantum Hall-like topological phases without introducing additional interactions or modifying the underlying Hamiltonian. This supports the bottom-up realization of topological phenomena in minimal lattice models.

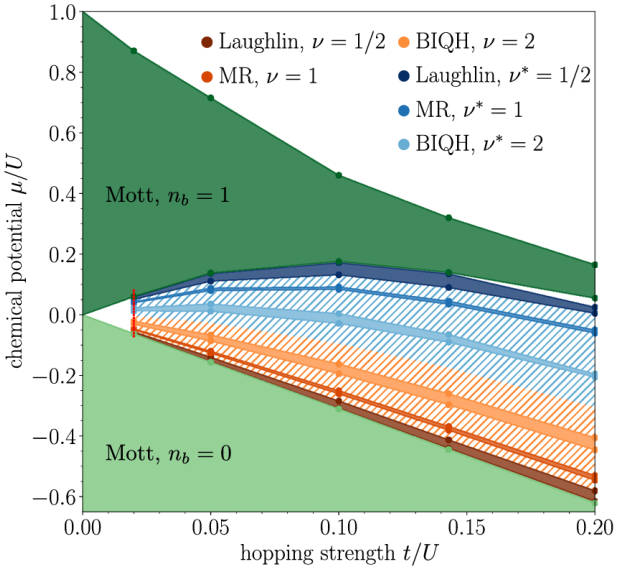

Figure 2.11: Phase diagram of the Bose-Hubbard model with $\Phi = \pi/3$ flux per plaquette on an infinite cylinder with circumference $L_y = 6$, focused on the area between the vacuum and the first Mott lobe (in the t/U-μ/U plane). Selected gapped states with filling factors $\nu = 1/2$, 1, 2 are tracked as a function of the hopping strength via infinite-DMRG simulations. Hatched areas are expected to contain further non-trivial gapped states.

Chapter 3

Two-plaquette BBH model

In the previous chapter, we introduced the Bose-Hubbard model with a uniform magnetic flux and surveyed the many-body phases that can arise in this setting. We now focus on the special case of π-flux per plaquette. This choice is motivated by the aim of perturbing the model as little as possible while still allowing for non-trivial magnetic effects. In particular, a π-flux configuration preserves time-reversal symmetry at the level of the microscopic Hamiltonian (which remains real as in the standard Bose-Hubbard model), thereby opening the possibility of spontaneous time-reversal symmetry breaking by the many-body ground state. This feature makes the π-flux choice a natural starting point for exploring the emergence of chiral or topological responses in minimally modified lattice models, even though no topological phase will ultimately be explored in the present work.

The central model of this thesis is the dimerized version of the π-flux Bose-Hubbard system, namely the bosonic Benalcazar-Bernevig-Hughes (BBH) ladder with alternating hoppings J and J' [19]. To investigate its low-energy physics in a controlled manner, we begin by analyzing a minimal building block: two adjacent plaquettes with the intra-plaquette hopping J, coupled by the inter-plaquette hopping J'. A visual representation of this setup will be shown later in Fig. 3.2. This dimerization allows to tune the hybridization of the low-energy states of neighboring plaquettes while preserving their internal structure. In the weak inter-plaquette coupling regime $J'/J \ll 1$, the local states of each plaquette remain well-defined, and the global behavior can be treated as a perturbative extension of the physics of isolated plaquettes. Maintaining a connection to this plaquette-based description provides insight into the relation between vortex physics and p-band physics. As shown by Di Liberto and Goldman [14], the effective low-energy description of a single plaquette naturally links the emergence of vortex order to the angular momentum carried by its low-energy orbitals. It is therefore instructive to examine how these local chiral degrees of freedom interact and hybridize when plaquettes are coupled.

The first goal of this chapter is to characterize the spectrum and relevant observables of the two-plaquette system through exact diagonalization, identifying distinctive features and their dependence on the inter-plaquette hopping amplitude J', and on-site interaction strength U, for fixed J. This will be the starting point for the mean-field treatment of an extend ladder system with the cluster-Gutzwiller ansatz [20]. We then analyze the same quantities using two different effective low-energy theories: one formulated in terms of the single-plaquette, low-energy single-particle orbitals, and another based on the low-energy single-particle orbitals of the coupled two-plaquette system, going beyond the perturbative treatment of J'. The aim is to determine whether the more detailed two-plaquette effective theory captures features of the exact solution that are inaccessible in the single-plaquette approach.

A lighter notation is adopted in the remainder of the thesis by omitting the hat symbol ($\hat{}$) on operators.

3.1 BBH model

We now introduce the explicit lattice formulation of the dimerized π-flux Bose-Hubbard model discussed above. We consider a finite region of the two-dimensional plane tessellated by square plaquettes, each threaded by a uniform π-flux. Building upon the construction of the Bose-Hubbard model in presence of a magnetic field, we now introduce the explicit lattice formulation of the two-dimensional plane tessellated by square plaquettes, each threaded by a uniform π-flux. As anticipated above, we specifically distinguish between intra-plaquette and inter-plaquette hopping amplitudes: this geometry evolves into the foundational framework of the Benalcazar-Bernevig-Hughes (BBH) model [19].
The 2D BBH Hamiltonian in Landau gauge takes the following form:

$$H = -\sum_{x,\,y}\left(t_x b^{\dagger}_{x+1,y}\, b_{x,y} + \text{h.c.}\right) + \sum_{x,\,y}\left((-1)^x t_y\, b^{\dagger}_{x,y+1}\, b_{x,y} + \text{h.c.}\right) + \sum_{x,\,y}\left[\frac{U}{2} n_{x,y}(n_{x,y}-1) - \mu\, n_{x,y}\right],$$

$$\text{with} \qquad t_{x(y)} = \begin{cases} J & \text{if } x(y) \text{ is even}\,, \\ J' & \text{if } x(y) \text{ is odd}\,. \end{cases} \tag{3.1}$$

Here each lattice site is labeled with discrete coordinates (x, y), and $(-1)^x$ enforces the π-flux as specified by the gauge choice.

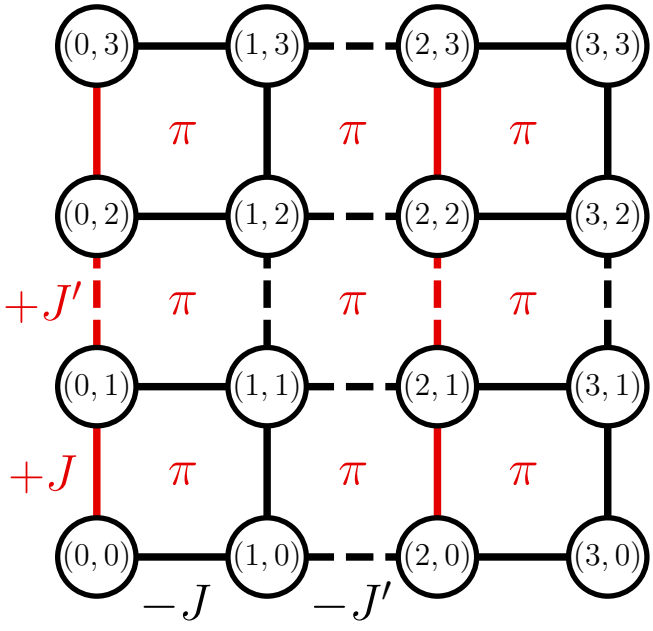

Figure 3.1: Graphical representation of a patch of the 2D BBH model in Landau gauge. Intra-plaquette bonds ($\pm J$) are shown as solid lines, inter-plaquette couplings ($\pm J'$) as solid lines, and lattice sites are represented by empty circles. Links colored in red carry the sign change to implement π-flux.

For the fermionic version of the model, the structural dimerization of the bonds is the key feature enabling the transition from first-order symmetry-protected topological effects, where non-trivial responses reside in the $(d-1)$-dimensional edge of the d-dimensional system, to higher-order

topological phases, where the topological signatures are pushed down to dimension $d-2$, at the zero-dimensional corners [19]. This generalizes the bulk-boundary correspondence to higher-order topology [71]: the (d)-dimensional bulk protects gapless states on the $(d-2)$-dimensional hinges (or corners), while the $(d-1)$-dimensional boundaries are gapped. The fermionic BBH model realizes a Higher Order Topological Insulators (HOTI) exhibiting a quantized bulk quadrupole moment protected by crystalline mirror symmetries, gapped one-dimensional edges and zero-dimensional topologically protected corner states carrying fractional charge. The choice of π-flux is essential because it ensures that mirror symmetries along the x and y axes anti-commute, $\{M_x\,,\ M_y\} = 0$, a requirement to protect the multipole moment [72]. In the non-interacting case ($U = 0$), topology is a single-particle property of the fermionic band structure, while the bosonic system is unstable toward the formation of a superfluid phase (Bose-Einstein condensate), which lacks the requisite bulk gap for topological protection. Adding on-site interactions could make HOTI accessible also for bosons, potentially stabilizing the Higher Order Topological Mott Insulator (HOTMI) proposed in Ref. [73] for interacting fermions. In this phase, the system maintains its topological properties even when the single-particle gap is absent or ill-defined, because they are protected by the many-body gap and the many-body symmetries.

The phase landscape of the bosonic BBH model analyzed here is determined by the interplay between the kinetic energy scales (J and J'), the on-site repulsion U and the synthetic π-flux. At zero temperature, the competition among these terms drives the system through distinct macroscopic states, characterized by their symmetry-breaking pattern and, for the topologically non-trivial ones, their topological invariants. We say that a symmetry of the Hamiltonian is spontaneously broken at the quantum level when the system is characterized by nonzero long-range correlator of an operator that is not invariant under that symmetry. For time-reversal symmetry, currents are odd under the transformation because they carry a definite orientation. A finite long-range current-current correlator, therefore, signals time-reversal breaking, and the system is then said to exhibit chiral order. Here after we describe the well-established phases for the bosonic BBH model within this classification.

- Superfluid (SF) phase. For weak interactions ($U \lesssim J,\ J'$), the kinetic energy dominates. The bosons delocalize across the lattice and undergo Bose-Einstein condensation. This phase is characterized by spontaneous symmetry breaking of the global $U(1)$ symmetry, Goldstone gapless excitations, and long-range phase coherence. Because the bulk is gapless, topological invariants are ill-defined, and the system lacks topological protection.

- Chiral superfluid phase. In the presence of currents with shared orientation along the lattice or correlated at long distances, the superfluid phase breaks the explicit time-reversal symmetry of the BBH Hamiltonian and acquires a chiral connotation.

- Trivial Mott insulator (MI). As the on-site repulsion U is increased beyond a critical threshold, and for commensurate fillings, the system undergoes a Superfluid-Mott transition. When the intra-plaquette hopping dominates the inter-plaquette hopping ($J > J'$), the bosons localize tightly within the elementary unit cells. The bulk and edges are fully gapped, charge fluctuations are heavily suppressed, and the ground state is topologically trivial, lacking both edge and corner localized modes.

- Chiral Mott insulator (CMI). The interplay between frustration introduced by the π-flux and interactions can provide a mechanism for a spontaneous symmetry breaking. While the π-flux preserves time-reversal symmetry at the Hamiltonian level, the system can spontaneously break this symmetry to minimize its energy at intermediate interaction strengths, generating staggered, circulating loop currents of bosons across the plaquettes. In the absence of said currents, this phase can be identified by the nonvanishing value of the current-current

correlators. In this phase, the bulk remains an incompressible insulator, but the system can develop localized gapless chiral edge currents. If characterized by a nonzero Chern number, the CMI actually corresponds to a Chern insulating phase, and develops a type of topological order analogous to the Integer Quantum Hall, as reviewed in sections 2.5, 2.6.

Henceforth, we restrict our analysis to the specific case of half filling, corresponding to an average boson density of $n = 0.5$. Because the structural dimerization of the BBH geometry defines a four-site unit cell, half filling corresponds to exactly two bosons per unit cell. This commensurability makes insulating phases accessible even at fractional density, in analogy with the flux-frustrated Bose-Hubbard model and in contrast to the standard Bose-Hubbard model.

3.2 Two-plaquette exact diagonalization

3.2.1 Description and graphical visualization

As a minimal building block for the analysis of the BBH model, we study two square plaquettes stacked along the y-direction and coupled by inter-plaquette tunneling. Each plaquette contains four sites and constitutes the unit cell. Fig. 3.2 shows an illustrative sketch of the model and specifies the site enumeration for the mapping to a one-dimensional chain with nearest neighbor and next-to-nearest neighbor hopping. Using two plaquettes goes beyond the single-plaquette description of recent studies [14, 74], allowing inter-plaquette currents and correlations that cannot appear in a single-cell model. This enlarged cluster is therefore the minimal extension to the setup needed to capture chiral ordering in the BBH system.

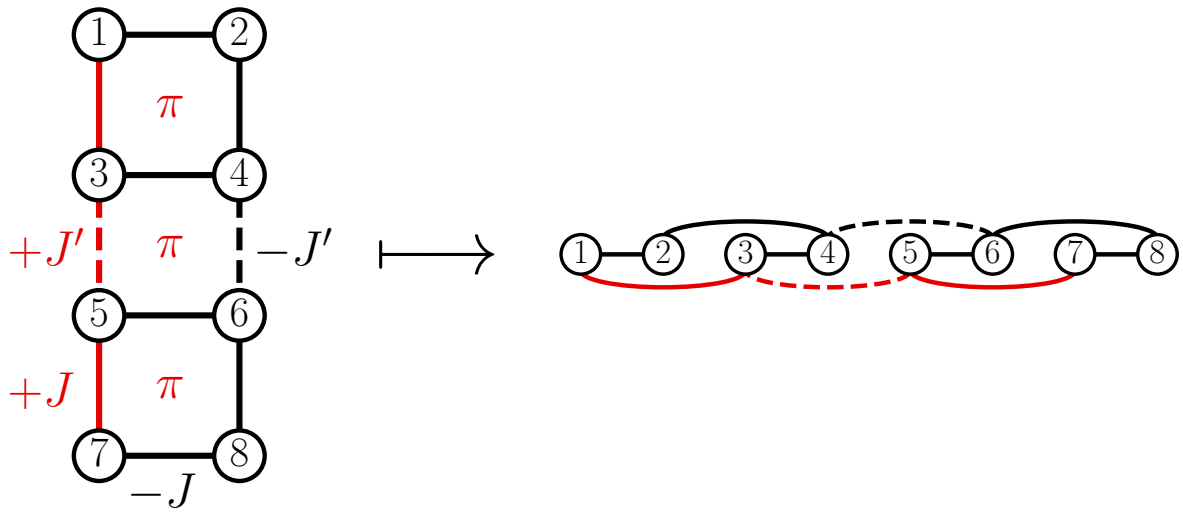

Figure 3.2: Graphical representation of the system under study: two plaquettes linked by a different hopping amplitude. Intra-plaquette bonds ($\pm J$) are shown as solid lines, inter-plaquette couplings ($\pm J'$) as solid lines, and lattice sites are represented by empty circles. Links colored in red carry the sign change to implement π-flux as specified by Landau gauge. Left: the original system embedded in a 2D plane. Right: its mapping to a one-dimensional chain.

As depicted in Fig. 3.2, the first plaquette is formed by sites 1–2–4–3 and the second by 5–6–8–7. Hopping amplitudes implement a π-flux per plaquette by including sign changes on specified links. We study the system at half filling ($n = 0.5$). With a fixed particle number sector, we work in the canonical ensemble, neglecting the chemical potential contribution. We split the tight-binding

Hamiltonian into its hopping and interaction parts, H_0 and H_{int}:

$$H_{\text{exact}} = H_0 + H_{\text{int}} = H_0 + \frac{U}{2}\sum_i n_i\big(n_i - 1\big)\,. \tag{3.2}$$

with $n_i = b_i^\dagger b_i$ the number operator acting on the site i. The hopping term is

$$H_0 = -\sum_{\langle ij\rangle} t_{ij}\, b_i^\dagger b_j + \text{h.c.}\,, \tag{3.3}$$

set by the following nonzero hopping strengths

$$\begin{aligned} &t_{12} = t_{24} = t_{34} = t_{56} = t_{68} = t_{78} = J\,, \\ &t_{13} = t_{57} = e^{i(\pi+\delta\phi)}J = -e^{i\delta\phi}J\,, \\ &t_{46} = J'\,, \\ &t_{35} = e^{i(\pi+\delta\phi)}J' = -e^{i\delta\phi}J'\,, \end{aligned} \tag{3.4}$$

contains a small flux shift $\delta\phi$ which is eventually introduced to weakly break time-reversal symmetry and make the equilibrium currents observable. At exactly π-flux, the Hamiltonian is strictly time-reversal symmetric, and the ground state forms an equal superposition of states with opposite chirality. This symmetric combination suppresses all one-body correlations (currents), even though two-body correlations remain finite. By applying a nonzero $\delta\phi$, we lift this degeneracy and reveal the current response of the system. Unless explicitly stated we set $\delta\phi = 0$.
We can in turn write the hopping term H_0 as the sum of an intra-plaquette Hamiltonian H_J, and an inter-plaquette Hamiltonian $H_{J'}$, $H_0 = H_J + H_{J'}$. The single-particle matrix representation of these operators takes the following form:

$$H_0 = J\begin{pmatrix} 0 & -1 & 1 & 0 & 0 & 0 & 0 & 0 \\ -1 & 0 & 0 & -1 & 0 & 0 & 0 & 0 \\ 1 & 0 & 0 & -1 & 0 & 0 & 0 & 0 \\ 0 & -1 & -1 & 0 & 0 & 0 & 0 & 0 \\ 0 & 0 & 0 & 0 & 0 & -1 & 1 & 0 \\ 0 & 0 & 0 & 0 & -1 & 0 & 0 & -1 \\ 0 & 0 & 0 & 0 & 1 & 0 & 0 & -1 \\ 0 & 0 & 0 & 0 & 0 & -1 & -1 & 0 \end{pmatrix} + J'\begin{pmatrix} 0 & 0 & 0 & 0 & 0 & 0 & 0 & 0 \\ 0 & 0 & 0 & 0 & 0 & 0 & 0 & 0 \\ 0 & 0 & 0 & 0 & 1 & 0 & 0 & 0 \\ 0 & 0 & 0 & 0 & 0 & -1 & 0 & 0 \\ 0 & 0 & 1 & 0 & 0 & 0 & 0 & 0 \\ 0 & 0 & 0 & -1 & 0 & 0 & 0 & 0 \\ 0 & 0 & 0 & 0 & 0 & 0 & 0 & 0 \\ 0 & 0 & 0 & 0 & 0 & 0 & 0 & 0 \end{pmatrix} =$$

$$= J\begin{pmatrix} 0 & -1 & 1 & 0 & 0 & 0 & 0 & 0 \\ -1 & 0 & 0 & -1 & 0 & 0 & 0 & 0 \\ 1 & 0 & 0 & -1 & r & 0 & 0 & 0 \\ 0 & -1 & -1 & 0 & 0 & -r & 0 & 0 \\ 0 & 0 & r & 0 & 0 & -1 & 1 & 0 \\ 0 & 0 & 0 & -r & -1 & 0 & 0 & -1 \\ 0 & 0 & 0 & 0 & 1 & 0 & 0 & -1 \\ 0 & 0 & 0 & 0 & 0 & -1 & -1 & 0 \end{pmatrix}, \quad \text{where } r \text{ is the ratio } r = \frac{J'}{J}. \tag{3.5}$$

Diagonalizing the isolated-plaquettes Hamiltonian H_J ($r = 0$) yields a discrete, degenerate single-particle spectrum. The π-flux configuration gaps the individual plaquettes, producing doubly degenerate energy levels at $\varepsilon^{O(r^0)} = \pm\sqrt{2}J$ for each plaquette. For the two-plaquette geometry, this results in a four-fold degeneracy for each energy sector, as shown in Fig. 3.3:

$$\sigma(H_J) = \big\{-\sqrt{2}J \text{ (multiplicity 4)},\ +\sqrt{2}J \text{ (multiplicity 4)}\big\}\,. \tag{3.6}$$

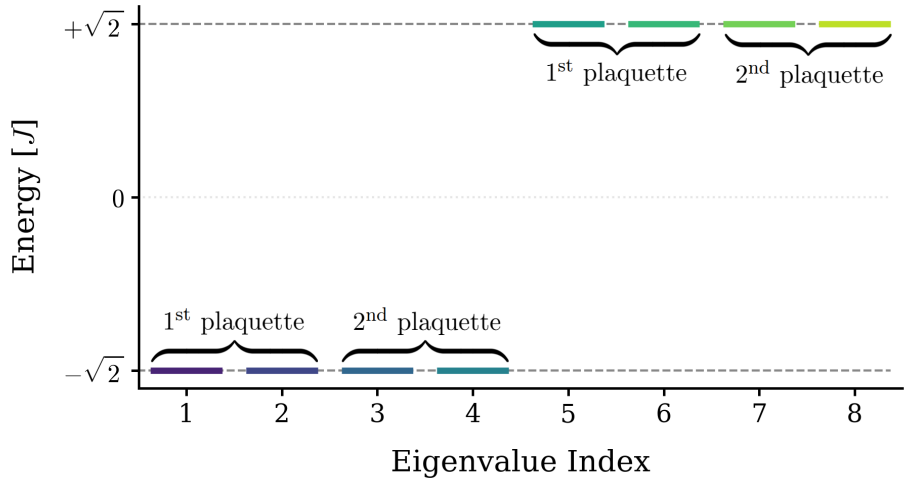

Figure 3.3: Full single-particle spectrum of two isolated-plaquettes hamiltonian in Eq.(3.5) for $r = 0$.

Introducing the inter-plaquette coupling $H_{J'}$ ($r \neq 0$) hybridizes the individual blocks and partially lifts this degeneracy. A finite coupling ratio r splits the original degenerate levels into pairs while maintaining the gap $\propto J$. The full non-interacting Hamiltonian H_0 shows sublattice (also called chiral) symmetry (see the next subsection for a proper definition). Consequently, the single-particle spectrum of H_0 is perfectly symmetric around zero energy ($\varepsilon \leftrightarrow -\varepsilon$).

$$
\begin{aligned}
\varepsilon_1 = \varepsilon_2 &= -\frac{J}{\sqrt{2}}\sqrt{r\left(r+\sqrt{r^2+4}\right)+4} \equiv \varepsilon_L, \\
\varepsilon_3 = \varepsilon_4 &= -J\frac{\sqrt{2}}{\sqrt{\dfrac{r}{\sqrt{r^2+4}}+1}} \equiv \varepsilon_H, \\
\varepsilon_5 = \varepsilon_6 &= J\frac{\sqrt{2}}{\sqrt{\dfrac{r}{\sqrt{r^2+4}}+1}} \\
\varepsilon_7 = \varepsilon_8 &= \frac{J}{\sqrt{2}}\sqrt{r\left(r+\sqrt{r^2+4}\right)+4},
\end{aligned}
\tag{3.7}
$$

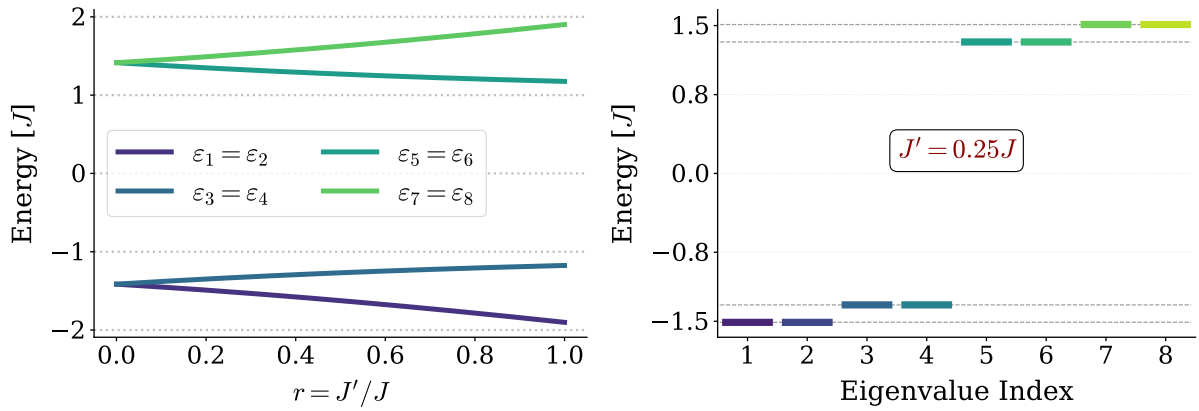

Figure 3.4: Single-particle spectrum of H_0. Left: the spectrum as a function of the adimensional inter-plaquette coupling $r = J'/J$. Right: the spectrum for fixed $J' = 0.25J$ to help visualize the residual degeneracy.

The eight energy levels are shown in Fig. 3.4 as a function of the adimensional inter-plaquette coupling $r = J'/J$ (left). A finite inter-plaquette coupling $r > 0$ partially lifts the degeneracy associated with the two isolated-plaquettes Hamiltonian H_J ($r = 0$). In fact, we observe that the fourfold degeneracy discussed previously in Fig.3.3 splits into two twofold degenerate subspaces, with an induced splitting proportional to $r = J'/J$.

3.2.2 Model symmetries and symmetry-related observables

In the previous section, we stated that the non-interacting Hamiltonian H_0 shows the signatures of a sublattice symmetry. A non interacting system manifests this spectral symmetry if there exists a unitary, Hermitian operator $\mathcal{C}$ that anticommutes with the Hamiltonian,

$$\{H_0, \mathcal{C}\} = H_0\mathcal{C} + \mathcal{C}H_0 = 0\,. \tag{3.8}$$

In the BBH model, the lattice is strictly bipartite: sites can be partitioned into two distinct sublattices, A and B, such that all nonzero hopping amplitudes strictly connect an A site to a B site. Consequently, the operator $\mathcal{C}$ is diagonal in the site basis, taking the value $+1$ on sublattice A and -1 on sublattice B. The anticommutation relation ensures that if $|\psi\rangle$ is a single-particle eigenstate of H_0 with energy E, then $\mathcal{C}|\psi\rangle$ is also an eigenstate with energy $-E$:

$$H_0(\mathcal{C}|\psi\rangle) = -\mathcal{C}H_0|\psi\rangle = -E(\mathcal{C}|\psi\rangle)\,. \tag{3.9}$$

This rigorously justifies the property mentioned in the previous subsection: the single-particle energy spectrum of H_0 is perfectly symmetric around zero energy ($E \leftrightarrow -E$). Note that chiral symmetry is a property of the hopping matrix, and including the many-body interaction term H_{int} generally breaks this spectral symmetry for the full many-body spectrum.
As already mentioned, the Benalcazar-Bernevig-Hughes model is invariant under time reversal symmetry $\mathcal{T}: t \mapsto -t$, namely,

$$H \mapsto H' = \mathcal{T}H\mathcal{T}^{-1} = H \iff \big[H, \mathcal{T}\big] = 0\,. \tag{3.10}$$

This follows from the same arguments discussed in section 2.3.
Another defining feature of the BBH model is its crystalline protection via mirror (reflection) symmetries. In two spatial dimensions, we define two primary reflection axes:

- M_x reflection. Maps $x \mapsto -x$ across the vertical axis bisecting the lattice;
- M_y reflection. Maps $y \mapsto -y$ across the central horizontal axis.

Due to the presence of π-flux, the representation of these operators on the Hilbert space is non-trivial and depends on the gauge chosen to encode the magnetic field (gauge dressing) [72]. For the two-plaquette cluster with the specified implementation of Landau gauge, the single-particle matrix representation of the mirror symmetries, up to a global phase re-shift, takes the following form:

$$M_x = \begin{pmatrix} 0 & -1 & 0 & 0 & 0 & 0 & 0 & 0 \\ -1 & 0 & 0 & 0 & 0 & 0 & 0 & 0 \\ 0 & 0 & 0 & 1 & 0 & 0 & 0 & 0 \\ 0 & 0 & 1 & 0 & 0 & 0 & 0 & 0 \\ 0 & 0 & 0 & 0 & 0 & -1 & 0 & 0 \\ 0 & 0 & 0 & 0 & -1 & 0 & 0 & 0 \\ 0 & 0 & 0 & 0 & 0 & 0 & 0 & 1 \\ 0 & 0 & 0 & 0 & 0 & 0 & 1 & 0 \end{pmatrix}, \qquad M_y = \begin{pmatrix} 0 & 0 & 0 & 0 & 0 & 0 & 1 & 0 \\ 0 & 0 & 0 & 0 & 0 & 0 & 0 & 1 \\ 0 & 0 & 0 & 0 & 1 & 0 & 0 & 0 \\ 0 & 0 & 0 & 0 & 0 & 1 & 0 & 0 \\ 0 & 0 & 1 & 0 & 0 & 0 & 0 & 0 \\ 0 & 0 & 0 & 1 & 0 & 0 & 0 & 0 \\ 1 & 0 & 0 & 0 & 0 & 0 & 0 & 0 \\ 0 & 1 & 0 & 0 & 0 & 0 & 0 & 0 \end{pmatrix}. \tag{3.11}$$

A direct calculation gives $\{M_x, M_y\} = M_x M_y + M_y M_x = 0$.
The many-body representation of the two symmetry operators is block-diagonal in the total particle number N basis. Each block acts within a fixed N-sector and is obtained from the single-particle matrices above by their natural extension to the N-particle Hilbert space. Equivalently, the full operator $M^{\text{full}}_{x(y)}$ is the direct sum over N of the sector matrices,

$$M^{\text{full}}_{x(y)} = \bigoplus_N M^{(N)}_{x(y)}, \tag{3.12}$$

where $M^{(N)}_{x(y)}$ is the matrix representing the symmetry on the N-particle subspace, with $M^{(N=1)}_{x(y)} = M_{x(y)}$. The two operators generate the full lattice symmetry group, i.e. every lattice symmetry can be written as a product of M^{full}_x and M^{full}_y.
In the two-plaquette system, reflections partition the sites into two symmetry-equivalent sets: $\mathcal{S}_1 = \{1, 2, 7, 8\}$, the 'border' sites and $\mathcal{S}_2 = \{3, 4, 5, 6\}$, the 'internal' sites, as shown in Fig. 3.5. Accordingly, we expect their densities to be equal and monitor the observable density imbalance defined as:

$$\Delta n \equiv \frac{1}{4}\sum_{i\in\mathcal{S}_1}\langle n_i\rangle \;-\; \frac{1}{4}\sum_{i\in\mathcal{S}_2}\langle n_i\rangle\,. \tag{3.13}$$

Similarly, directed bonds $i \to j$ are categorized into three symmetry classes: border ($\mathcal{B}$), internal ($\mathcal{I}$), and vorticity ($\mathcal{V}$), defined by the sets

$$\begin{aligned}
\mathcal{B} &= \{1\to 2,\;\; 3\to 1,\;\; 2\to 4,\;\; 8\to 7,\;\; 6\to 8,\;\; 7\to 5\}\,,\\
\mathcal{I} &= \{4\to 3,\;\; 5\to 6\}\,,\\
\mathcal{V} &= \{5\to 3,\;\; 4\to 6\}\,.
\end{aligned} \tag{3.14}$$

The local observable for each bond ℓ is the directed current J_ℓ of Eq. (2.15). The averaged observables for each class are

$$J_{\mathcal{B}} \equiv \frac{1}{6}\sum_{\ell\in\mathcal{B}}\langle J_\ell\rangle\,, \qquad J_{\mathcal{I}} \equiv \frac{1}{2}\sum_{\ell\in\mathcal{I}}\langle J_\ell\rangle\,, \qquad J_{\mathcal{V}} \equiv \frac{1}{2}\sum_{\ell\in\mathcal{V}}\langle J_\ell\rangle\,, \tag{3.15}$$

with $J_{\mathcal{I}} = J_{\mathcal{B}} + J_{\mathcal{V}}$, due to the particle number conservation. Δn probes charge imbalance between site groups, $J_{\mathcal{B}}$ and $J_{\mathcal{I}}$ distinguish edge from bulk transport, and $J_{\mathcal{V}}$ measures the current exchange between the plaquettes.

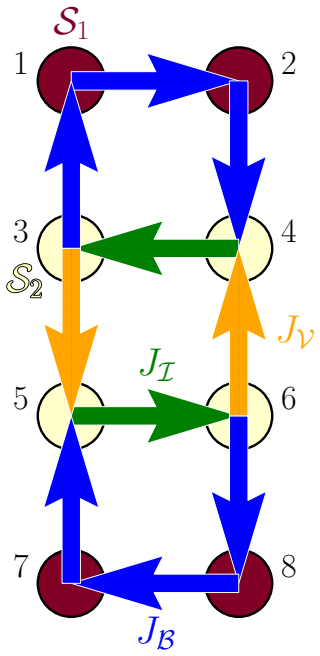

Figure 3.5: Color-coded graphical representation of the symmetry-related observables in the two-plaquette BBH system. Densities of sites in set $\mathcal{S}_1$ are dark red, those of sites in $\mathcal{S}_2$ faint yellow. Border currents $J_{\mathcal{B}}$ are blue, internal currents $J_{\mathcal{I}}$ green, while vorticity currents $J_{\mathcal{V}}$ orange.

With these definitions, the loop currents in each plaquette can be expressed in terms of the symmetry-averaged bond currents as:

$$\langle J_{\square}^{P1} \rangle = \frac{1}{4}\langle J_{1\to2} + J_{2\to4} + J_{4\to3} + J_{3\to1} \rangle = \frac{3}{4}J_{\mathcal{B}} + \frac{1}{4}J_{\mathcal{I}} = J_{\mathcal{B}} + \frac{1}{4}J_{\mathcal{V}}\,, \tag{3.16}$$

$$\langle J_{\square}^{P2} \rangle = \frac{1}{4}\langle J_{5\to6} + J_{6\to8} + J_{8\to7} + J_{7\to5} \rangle = \frac{3}{4}J_{\mathcal{B}} + \frac{1}{4}J_{\mathcal{I}} = J_{\mathcal{B}} + \frac{1}{4}J_{\mathcal{V}}\,, \tag{3.17}$$

where the factor 1/4 is included to normalize the current over the four bosons in the eight-sites configuration. Note, that $J_{\square}^{P_1}$ and $J_{\square}^{P2}$ remain distinct local operators; symmetry implies $\langle J_{\square}^{P_1} \rangle = \langle J_{\square}^{P_2} \rangle$, but does not force their correlator to vanish. As stated earlier, equilibrium currents become visible only when the system is perturbed by a nonzero flux shift ($\delta\phi \neq 0$). We monitor the connected correlator of the loop currents on the two plaquettes,

$$\langle J_{\square}^{P1} J_{\square}^{P2} \rangle_c = \langle J_{\square}^{P1} J_{\square}^{P2} \rangle - \langle J_{\square}^{P1} \rangle \langle J_{\square}^{P2} \rangle\,. \tag{3.18}$$

This observable captures the relative alignment of the phase winding of the many-body wavefunction in each plaquette and therefore provides information about the underlying chiral order for eventual spontaneous symmetry breaking ground state. It is particularly valuable at $\delta\phi = 0$, where time-reversal symmetry forces the expectation value of each individual plaquette current to vanish, but their correlations remain sensitive to the structure of the chiral ordered ground state. In this case, one simply has $\langle J_{\square}^{P1} J_{\square}^{P2} \rangle_c = \langle J_{\square}^{P1} J_{\square}^{P2} \rangle$, but introducing the connected form is convenient for continuity with the analysis in the following chapter.

3.2.3 Many-body spectrum

To investigate the effects of interactions on the bosonic BBH system, we perform exact diagonalization (ED) of the full many-body Hamiltonian H_{exact}. The system consists of $N_S = 8$ sites with

an average density of half a particle per site, corresponding to a total particle number $N = 4$. The maximum possible occupation of any single site is $n_{\max} = 4$, which truncates the local Hilbert space dimension to $d = 5$. The total dimension of the many-body Hilbert space is given by the binomial coefficient $\binom{N_S+N-1}{N} = 330$. We explicitly construct the Hamiltonian matrix in the Fock basis and obtain the full energy spectrum using the QuSpin open-source Python package [75]. To track the continuous evolution of individual eigenstates as a function of interaction strength U/J, we match energy levels by maximizing the fidelity $|\langle\Psi_n(U)|\Psi_m(U+\delta U)\rangle|$, with m, n excitation indices.δU is $3 \cdot 10^{-3} J$, meaning that we are computing the fidelity between eigenvectors evaluated at consecutive, closely spaced values of U. This state-tracking procedure uniquely identifies continuous spectral trajectories, allowing us to follow how specific states evolve, split, or undergo avoided crossings as interactions are varied. Unless specified, the states labeled by $m = 1, \ldots, 8$ correspond to the eight-lowest energy states in the weakly interacting regime ($U/J \sim 0.003$), and are then continuously tracked as we vary system parameters. We denote many-body energies as E to distinguish them from single-particle energies (ε). The numerical results presented here are obtained for a fixed inter-plaquette coupling of $J' = 0.25J$.

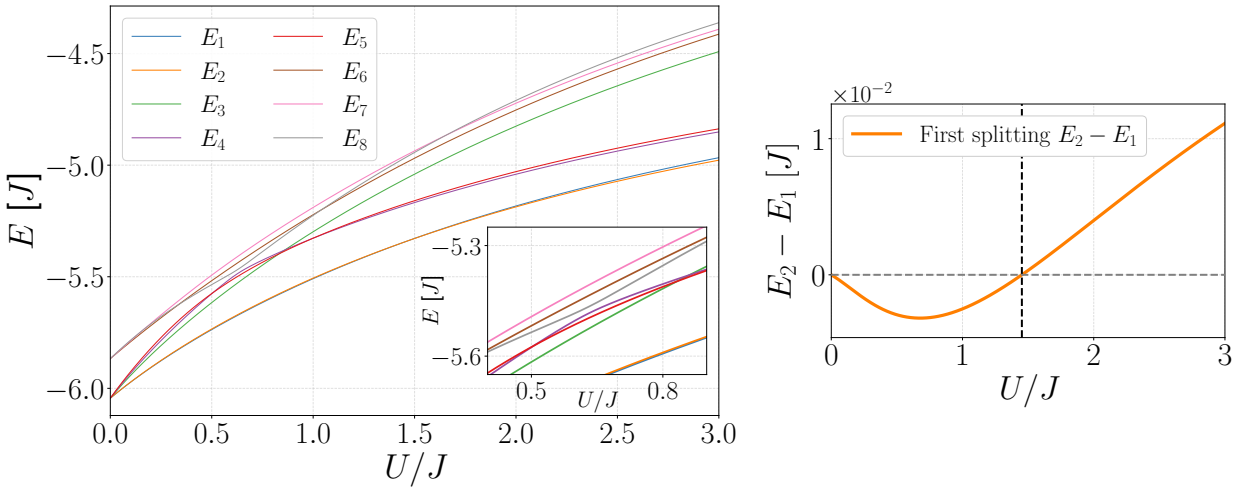

Figure 3.6: Many-body spectrum of the two-plaquette BBH model for $J' = 0.25J$ at half filling. Left: lowest eight energy levels as a function of interaction strength U/J. The inset displays a zoom of the region $U/J \in [0.4, 0.9]$ highlighting an avoided crossing between the fifth and sixth excited states. Right: energy splitting between the ground state and first excited state as a function of U/J. The vertical line highlights the value of U/J at which the splitting crosses zero, estimated by linear interpolation between the points where the splitting changes sign at $U/J \simeq 1.452$, with $\Delta U/J = 5 \cdot 10^{-3}$ between consecutive data points collected.

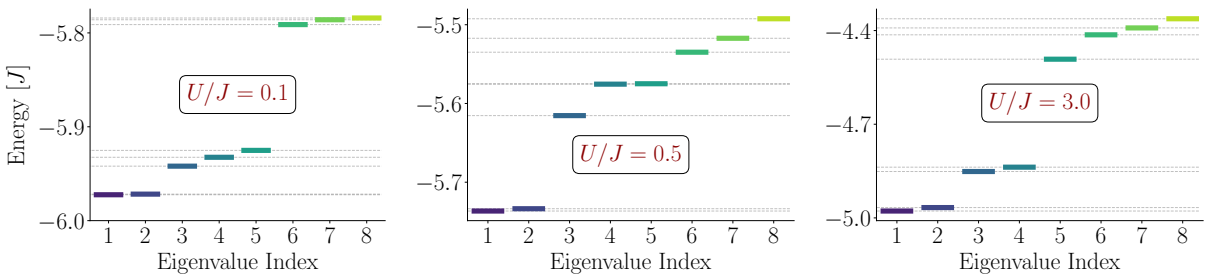

Figure 3.7: Many-body spectrum of the two-plaquette BBH model. Lowest eight energy levels for $J' = 025J$ at fixed values of U/J: 0.1 (left), 0.5 (center), and 3.0 (right). These panels correspond to vertical cuts through the full spectrum shown in Fig. 3.6 and highlight level splittings that are difficult to resolve in the main plot.

The exact many-body spectrum exhibits a clear hierarchy of energy scales. As shown in Fig. 3.6, the lowest two eigenstates, E_1 and E_2, form a quasi-degenerate low-energy manifold. This pair of states remains separated from the higher-energy excited states by an energy gap of order J' across the entire investigated interaction range from $U/J = 0$ to 3. Focusing on the low-energy manifold, we track the states by their overlap to observe the evolution of the first energy splitting, defined as $E_2 - E_1$. The behavior of this splitting is non-trivial. Starting from a degenerate configuration at U = 0, the splitting initially dips, indicating that the tracked state called E_2 drops below E_1 in energy. The energy difference reaches a local minimum before turning upwards and crossing exactly through zero. This zero-crossing represents an exact level crossing between the ground state and the first excited state, meaning that at this point the ground state is degenerate. Beyond this specific interaction strength, $U \simeq 1.452J$, the splitting grows steadily and almost linearly. Accurately capturing this level crossing and the magnitude of the splitting (which is on the order of 10^{-2} J) will be a primary quantitative test for our effective theories.
In addition to the ground-state evolution, the exact spectrum features show internal structures within the higher-energy manifold. Notably, there is a clear avoided crossing between higher excited states, highlighted in the inset of Fig. 3.6 (left) for U/J between 0.5 and 0.8 and energies around $-5.3J$. While the explicit dynamics of these highly excited states are not the primary focus of our low-energy analysis, the ability of an effective theory to retain or wash out such features serves as a useful qualitative benchmark for evaluating the limits of the chosen approximation scheme.
To further illustrate the spectral hierarchy, we examine cuts of the many-body spectrum at fixed interaction strengths ($U/J = 0.1$, 0.5, and 3.0), shown in Fig. 3.7. At weak interactions ($U/J = 0.1$, left panel), the system strongly resembles the non-interacting limit, characterized by tightly clustered energy levels. As the on-site repulsion increases ($U/J = 0.5$, $U/J = 3.0$ center and right panels), the internal splittings within both the low-energy doublet and the higher-excited manifold grow significantly, reflecting the increasing energetic cost of multi-particle occupation.

3.2.4 Properties of the many-body ground state

To complete the analysis of the exact model, we investigate the chiral current patterns emerging in the two-plaquette system under a symmetry-breaking flux perturbation $\delta\phi$. The resulting current distributions exhibit non-trivial, non-monotonic behaviors that are intimately linked to the closing of the energy gap between the ground state (E_1) and the first excited state (E_2)

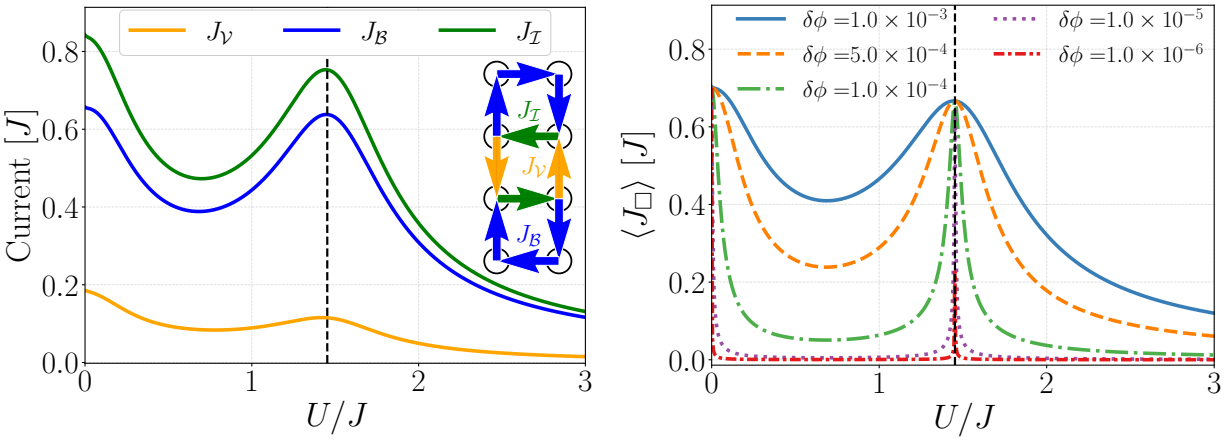

Figure 3.8: Currents in the model perturbed by a symmetry-breaking flux shift. The system consists of four bosons on eight sites forming two square plaquettes linked by inter-plaquette hopping strength $J' = 0.25J$. Left: Border, internal and vorticity currents as a function of U/J for a flux shift of $\delta\phi = 10^{-3}$. The inset defines the current labels and their orientations on the lattice. Right: Loop current $J_\square = \langle J_\square^{P1} \rangle = \langle J_\square^{P2} \rangle$ versus U/J for several values of the flux shift $\delta\phi \in \{10^{-3}, 2 \cdot 10^{-4}, 10^{-4}, 10^{-5}\, 10^{-6}\}$.
Both panels show a vertical line at $U \simeq 1.452J$, where the first excitation gap closes. This point closely coincides with the peak of the currents.

As illustrated in the left panel of Fig. 3.8, the border ($J_{\mathcal{B}}$), internal ($J_{\mathcal{I}}$), and vorticity ($J_{\mathcal{V}}$) currents all follow a consistent, synchronized trend as a function of U/J. In particular, these currents maintain a constant sign throughout the investigated parameter regime, meaning they never reverse their orientation. This observation justifies a simplified loop-current description of the system. The currents consistently form vortex patterns with a closed orientation that is identical in both plaquettes (shown in the inset of Fig. 3.8). In this regime, the physical evolution of the system is not characterized by a change in the current pattern geometry, but rather by the modulation of the overall current magnitude as the interaction strength varies. The most prominent feature of the current response is the current revival occurring at intermediate interaction strengths. Rather than decaying monotonically with U/J, the currents show a substantial enhancement at intermediate interaction strengths. The peak of this revival is directly tied to the spectral properties of the system: in both the vorticity-border-internal currents plot (Fig. 3.8, left) and the loop current plot (Fig. 3.8, right), the current peaks at the vertical dashed line at $U \simeq 1.452J$. This line marks the exact point where the first excitation gap closes, indicating that the current revival is a macroscopic signature of the ground-state level crossing.
The right panel demonstrates the persistence of this phenomenon as the symmetry-breaking perturbation $\delta\phi$ is reduced toward the limit of zero flux. As $\delta\phi$ decreases, the current peak does not disappear; instead, it becomes increasingly localized and "sharpened" around the degeneracy point. This behavior hints at the fact that when the ground state is perfectly degenerate, the system spontaneously chooses one, organizing such that persistent currents are present despite the nominal restoration of time-reversal symmetry. The non-monotonic behavior thus reflects the high sensitivity of the many-body state to external perturbations when near a level crossing.

To understand whether the current revival is a mere artifact of the flux perturbation or a fundamental property of the many-body state, we examine the system in its unperturbed state ($\delta\phi = 0$). While the mean current is zero in this limit due to time-reversal symmetry, the underlying physics of the ground-state crossing manifests clearly through sharp discontinuities in other physical observables.

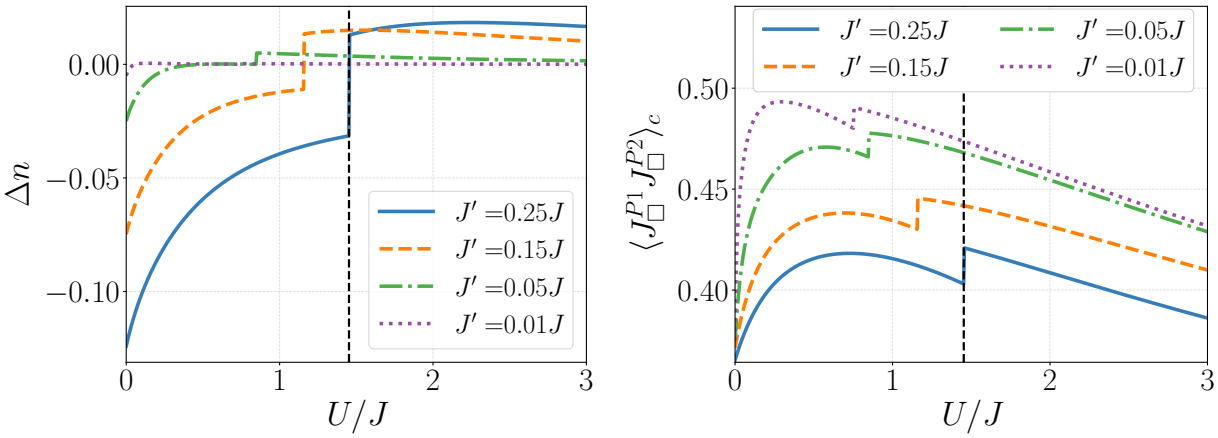

Figure 3.9: Relevant observables of the unperturbed model for four different values of $J' \in \{0.25J, 0.15J, 0.05J, 0.01J\}$ as a function U/J. The system consists of four bosons on eight sites forming two square plaquettes linked by inter-plaquette hopping strength J'. Left: density imbalance Δn. Right: Loop current connected correlator $\langle J_{\square}^{P1} J_{\square}^{P2} \rangle_c = \langle J_{\square}^{P1} J_{\square}^{P2} \rangle - \langle J_{\square}^{P1} \rangle \langle J_{\square}^{P2} \rangle$. Both panels show a black dashed vertical line at $U \simeq 1.452J$, where the ground state becomes degenerate for $J' = 0.25J$. This point closely coincides with the discontinuities of both density imbalance and loop current connected correlator lines for $J' = 0.25J$.

First, taking as reference the case $J' = 0.25J$, we can compare the response of the unperturbed system to what has been observed above for $\delta\phi \neq 0$. The trend of the density imbalance across the interaction range, shown in Fig. 3.9 (left) reveals a significant spatial reorganization of the bosons. At weak interactions, the bosons preferentially occupy the internal sites of the cluster (3, 4, 5, 6) to maximize the kinetic energy associated with inter-plaquette hopping. However, at the interaction threshold set by the closing of the first excitation gap, the density imbalance undergoes a sharp upward jump, signaling a spatial reorganization where the particles are redistributed toward the external sites (1, 2, 7, 8). This represents a fundamental change in the ground-state structure driven by the competition between U and the kinetic energy.
Simultaneously, the loop current connected correlator (right panel of Fig. 3.9) also exhibits a sudden jump at the point of crossing between ground state and the first excited state, as further signal of the observed peculiar behavior. The correlation stays positive in the whole studied interaction range, implying that while the mean current vanishes, the fluctuations of the currents in the two plaquettes are locked in phase. This reflects an underlying chiral order that confirms that the vortex nature of the system as an inherent feature of the many-body wavefunction.
The position of these discontinuities is sensitive to the inter-plaquette coupling J'. Weakening the inter-plaquette coupling shifts the discontinuity to lower interaction strengths and suppresses the size of the jumps. This dependence highlights that a finite inter-plaquette coupling is not merely a quantitative correction but a necessary condition for the emergence of this many-body behavior. It suggests that the non-trivial interplay between J and J' must be preserved to resolve the correct physics of the system, as the critical features of the spectrum are intrinsically tied to the finite hybridization between the two plaquettes. Consequently, the ability of a theoretical framework to capture these discontinuities likely depends on how J' is incorporated into the construction of effective Hamiltonians.

3.3 Construction of the low-energy effective theory

This section is oriented to detail the general procedure for the construction of low-energy theories of the system under consideration. We will later employ this scheme to derive different effective

descriptions, with different degrees of approximation and complexity.
To construct a low-energy effective model, we project the full many-body Hamiltonian onto a truncated, low-dimensional subspace. This approach allows us to isolate the relevant physics of the ground state and lowest excitations. The starting point is the general many-body Hamiltonian, partitioned into a single-particle (non-interacting) component H_0 and a quartic interaction term H_{int}, as in Eq. (3.2). First, we identify a reference single-particle operator H_{SP}, which may represent the full H_0 or a subset of it such as the intra-plaquette hopping, and solve its eigenvalue problem,

$$H_{\text{SP}}|\psi_\alpha\rangle = \varepsilon_\alpha|\psi_\alpha\rangle\,. \tag{3.19}$$

The eigenvectors $|\psi_\alpha\rangle$ define the single-particle orbitals of the system. We construct a transformation matrix $\mathcal{U}_{i\alpha} = \langle i|\psi_\alpha\rangle$, where the columns are the eigenvectors expressed in the site basis. This unitary matrix transforms the site operators into orbital operators as

$$b_i = \sum_\alpha \mathcal{U}_{i\alpha} c_\alpha\,. \tag{3.20}$$

The approximation to an effective theory lies in the truncation of this basis. We retain only a subset of m low-energy eigenstates $\{\psi_\alpha\}_{\alpha=1}^m$ to span the effective Hilbert space. This projection is well defined and physically meaningful provided that the single-particle spectrum exhibits a clear spectral gap Δ separating the m retained states from the discarded high-energy manifold. Once defined the low-energy subspace, any remaining quadratic terms in the Hamiltonian, such as hopping terms not included in the initial diagonalization of H_{SP}, are projected by simple matrix multiplication. If T represents the matrix form of these additional single-particle terms, the projected coefficients in the orbital basis are given by

$$\tilde{T}_{\alpha\beta} = \mathcal{U}^\dagger\, T\, \mathcal{U} = \sum_{ij} \mathcal{U}^*_{\alpha i}\, T_{ij}\, \mathcal{U}_{j\beta}, \tag{3.21}$$

where α, β are restricted to the indices of the low-energy subset: $\alpha, \beta = 1 \ldots m$.
The transformation of the quartic interaction H_{int} follows by substituting the operator expansion into the on-site interaction term. This mapping generates a multi-mode interaction where particles can scatter between any combination of the retained orbitals:

$$H_{\text{int}}^{\text{eff}} = \frac{U}{2} \sum_{\alpha,\beta,\gamma,\delta=1}^{m} V_{\alpha\beta\gamma\delta}\, c_\alpha^\dagger c_\beta^\dagger c_\gamma c_\delta\,. \tag{3.22}$$

The coupling tensor $V_{\alpha\beta\gamma\delta}$ encodes the spatial overlap of the chosen orbitals and is computed as

$$V_{\alpha\beta\gamma\delta} = \sum_{i=1}^{8} \mathcal{U}^*_{i\alpha} \mathcal{U}^*_{i\beta} \mathcal{U}_{i\gamma} \mathcal{U}_{i\delta}\,. \tag{3.23}$$

By construction, it is symmetric under exchange of the first pair of indices and of the second pair, $\alpha \leftrightarrow \beta\,,\quad \gamma \leftrightarrow \delta$. When the orbitals are real, so that $\mathcal{U}^*_{i\alpha}\mathcal{U}_{i\alpha}$, the tensor acquires full symmetry under permutation of any of its indices, and all exchanges $\alpha \leftrightarrow \beta \leftrightarrow \gamma \leftrightarrow \delta$ leave $V_{\alpha\beta\gamma\delta}$ invariant. When a given set of orbitals $c_\alpha^\dagger c_\beta^\dagger c_\gamma c_\delta$ is coupled by the interaction tensor $V_{\alpha\beta\gamma\delta}$, the symmetry of the tensor ensures that all permutations of the indices related by its invariances are coupled with the same strength. In other words, any interaction channel allowed for one ordering of (α, β, γ, δ) is automatically allowed for all symmetry-equivalent reorderings.
The effective Hamiltonian takes the final form

$$H_{\text{eff}} = \sum_{\alpha=1}^{m} \varepsilon_\alpha\, c_\alpha^\dagger c_\alpha + \sum_{\alpha,\beta=1}^{m} \tilde{T}_{\alpha,\beta} c_\alpha^\dagger c_\beta + \frac{U}{2} \sum_{\alpha,\beta,\gamma,\delta=1}^{m} V_{\alpha\beta\gamma\delta}\, c_\alpha^\dagger c_\beta^\dagger c_\gamma c_\delta\,, \tag{3.24}$$

The validity of this effective description is strictly confined to the regime where the on-site interaction and the kinetic perturbations energies are small compared to the spectral gap, $U, |T| \ll \Delta$. In this limit, the high-energy modes are left unpopulated and do not contribute (at the leading order) to the structure of the many-body ground state. Therefore, under these conditions, the theory provides a high-fidelity representation of the system's low-energy physics while drastically reducing the dimension of the underlying Fock space.

3.3.1 Chiral orbital order without higher bands

It is possible to show that the chiral orbital order of interacting bosons in π-flux square plaquettes can be interpreted in direct analogy with the physics of bosons occupying $p_{x,y}$ orbitals in higher bands as shown in [14]. In their work, Di Liberto and Goldman begin by analyzing the Hamiltonian of a single plaquette (which we denote by 1P),

$$H^{\mathrm{1P}}_{\mathrm{exact}} = -J\left(b_1^\dagger b_2 + b_2^\dagger b_4 + b_4^\dagger b_3 - b_3^\dagger b_1 + \mathrm{h.c.}\right) + \frac{U}{2}\sum_{i=1}^{4} n_i\left(n_i - 1\right). \tag{3.25}$$

An isolated plaquette has a low-energy subspace spanned by two degenerate single-particle modes, denoted as d_1 and d_2, which are separated by an energy gap $\propto J$ from higher excited states, as shown in Fig. 3.10.

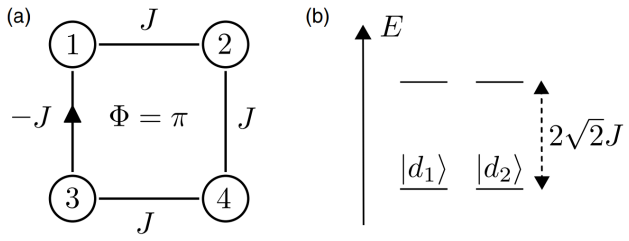

Figure 3.10: Single plaquette cluster. Left: graphical representation of the system, corresponding to the top plaquette in Fig. 3.2. Right: energy spectrum showing the same splitting of the isolated two-plaquettes case in Fig. 3.3. Source: (Adapted from [14]).

Projecting onto the lowest two-energy manifold simplifies the original four-site problem into a two-mode model, which can be written as follows:

$$H^{1P}_{\mathrm{eff}} = \frac{3U}{16}n^2 - \frac{U}{16}L_z^2 - \left(\sqrt{2}J + \frac{U}{8}\right)n\,, \tag{3.26}$$

where $n = d_1^\dagger d_1 + d_2^\dagger d_2$ and $_z = i(d_1^\dagger d_2 - d_2^\dagger d_1)$ are respectively the number and angular momentum operators.

We note that L_z is structurally identical to the angular momentum operator in $p_{x,y}$ orbital models [15]. The projected on-site interaction yields a term proportional to $-L_z^2$, alongside density-density interactions that depend on the total particle number n. Due to the negative sign of the $-L_z^2$ interaction term, the system energetically favors states that maximize the orbital angular momentum. Exact diagonalization confirms that the many-body ground state is doubly degenerate, corresponding to a total angular momentum of $\pm N$, where N is the total number of bosons. This leads to a macroscopic occupation of the complex orbitals $|d_1\rangle \pm i|d_2\rangle$. Consequently, the many-body ground state spontaneously breaks both time-reversal symmetry and a discrete $\mathbb{Z}_2$ orbital-exchange symmetry.

When these π-flux plaquettes are assembled into extended lattice geometries and coupled via weak hopping terms that preserve the orbital structure, the local orbital angular momentum ordering

translates into a chiral superfluid vortex lattice, as shown in Fig. 3.11. In this macroscopic phase, each supersite (plaquette) hosts a quantized vortex characterized by a condensate phase winding $\varphi_i = \arg\langle b_i \rangle$. The emergent vortex lattice can be seen as a direct many-body manifestation of the underlying orbital angular momentum maximization.

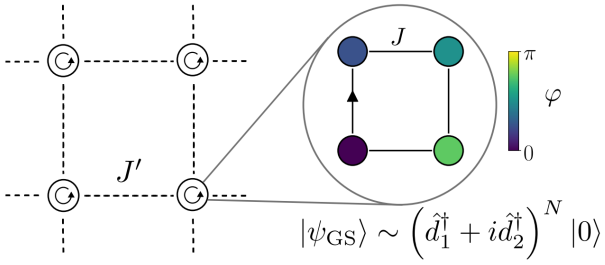

Figure 3.11: Sketch of the extension of the single-plaquette cluster to a two-dimensional BBH model. This construction in the weak inter-plaquette coupling limit ($J' \ll J$) results in a chiral superfluid phase. Such phase hosts one quantized vortex per plaquette, each characterized by a condensate phase winding $\varphi_i = \arg\langle b_i \rangle$. Source: (Adapted from [14]).

DMRG simulations show that this framework correctly captures the phase diagram, including transitions between chiral superfluid and chiral Mott insulator phases.

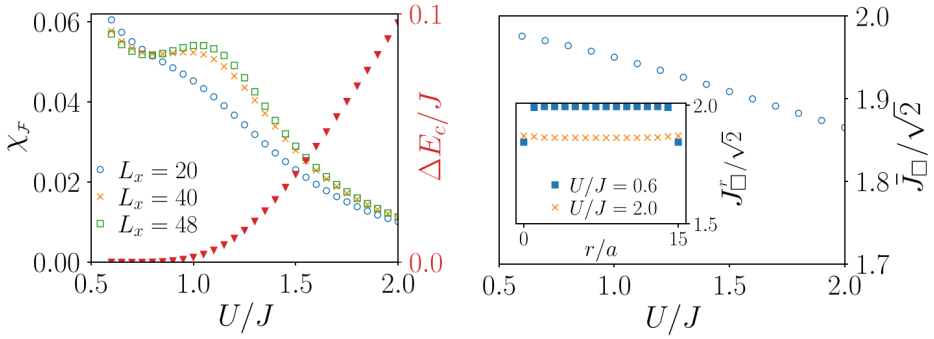

Figure 3.12: Chiral superfluid to chiral Mott insulator phase transition as a function of U/J. Left: fidelity susceptibility χ_f for a 2-leg ladder with length up to $L = 48$ sites, extracted with DMRG for $J' = 0.1J$ and an infinitesimal flux perturbation $\delta\phi$. The peak signals a phase transition. The trend of the finite charge gap ΔE_c, obtained by finite-size scaling, distinguishes between the two types of phase. ΔE_c is the energy required to change the total particle number of the system by one unit. Right Averaged loop-current $\bar{J}_\square = \sum_r |\langle J^r_\square \rangle|/(L-1)$ over the ladder plaquettes for $L = 32$. The inset displays two loop-current profiles, one in the chiral superfluid and one in the CMI. Source: (Adapted from [14]).

The transition between the chiral superfluid and the chiral Mott insulator is identified here by combining two complementary diagnostics. In Fig. 3.12, the fidelity susceptibility χ_f(left panel) exhibits a more pronounced peak as the system size is increased, signaling the presence of a phase transition. To determine the nature of the phases on either side of this peak, the charge gap $\Delta E_c = E(N+1) + E(N-1) - 2E(N)$, obtained via finite size scaling, is tracked as a function of the on-site interaction strength. A vanishing charge gap indicates a compressible phase, consistent with a superfluid, whereas the opening of a finite gap marks the onset of an incompressible Mott state. Throughout the transition, the loop-current pattern remains nonzero, demonstrating that time-reversal symmetry is broken in both phases. The spatial profile of these currents changes only mildly across the transition, reflecting the persistence of chiral order even as the system becomes insulating.

3.3.2 Single-plaquette effective theory for two interacting plaquettes

A natural extension of the single-plaquette effective description to the two-plaquette system involves treating the cluster as a pair of separable manifolds coupled perturbatively by inter-plaquette tunneling. In this "naive" extension, we assume that the low-energy physics is dominated by the local properties of each unit cell, with the J' links acting as weak hybridization between them. Formally, this construction follows the general procedure by defining the single-particle reference Hamiltonian as the intra-plaquette term, $H_{SP} = H_J$, and treating the inter-plaquette hopping as perturbation, $T = H_{J'}$.

As established in the single-particle spectrum (see Fig. 3.3), each isolated plaquette has a low-energy manifold of two degenerate states separated from the higher-energy sector by a gap of $2\sqrt{2}J$. Provided that $J', U \ll J$, we can truncate the total Hilbert space to the four-dimensional subspace spanned by the lowest two orbitals of each plaquette, namely:

$$d_\alpha^{P_1} = d_\alpha \otimes \mathbb{1}_{P_2}\,, \quad d_\alpha^{P_2} = \mathbb{1}_{P_1} \otimes d_\alpha\,. \tag{3.27}$$

Here, d_α are the single-particle orbitals of the previous subsection and the identities act on each plaquette's subspace, identified by sites $\mathrm{P}_1 : \{1, 2, 3, 4\}$ and $\mathrm{P}_2 : \{5, 6, 7, 8\}$ for the chosen enumeration (see Fig. 3.2). By projecting the full Hamiltonian 3.2 onto this basis, the single-plaquette effective theory is promoted to a two-plaquette model. The resulting effective Hamiltonian is

$$H^{2P}_{\text{eff}\,1P} = \frac{3U}{16}(n^2_{P_1}+n^2_{P_2}) - \frac{U}{16}\left(L^2_{P_1}+L^2_{P_2}\right) - \left(\sqrt{2}J+\frac{U}{8}\right)(n_{P_1}+n_{P_2}) - \frac{J'}{2\sqrt{2}}\left(d_1^{P_1\dagger}d_1^{P_2}+d_2^{P_1\dagger}d_2^{P_2}+\text{h.c.}\right), \tag{3.28}$$

where the local density n_{P_i} and orbital angular momentum L_{P_i} operators for each plaquette P_i are defined as:

$$\begin{aligned} n_{P_i} &= d_1^{P_i\dagger}d_1^{P_i} + d_2^{P_i\dagger}d_2^{P_i} \\ L_{P_i} &= \mathrm{i}\big(d_1^{P_i\dagger}d_2^{P_i} - d_2^{P_i\dagger}d_1^{P_i}\big) \end{aligned} \tag{3.29}$$

The final term in the effective model represents the projection of the J' hopping, which becomes a flavor-conserving tunneling between the same orbital types in adjacent plaquettes.

To better resolve the many-body spectrum and exploit the symmetry of the system, we perform a rotation to the chiral basis $|d_\pm^{P_i}\rangle = \frac{1}{\sqrt{2}}\big(|d_1^{P_i}\rangle \pm \mathrm{i}|d_2^{P_i}\rangle\big)$.

These states are simultaneous eigenstates of the isolated single-plaquette Hamiltonian H_J and the local angular momentum operator, $L_{P_i}|d_\pm^{P_i}\rangle = \pm|d_\pm^{P_i}\rangle$. In this rotated representation, the effective Hamiltonian takes the form

$$\begin{aligned} H^{2P}_{\text{eff}\,1P} =& \frac{U}{8}\sum_{i=1,\,2}\sum_{j=\pm} n_j^{P_i}\big(n_j^{P_i}-1\big) + \frac{U}{2}\big(n_-^{P_1}n_+^{P_1}+n_-^{P_2}n_+^{P_2}\big) - \sqrt{2}J\big(n_-^{P1}+n_+^{P_1}+n_-^{P_2}+n_+^{P_2}\big) + \\ &- \frac{J'}{2\sqrt{2}}\big(d_+^{P_1\dagger}d_+^{P_2}+d_-^{P_1\dagger}d_-^{P_2}+\text{h.c.}\big)\,, \quad \text{where } n_\pm^{P_i} = d_\pm^{P_i\dagger}d_\pm^{P_i}. \end{aligned} \tag{3.30}$$

This formulation explicitly reveals the competition between the underlying physical processes in the dimerized system. For a fixed total particle number N, the term proportional to J acts as a global energy shift and therefore does not influence the relative spectral structure. The first term, proportional to $U/8$, represents an on-orbital repulsive interaction. It penalizes the occupation of the same orbital by multiple bosons, tending to distribute the particles across the available modes. In contrast, the second term $(U/2)$ is the manifestation of the $-L_z^2$ interaction identified in the single-plaquette theory. By energetically penalizing the simultaneous occupation of opposite-chirality orbitals (+ and −) within a single plaquette, it drives the system to maximize its local orbital angular momentum. Finally, the projected inter-plaquette tunneling (J') couples orbitals

with the same chirality, mediating the delocalization of bosons across the two plaquettes. Notably, because this term is a chirality flavor-conserving coupling, the total orbital angular momentum is a conserved quantity:

$$L_{\text{tot}} = \left(n_+^{P_1} - n_-^{P_1}\right) + \left(n_+^{P_2} - n_-^{P_2}\right) . \tag{3.31}$$

Because the Hamiltonian now decomposes into sectors of definite total angular momentum, we can diagonalize the system within each sector independently. This provides an angular momentum-based distinction of the many-body spectrum.

3.3.3 Many-body spectrum in the isolated-plaquettes effective theory

Following the analysis of the exact model, we focus on the case $N = 4$, which corresponds to an average filling of half a boson per site. The many-body Hilbert space $\mathcal{H}$ of dimension $D = 35$ ($N = 4$ bosons in 4 orbitals) decomposes into a direct sum of subspaces $\mathcal{H} = \bigoplus_k \mathcal{H}_{L_k}$. To explicitly construct and block-diagonalize the Hamiltonian within each subspace $\mathcal{H}_{L_k}$, we define the many-body Fock basis in terms of the chiral orbital occupations: $|n_+^{P_1}, n_-^{P_1}, n_+^{P_2}, n_-^{P_2}\rangle$. The total number of particles dictates that $\sum_{i,\sigma} n_\sigma^{P_i} = 4$.
For $N = 4$, there are five distinct sub-sectors characterized by $L_{\text{tot}} \in \{-4, -2, 0, 2, 4\}$. The system exhibits a manifest symmetry under the simultaneous exchange of the occupation of the $+$ and $-$ orbitals in both plaquettes. This parity-like operation maps the basis states of a $+L_{\text{tot}}$ sector directly onto those of the corresponding $-L_{\text{tot}}$ sector, leaving the matrix representation of the Hamiltonian unchanged. Consequently, the energy spectrum is strictly doubly degenerate for all states with $L_{\text{tot}} \neq 0$. The specific dimensional breakdown of the effective Hamiltonian is as follows:

- $L_{\text{tot}} = \pm 4$ sectors, with dimension $D_{L_z=\pm 4} = 5$. The basis states for the $L_{\text{tot}} = +4$ sector are:
  $B_{L_z=4} = \{\, |4000\rangle, |3010\rangle, |2020\rangle, |1030\rangle, |0040\rangle \,\}$. These are the maximally chiral states.
- $L_{\text{tot}} = \pm 2$ sectors, with dimension $D_{L_z=\pm 2} = 8$. The basis states for $L_{\text{tot}} = +2$ are:
  $B_{L_z=2} = \{\, |3100\rangle, |3001\rangle, |2110\rangle, |2011\rangle, |1120\rangle, |1021\rangle, |0130\rangle, |0031\rangle \,\}$. These sectors represent intermediate angular momentum, where bosons stay in orbitals with opposite chirality with unbalanced occupations.
- $L_{\text{tot}} = 0$ sector, with dimension $D_{L_z=0} = 9$. This is the unique, non-degenerate sector where the chirality is perfectly balanced out. Its basis states are:
  $B_{L_z=0} = \{\, |2200\rangle, |1210\rangle, |0220\rangle, |2101\rangle, |1111\rangle, |0121\rangle, |2002\rangle, |1012\rangle, |0022\rangle \,\}$.

For each sector at fixed $L_z = k$, the matrix form of the corresponding Hamiltonian block is constructed element-wise as

$$\langle i|H_{\text{eff}\,1P}^{2P}|j\rangle \quad \forall |i\rangle, |j\rangle = |n_+^{P_1}, n_-^{P_1}, n_+^{P_2}, n_-^{P_2}\rangle \in B_{L_z=k} \, .$$

By independently diagonalizing these matrices, we can construct the low-energy many-body spectrum within this particular effective description. The resulting spectrum, plotted as a function of the on-site interaction strength U/J, for fixed $J' = 0.25J$, is shown in Fig. 3.13, with colors highlighting the distinct L_{tot} values. This method allows to easily obtain all 35 eigenstates of the effective theory. We plot the first 12 lines (corresponding to the lowest 21 eigenvalues in the weak interacting limit) because we are interested in the low-energy properties, and the comparison with the exact diagonalization. Lines are tracked by maximum fidelity overlap as explained in subsection 3.2.3. Because tracking eigenstates does not guarantee that the selected manifold remains the lowest in energy at all parameter values, we verified this explicitly by plotting the full spectrum

and confirming that no higher-energy state at $U = 0$ enters the displayed low-energy window at larger values of U/J.

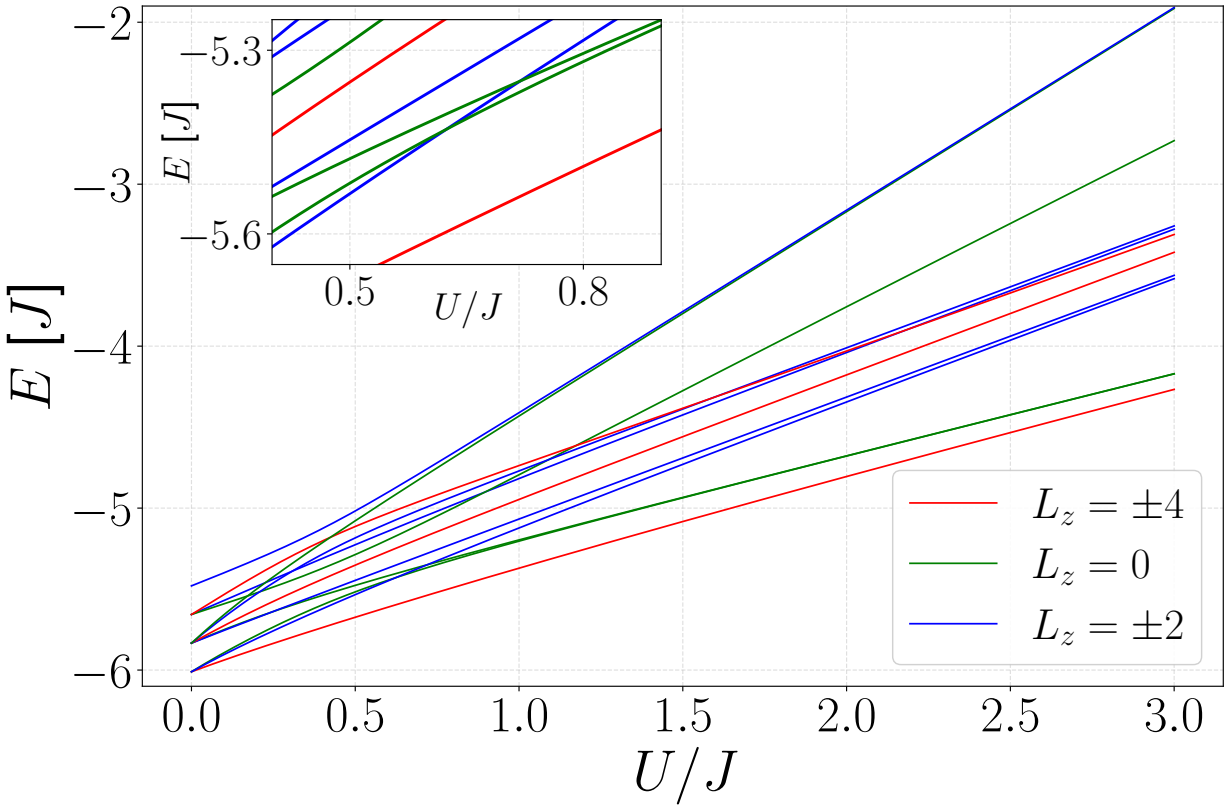

Figure 3.13: Spectrum of the effective Hamiltonian $H^{2P}_{\text{eff }1P}$ as a function of U/J. Colors identify total angular momentum of the two plaquettes: doubly-degenerate states with $L_z = \pm 4$ are red, states with $L_z = \pm 2$ ($deg = 2$) are blue, while non-degenerate eigenstates with $L_z = 0$ are green. The ground-state maximizes total angular momentum like in the single-plaquette effective description.

Applying the naive effective theory to the two-plaquette system allows us to observe the emergence of a structured many-body spectrum, though with significant qualitative differences compared to the exact results of Fig. 3.6. The spectrum of the effective Hamiltonian $H^{2P}_{\text{eff }1P}$ is characterized by states grouped into distinct sectors based on their total angular momentum, L_z. Consistent with the single-plaquette effective description, the ground state in this construction maximizes the total angular momentum $L_z = \pm 4$, as shown by the red doubly-degenerate ground state line in Fig. 3.13. This links chiral order to angular momentum physics also in the two-plaquette extension of the single-plaquette description.

While the naive effective theory captures the general hierarchy of the many-body states, specifically the existence of a well-separated low-energy manifold, it fails to reproduce several critical features of the exact system. In the naive theory, the first energy splitting $(E_2 - E_1)$ is identically zero by construction because the inter-plaquette coupling is treated in a way that preserves the perfect degeneracy between the $+$ and $-$ chirality sectors. In contrast, the exact spectrum reveals a non-trivial splitting that varies with U/J and crosses zero at an intermediate value of the interaction strength.

The exact spectrum features an avoided crossing between higher excited states. Instead, as shown by the inset in Fig. 3.13, in the naive spectrum these features are replaced by exact crossings of levels belonging to different L_z sectors.

Although both models show a gap separating the lowest two states from the rest of the spectrum,

the precise ordering and spacing of the higher levels in the naive theory do not align well with the exact results.

3.3.4 Properties of the many-body ground state in the isolated-plaquettes effective theory

We study the relevant observables of the model identified in Subsection 3.2.2 in the context of the isolated-plaquettes effective theory to compare the behavior of the system as the interaction strength U/J varies to the exact results of Subsection 3.2.4. Within the effective theory of this subsection, the inter-plaquette coupling is projected onto the single plaquette orbitals, therefore the J' link is not to be considered as a current carrier and thus we omit to display here the vorticity, border and internal currents behavior. In the following, we focus on the trend of the loop current.

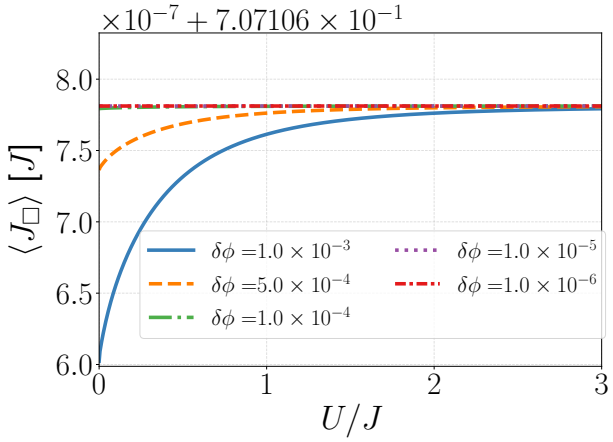

Figure 3.14: Loop current $J_\square = \langle J_\square^{P1} \rangle = \langle J_\square^{P2} \rangle$ versus U/J in the isolated-plaquettes effective model perturbed by different values of the symmetry-breaking flux shift $\delta\phi \in \{10^{-3}, 2 \cdot 10^{-4}, 10^{-4}, 10^{-5}\, 10^{-6}\}$. The system consists of four bosons on eight sites forming two square plaquettes linked by inter-plaquette hopping strength $J' = 0.25J$.

In contrast to the exact numerical results, the loop current response within the naive effective theory shows no signs of a revival. As illustrated in Fig. 3.14, the currents are essentially fixed at a value of approximately $0.707J$ and remain constant across the entire investigated range of U/J. This lack of non-monotonic behavior is a direct consequence of the ground-state manifold being perfectly degenerate ($E_2 - E_1 = 0$) by construction in this framework. Given that we do not fix the total angular momentum sector, the two $L_z = \pm 4$ chiral ground states are always energetically equivalent for $\delta\phi = 0$. In Fig.3.14, the system maintains a maximal, nonzero current expectation value set by the infinitesimal flux shift $\delta\phi \to 0$. While this captures the existence of chiral states, the "frozen" nature of the naive orbitals prevents the theory from describing the physical competition between interaction and hybridization that drives the current enhancement and site-redistribution observed in the exact model (see Fig.3.8, right).

To conclude our analysis of the naive effective theory, we examine the density imbalance and the current-current correlations. These observables further highlight the qualitative discrepancies between the single-plaquette approximation and the exact physics of the dimerized system.

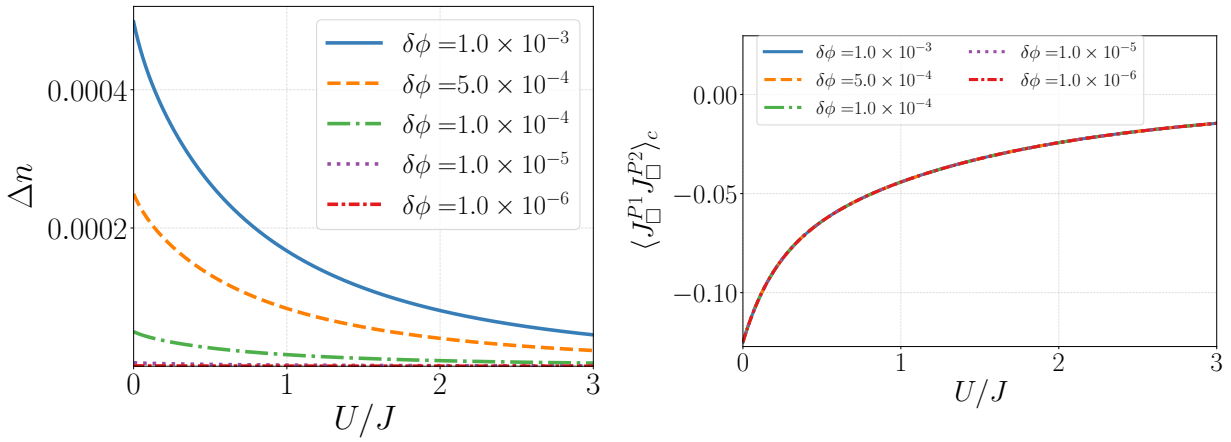

Figure 3.15: Relevant observables of the unperturbed isolated-plaquettes effective model for different values of the flux shift $\delta\phi \in \{10^{-3}, 2 \cdot 10^{-4}, 10^{-4}, 10^{-5}\, 10^{-6}\}$. The system consists of four bosons on eight sites forming two square plaquettes linked by inter-plaquette hopping strength J'. Left: density imbalance Δn. Right: Loop current connected correlator $\langle J_\square^{P1} J_\square^{P2} \rangle_c = \langle J_\square^{P1} J_\square^{P2} \rangle - \langle J_\square^{P1} \rangle \langle J_\square^{P2} \rangle$.

Unlike the exact model, which exhibited a sharp spatial reorganization of particles at the level-crossing point, the density imbalance in the naive theory remains essentially zero. As shown in Fig. 3.15 (left), the values of Δn are several orders of magnitude smaller than those found in the exact case. In the limit of a vanishing flux shift ($\delta\phi \to 0$), the imbalance vanishes entirely across the whole range of U/J. The theory is fundamentally unable to capture the switch from internal to external site preference that characterizes the true ground state.

The failure of the naive construction is perhaps most evident in the behavior of the loop current connected correlator, Fig. 3.15 (right). While the exact model showed strong positive correlations, signaling that the two plaquettes lock into the same chirality, the naive theory predicts persistent negative correlations. Regardless of how small the symmetry-breaking flux shift is, the correlator remains negative and only slowly approaches zero as the interaction strength increases, while showing no sign of jumps or non-monotonic behavior. While the chirality is reflected in the fact that both plaquettes present the same loop current pattern, with equal magnitude and direction, this description fails to capture the correlated nature of vortex order, which becomes long-range in extended lattices.

It is important to note that these results are presented in the limit of an infinitesimal flux shift $\delta\phi$ to ensure numerical stability. However, even with this stabilization, the resulting physics is qualitatively inconsistent with the full theory. In summary, the naive single-plaquette effective theory fails on every critical benchmark: it does not reproduce the ground-state level crossing, it misses the current revival, it cannot describe the spatial redistribution of particles, and it predicts the wrong sign for chiral correlations. These failures demonstrate that inter-plaquette coupling J' cannot be treated as a mere perturbation on top of isolated plaquette states. Instead, a more sophisticated approach is required, one that accounts for the inter-plaquette mixing of the orbitals.

3.3.5 Mirror-symmetry adapted construction

To conclude our discussion of the naive effective approach, we introduce a symmetry-adapted version of the theory. Although this formulation does not alter the underlying physical predictions of the isolated-plaquettes framework, it establishes a mathematical correspondence with the more advanced effective theory presented in the following section. In that theory, the single-particle orbitals are defined as simultaneous eigenstates of the full single-particle Hamiltonian $H_0(r)$ (Eq. (3.5)) and of the M_x symmetry (Eq. (3.11)). To ensure consistency between the two descriptions,

we likewise require simultaneous diagonalization of the reference single-particle Hamiltonian and the mirror operator.

We take as reference Hamiltonian the unperturbed intra-plaquette term, $H_{SP} = H_J$. The only difference from the previous subsection is that we now construct the common eigenstates of H_J and M_x. This is allowed because the two operators commute. This construction leads to a unitary mixing of the plaquette-localized orbitals $d_\alpha^{P_1}$ and $d_\alpha^{P_2}$ (Eq. (3.27)), while preserving the naive assumption that the orbitals themselves do not depend on r. The corresponding single-particle transformation matrix $\mathcal{U}_{i\alpha}$ (Eq. (3.20)), with $i \in \{1,\dots,8\}$ and $\alpha \in \{1,\dots,4\}$, is

$$\mathcal{U}_{i\alpha} = \begin{pmatrix} A & -B & A & -B \\ A & B & A & B \\ -B & A & -B & A \\ B & A & B & A \\ A & -B & -A & B \\ A & B & -A & -B \\ -B & A & B & -A \\ B & A & -B & -A \end{pmatrix},$$

where $A = \frac{1}{2}\sqrt{\frac{1}{2}\left(1+\frac{1}{\sqrt{2}}\right)}$ and $B = \frac{1}{2}\sqrt{\frac{1}{2}\left(1-\frac{1}{\sqrt{2}}\right)}$.

In this basis, the single-particle energies $\varepsilon_\alpha^{\mathrm{O(r)}}$ incorporate the first-order correction in $r = J'/J$

$$\begin{aligned} \varepsilon_1^{O(r)} = \varepsilon_2^{O(r)} &= -J\left(\sqrt{2} + \frac{r}{2\sqrt{2}}\right) \equiv \varepsilon_L^{O(r)}, \\ \varepsilon_3^{O(r)} = \varepsilon_4^{O(r)} &= -J\left(\sqrt{2} - r/2\sqrt{2}\right) \equiv \varepsilon_H^{O(r)}. \end{aligned} \tag{3.32}$$

Each orbital is labeled by its energy eigenvalue and mirror symmetry eigenvalue $(\varepsilon^{O(r)}, m_x)$:

$$\begin{aligned} |1\rangle = (\varepsilon_L^{O(r)}, -1), \quad |2\rangle = (\varepsilon_L^{O(r)}, +1) \\ |3\rangle = (\varepsilon_H^{O(r)}, -1), \quad |4\rangle = (\varepsilon_H^{O(r)}, +1) \end{aligned}$$

The columns of $U_{i\alpha}^{O(r)}$ correspond to the orbitals $\big(|1\rangle, |2\rangle, |3\rangle, |4\rangle\big)$ in this order, expressed in site basis.

The projection of the on-site interaction H_{int} onto this basis defines the coupling tensor $V'_{\alpha\beta\gamma\delta}$. Because the orbitals are delocalized over both plaquettes, the interaction produces a variety of multi-mode scattering processes. The nonvanishing components of $V'_{\alpha\beta\gamma\delta}$, grouped by coupling type, are listed in Table 3.2. We distinguish four different channel types: self interaction, where $\alpha = \beta = \gamma = \delta$; intra-eigenvalue scattering, where all indeces refer to orbitals with the same specified single-particle eigenvalue; cross-eigenvalue scattering, where the indeces involve orbitals with different specified single-particle eigenvalues; and four-orbital mixing, where $(\alpha, \beta, \gamma, \delta)$ are all distinct, coupling four different orbitals.

Self-interaction corresponds to on-orbital repulsion. Intra-m_x scattering includes density-density and exchange processes of orbitals processes between orbitals sharing the same mirror eigenvalue. Cross-m_x scattering involve density-density and exchange terms for orbitals with opposite mirror eigenvalue. The four-orbital mixing term transfers a pair of excitations from two distinct orbitals into the remaining two.

The resulting "naive" effective Hamiltonian in the symmetry-adapted basis contains no off-diagonal quadratic terms:

$$H_{\mathrm{eff}\,1P}^{2P} = \sum_{\alpha=1}^{4} \varepsilon_\alpha^{O(r)}\, c_\alpha^\dagger c_\alpha + \frac{U}{2} \sum_{\alpha,\beta,\gamma,\delta=1}^{4} V'_{\alpha\beta\gamma\delta}\, c_\alpha^\dagger c_\beta^\dagger c_\gamma c_\delta\,. \tag{3.33}$$

Table 3.1: nonzero elements of the projected interaction tensor $V'_{\alpha\beta\gamma\delta}$ in the symmetry-adapted basis. Only unique permutations of indices $(\alpha, \beta, \gamma, \delta)$ are listed; all other index exchanges yield the same coupling strength.

Coupling Type	**Index Combinations** $(\alpha, \beta, \gamma, \delta)$	**Weight**
Self-interaction	$(1,1,1,1), (2,2,2,2), (3,3,3,3), (4,4,4,4)$	3/16
Intra-m_x	$(1,1,3,3), (2,2,4,4)$	3/16
Cross-m_x	$(1,1,2,2), (1,1,4,4), (2,2,3,3), (3,3,4,4)$	1/16
Four-orbital mixing	$(1,2,3,4)$	1/16

Further remarks on this formulation, and its relation to the advanced effective theory, are presented in the next section.

3.4 Two-plaquette effective theory

To capture the full hybridization of the dimerized system, we employ an advanced effective theory where the single-particle reference Hamiltonian is the full non-interacting Hamiltonian, $H_{\text{SP}} = H_0$. In contrast to the naive approach, the single-particle orbitals $\{\psi_\alpha(r)\}$ now depend explicitly on the coupling ratio $r = J'/J$, allowing the basis to adjust continuously to the inter-plaquette tunneling.

3.4.1 Mirror symmetry adapted construction

To uniquely define low-energy orbitals, we perform a simultaneous diagonalization of H_0 and the mirror symmetry operator M_x. The diagonalization is fully symbolic in the parameter r, allowing us to retain the exact dependence of single-particle orbitals on the inter-plaquette coupling. The explicit form is obtained using Wolfram Mathematica software [76].
As seen in Eq. (3.4), the low-energy manifold consists of two degenerate pairs. The mirror eigenvalue provides a natural label that distinguishes the states within each pair. We therefore label each orbital by its energy eigenvalue and mirror eigenvalue $(\varepsilon,\, m_x)$:

$$|1\rangle = (\varepsilon_L,\, -1), \quad |2\rangle = (\varepsilon_L,\, +1)$$

$$|3\rangle = (\varepsilon_H,\, -1), \quad |4\rangle = (\varepsilon_H,\, +1)$$

The explicit form of the transformation matrix $\mathcal{U}_{i\alpha}$ is not shown, as its analytic expression is lengthy and not required for the discussion that follows.
In this basis, the projected interaction tensor $V_{\alpha\beta\gamma\delta}$ contains 128 nonvanishing entries. Because the chosen orbitals are real, the tensor is fully symmetric under the exchange of any pair of indices $\alpha \leftrightarrow \beta \leftrightarrow \gamma \leftrightarrow \delta$, reducing the number of independent coupling channels to 21. The interaction strengths are no longer constant but vary with the inter-plaquette coupling. Table 3.2 lists these coefficients, Taylor-expanded for $r \to 0$ up to $O(r^3)$, providing a systematic view of how dimerization modifies the many-body scattering channels. The full analytic expressions were obtained and used in the calculations presented in this section, but they are not reported here: their symbolic form is lengthy and offers little additional insight.

As discussed in Subsection 3.3.5, self-interactions terms correspond to on-orbital repulsions. In the present formulation, their coefficients distinguish low-energy and high-energy modes. Channels involving two pairs of equal indices represent density-density and exchange processes acting on the specific orbitals indicated by the coupling type.

Table 3.2: nonzero elements of the projected interaction tensor $V_{\alpha\beta\gamma\delta}$ in the symmetry-adapted basis. Only one representative for each symmetry-related permutation of $(\alpha, \beta, \gamma, \delta)$ is listed.

Coupling Type	**Index Combinations** $(\alpha, \beta, \gamma, \delta)$	**Weight**
Low-energy self-int.	$(1,1,1,1), (2,2,2,2)$	$\frac{3}{16} - \frac{r}{32} + \frac{3r^2}{64} - \frac{r^3}{256}$
High-energy self-int.	$(3,3,3,3), (4,4,4,4)$	$\frac{3}{16} + \frac{r}{32} + \frac{3r^2}{64} + \frac{r^3}{256}$
Intra-m_x	$(1,1,3,3), (2,2,4,4)$	$\frac{3}{16} - \frac{7r^2}{128}$
Intra-ε_L (cross-m_x)	$(1,1,2,2)$	$\frac{1}{16} + \frac{r}{32} + \frac{r^2}{64} + \frac{r^3}{256}$
Intra-ε_H (cross-m_x)	$(3,3,4,4)$	$\frac{1}{16} - \frac{r}{32} + \frac{r^2}{64} - \frac{r^3}{256}$
Cross-energy cross-m_x	$(1,1,4,4), (2,2,3,3)$	$\frac{1}{16} - \frac{r^2}{128}$
Four-orbital mixing	$(1,2,3,4)$	$\frac{1}{16} - \frac{r^2}{128}$
$3\varepsilon_H \to 1\varepsilon_L$ **intra-$m_x = -1$**	$(1,3,3,3)$	$\frac{r}{8\sqrt{2}} + \frac{r^2}{64\sqrt{2}} - \frac{9r^3}{256\sqrt{2}}$
$3\varepsilon_H \to 1\varepsilon_L$ **intra-$m_x = +1$**	$(2,4,4,4)$	$-\frac{r}{8\sqrt{2}} - \frac{r^2}{64\sqrt{2}} + \frac{9r^3}{256\sqrt{2}}$
$3\varepsilon_L \to 1\varepsilon_H$ **intra-$m_x = -1$**	$(1,1,1,3)$	$-\frac{r}{8\sqrt{2}} + \frac{r^2}{64\sqrt{2}} + \frac{9r^3}{256\sqrt{2}}$
$3\varepsilon_L \to 1\varepsilon_H$ **intra-$m_x = +1$**	$(2,2,2,4)$	$\frac{r}{8\sqrt{2}} - \frac{r^2}{64\sqrt{2}} - \frac{9r^3}{256\sqrt{2}}$
asymmetric mixing	$(1,1,2,4), (1,2,2,3), (1,3,4,4), (2,3,3,4)$	$\pm\frac{r^2}{64\sqrt{2}} \pm \frac{r^3}{256\sqrt{2}}$

The resulting two-plaquette effective Hamiltonian within this mirror symmetry-adapted basis is

$$H_{\text{eff}}^{2P} = \sum_{\alpha=1}^{4} \varepsilon_\alpha \, c_\alpha^\dagger c_\alpha + \frac{U}{2} \sum_{\alpha,\beta,\gamma,\delta=1}^{4} V_{\alpha\beta\gamma\delta} \, c_\alpha^\dagger c_\beta^\dagger c_\gamma c_\delta \, . \tag{3.34}$$

3.4.2 Comparison to isolated-plaquettes mirror-adapted effective theory

The transition from the naive effective theory to the advanced construction reveals the physical consequences of allowing orbital hybridization. In the limit $r \to 0$, the two symmetry-adapted theories coincide exactly: the $O(1)$ terms of the advanced interaction tensor recover the 3/16 and 1/16 weights found in Table 3.1. However, for finite r, two critical differences emerge that distinguish the advanced effective theory.

Renormalization of existing couplings

The self-interaction, intra-eigenvalue, cross-eigenvalue, and four-orbital mixing terms (the 3/16 and 1/16 sectors) acquire r-dependent corrections. This reflects the fact that the repulsive energy between bosons is modified by the dimerization. This is a direct consequence of the fact that the

spatial profiles of the single-particle orbitals evolve with the inter-plaquette tunneling. Different orbitals evolve differently with increasing r. For instance, for the lowest orbitals $|1\rangle$, $|2\rangle$ the self interaction coefficient decreases with r, whereas for the higher orbitals $|3\rangle$, $|4\rangle$ it increases. The self interaction in a orbital $|\alpha\rangle$ is proportional to $V_{\alpha\alpha\alpha\alpha} \simeq \sum_i |\langle i|\alpha\rangle|^4$, where $\langle i|\alpha\rangle$ is the orbital amplitude on site i. As r increases the lower and higher orbitals redistribute their weight across the eight sites in different ways, leading to opposite trends in $V_{\alpha\alpha\alpha\alpha}$. A more evenly-distributed, delocalized orbital leads to a weaker on-orbital interaction term and vise versa.

Emergence of new scattering channels

More importantly, the advanced theory identifies entirely new interaction channels that are strictly absent in the naive theory. These are the $3\varepsilon_{H(L)} \to \varepsilon_{L(H)}$ intra-m_x and asymmetric mixing terms in Table 3.2, which vanish at $r = 0$. Physically, these terms represent density-induced tunneling and interaction-induced orbital-mixing processes. Because some of these channels scale as $O(r)$, they become increasingly relevant as the inter-plaquette coupling grows, potentially altering the many-body ground state and the chiral current response in ways the naive theory cannot predict.

3.4.3 Many-body spectrum in the two-plaquette effective theory

To assess the validity of the advanced effective theory, we now compare its many-body spectrum with the exact results and with the naive construction. For a fixed total particle number $N = 4$, the advanced theory yields an interacting Hamiltonian with Hilbert space dimension $D = 35$ ($N = 4$ bosons in four inter-plaquette coupling-dependent orbitals). This dimension makes the problem more computationally accessible to diagonalize than the exact Hamiltonian while still incorporating both orbital hybridization and a more complete interaction structure as opposed to the naive theory. By tracking the evolution of its eigenvalues as a function of U/J, we can directly evaluate how well the effective description reproduces the ordering, splittings, and avoided crossings observed in the exact spectrum.

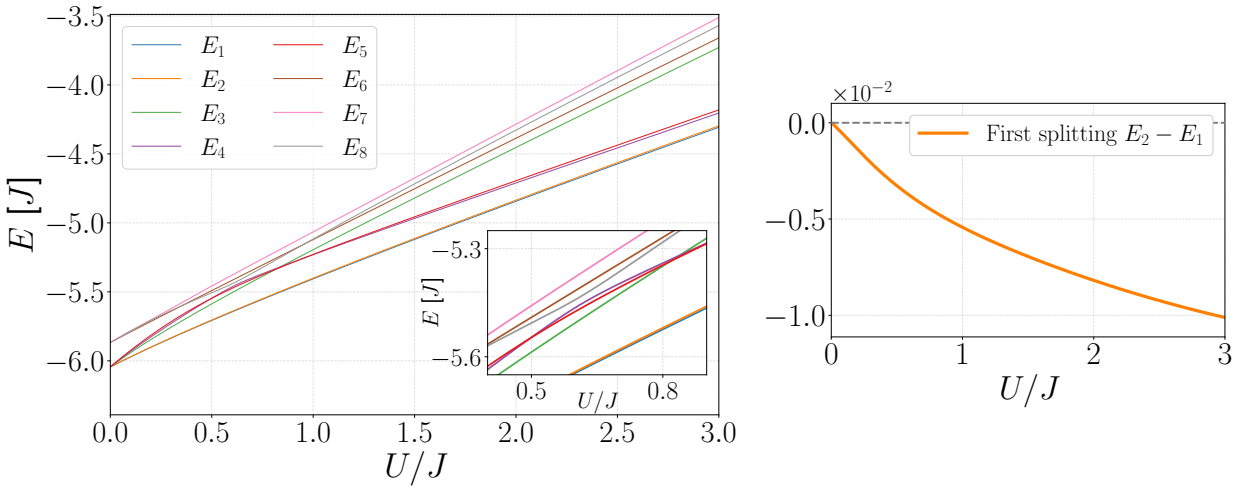

Figure 3.16: Many-body spectrum of the two-plaquette effective BBH model for $J' = 0.25J$ at half filling. Left: lowest eight energy levels as a function of interaction strength U/J. The inset displays a zoom of the region $U/J \in [0.4, 0.9]$ highlighting an avoided crossing between the fifth and sixth excited states. Right: energy splitting between the ground state and first excited state as a function of U/J.

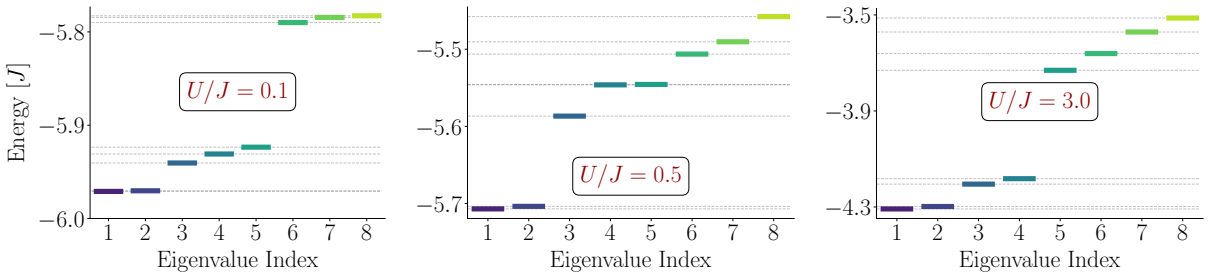

Figure 3.17: Many-body spectrum of the effective two-plaquette BBH model. Lowest eight energy levels for $J' = 025J$ at fixed values of U/J: 0.1 (left), 0.5 (center), and 3.0 (right). These panels correspond to vertical cuts through the full spectrum shown in Fig. 3.6 and highlight level splittings that are difficult to resolve in the main plot.

The transition to the advanced effective theory marks a significant quantitative and qualitative improvement, as this framework successfully recovers the critical many-body features that were absent in the naive approximation. The overall many-body spectrum of the advanced theory shows excellent agreement with the exact results . The low-energy manifold remains well-separated from the higher excited states, and the specific ordering and evolution of the levels E_3 through E_8 are closely reproduced . A significant result is the ability of the theory to capture the internal dynamics of the high-energy sector. As shown in the inset of Fig. 3.16 (left), the advanced effective model successfully reproduces the avoided crossing between higher-energy eigenstates for U/J between 0.5 and 0.8 . Another important improvement lies in the description of the low-energy doublet splitting, 3.16 (left). This effective theory recovers a nonzero splitting that evolves non-trivially as a function of U/J. However, within this restricted range, we do not observe the ground state level crossing. As a consequence, within the window $U/J \in [0, 3]$ and for the chosen $J' = 0.25J$, there is no non-monotonic behavior of the currents. Nonetheless, even in this parameter regime, the advanced effective theory regains key physical insights beyond the isolated-plaquettes approach, visible in the relevant observables of the unperturbed model ($\delta\phi = 0$).

3.4.4 Properties of the many-body ground state in the two-plaquette effective theory

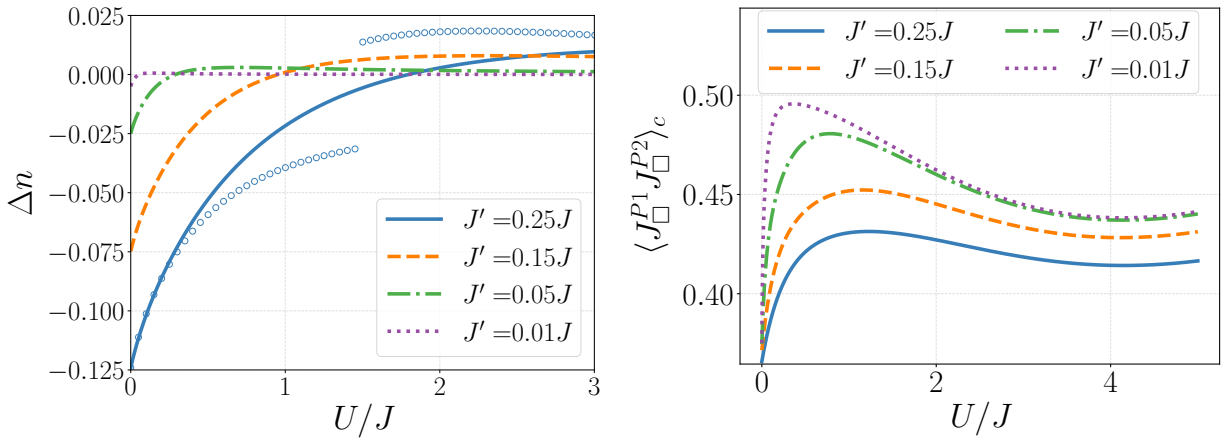

Figure 3.18: Relevant observables of the unperturbed advanced effective model for four different values of $J' \in \{0.25J, 0.15J, 0.05J, 0.01J\}$ as a function of U/J. The system consists of four bosons on eight sites forming two square plaquettes linked by an inter-plaquette hopping strength J'. For the $J' = 0.25J$ case, results from the exact theory are included as blue open markers to allow for a direct comparison with the blue solid line, which represents the effective theory results at the same coupling strength. Left: density imbalance Δn. Right: Loop current connected correlator $\langle J_\square^{P1} J_\square^{P2}\rangle_c = \langle J_\square^{P1} J_\square^{P2}\rangle - \langle J_\square^{P1}\rangle\langle J_\square^{P2}\rangle$.

The advanced theory recovers a nonvanishing density imbalance Δn. Unlike the naive model, the coupled-plaquette framework captures a continuous spatial reorganization of the bosons as the interaction strength increases, as shown in Fig. 3.18 (left). For example, for $J' = 0.25J$ (blue line) the imbalance starts at negative values (internal site preference) and crosses zero around $U/J \approx 1.8$, shifting toward positive values (external site preference). Although the exact results for the same inter-plaquette coupling strength (blue open markers in Fig. 3.18) display the sign reversal for a slightly lower value of $U/J \simeq 1.45$, accompanied by a sharp jump, the trend obtained with the effective theory resembles the physical mechanism observed in the exact results, where the system shifts its density to minimize the energetic cost of particle overlap.

The advanced theory also resolves the sign error present in the naive model's current-current correlations. Fig. 3.18 (right) illustrates that the loop current connected correlators are now strictly positive and possess the correct physical magnitude, ranging between 0.4 and 0.5 . This indicates that the theory correctly identifies the tendency of the two plaquettes to lock into a collective chiral state. Although the correlator displays a non-monotonic evolution, it does not exhibit the sharp jump seen in the exact model.

The absence of a sharp discontinuity in these observables is directly tied to the behavior of the low-energy manifold. In this parameter regime, the first energy splitting $E_2 - E_1$ remains finite (Fig. 3.16, right), without turning back to cross zero. Because the current revival and other "jump" phenomena are macroscopic signatures of the ground-state crossing, they do not appear as interesting features in this restricted window and are therefore omitted from this initial comparison.

To fully recover the level-crossing physics and the associated current revivals, we must extend our analysis to higher interaction strengths U and larger inter-plaquette couplings J'. At first glance, simultaneously enlarging both parameters might appear to violate the fundamental assumptions of our effective theory. The construction relies on a strict separation of scales: the on-site interaction U is treated as a perturbation and projected exclusively onto the low-energy orbitals, implicitly assuming that U remains small enough to safely discard interaction terms that mix the retained states with the high-energy chiral counterparts. While J' is incorporated non-perturbatively, mean-

ing we can increase it without breaking the hybridization model, enlarging U risks breaking the perturbative projection itself.
However, a careful examination of the single-particle spectrum as a function of the coupling ratio $r = J'/J$ provides a physical justification for this extended parameter regime.

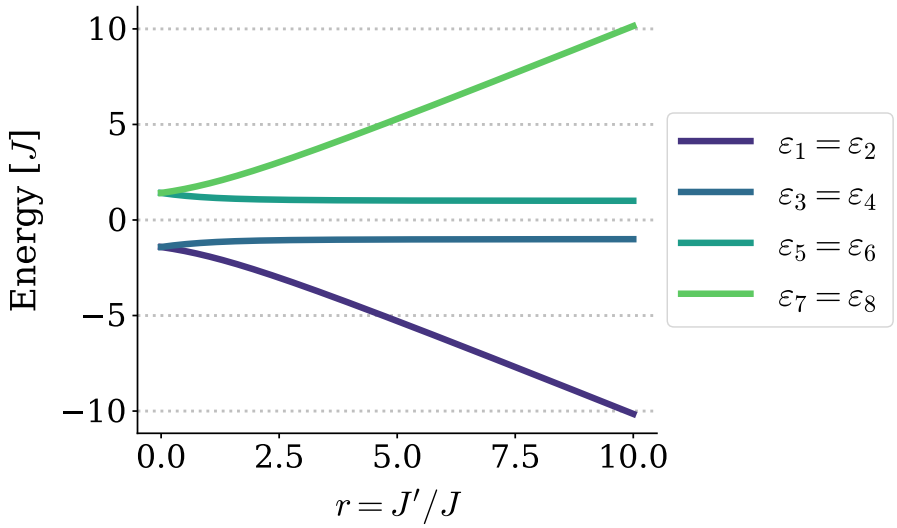

Figure 3.19: Single-particle spectrum of H_0 (Eq. (3.5)) as a function of the adimensional inter-plaquette coupling $r = J'/J$, extended up to $r = 10$.

As illustrated in Fig. 3.19, the fundamental gap between the retained negative-energy states and the discarded positive-energy states remains on the order of J. However, as J' increases, the negative-energy sector itself undergoes a significant bifurcation: the lowest-energy doublet $(\varepsilon_1, \varepsilon_2)$ descends linearly with J', while the upper negative-energy doublet $(\varepsilon_3, \varepsilon_4)$ remains relatively flat. This behavior allows us to identify an emergent separation of energy scales proportional to J'. Under these conditions, we can assume that the many-body ground state is primarily determined by the properties of the lowest-energy doublet. By energetically isolating these two orbitals, the interaction strength $\simeq U/16$ can be meaningfully compared to the J'-dependent gap rather than just the base hopping J (where the $1/16$ factor comes from the coupling weight $\leq 3/16$ that multiplies the interaction strength when projected). In this hierarchy, the upper negative-energy states $(\varepsilon_3, \varepsilon_4)$ are effectively "pushed" into the high-energy landscape along with the positive-energy subspace. Therefore, the energy penalty required to virtually excite a particle out of the active low-energy subspace into any discarded state now scales with the inter-plaquette coupling. Because this "protective gap" is dynamically enhanced by J', the validity of the advanced effective projection no longer strictly requires $U \ll J$. Instead, the interaction strength must remain manageable relative to this enhanced energy scale. Consequently, increasing J' naturally broadens the window of applicable interaction strengths in the coupled-plaquette effective theory, providing us the theoretical grounds to increase U commensurately while preserving the integrity of the low-energy manifold.

Since $J' = 0.25J$ is too small to create a protective gap that allows to increase the on-site interactions beyond the threshold allowing the closing of the first, we now analyze the case $J' = J = 1$. The first check to be made is whether the first splitting crosses zero.

For $J' = J$, the closing of the first gap is at $(U/J)^* \simeq 3.707$, as shown in Fig. 3.20. Correspondingly, we recover the peculiar behaviors in all observables: the revival of chiral currents, the sharp jump in the current-current correlators, and the discontinuity in the density imbalance.

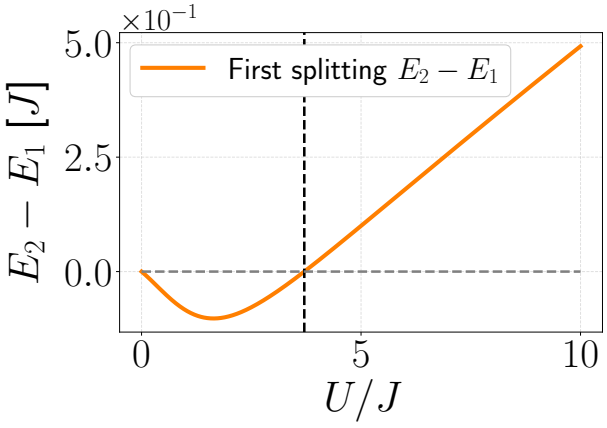

Figure 3.20: Tracked energy splitting between the ground state and first excited state as a function of U/J for $J' = J$ in the connected-plaquette effective model. The vertical line highlights the value of U/J at which the splitting crosses zero, estimated by linear interpolation between the points where the splitting changes sign at $(U/J)^* \simeq 3.707$, with $\Delta U/J = 10^{-2}$ between consecutive data points collected.

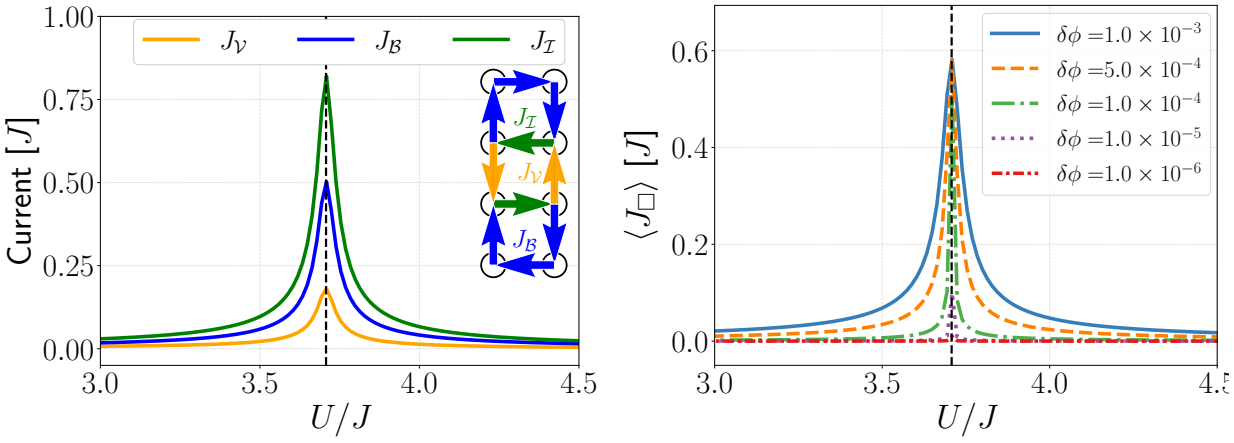

Figure 3.21: Currents in the advance effective model perturbed by a symmetry-breaking flux shift. We set $J' = J$, allowing us to explore a greater interaction range Left: Border, internal and vorticity currents as a function of U/J for a flux shift of $\delta\phi = 10^{-3}$. The inset defines the current labels and their orientations on the lattice. Right: Loop current $J_\square = \langle J_\square^{P1} \rangle = \langle J_\square^{P2} \rangle$ versus U/J for several values of the flux shift $\delta\phi \in \{10^{-3}, 2 \cdot 10^{-4}, 10^{-4}, 10^{-5}\, 10^{-6}\}$.
Both panels show a vertical line at $(U/J)^* \simeq 3.707J$, where the first excitation gap closes. This point closely coincides with the peak of the currents.

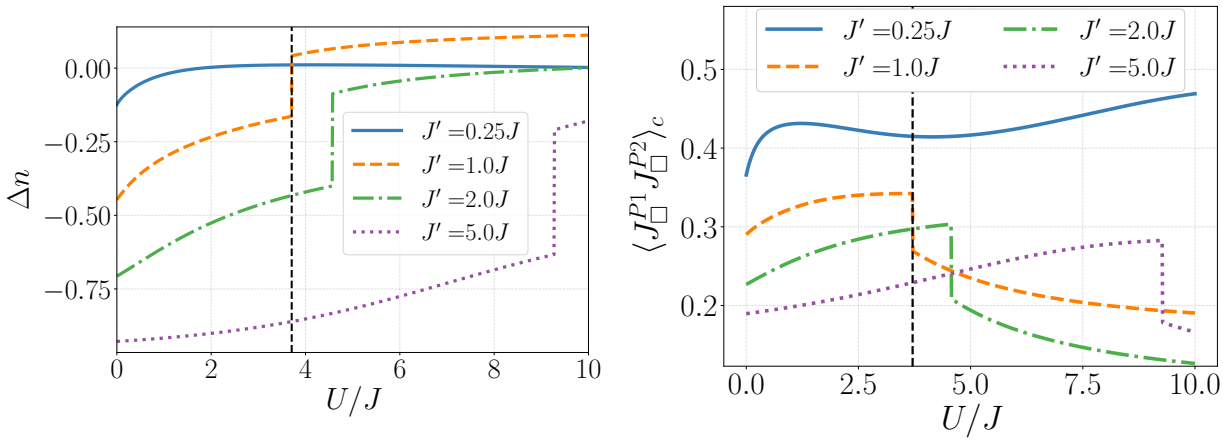

Figure 3.22: Relevant observables of the unperturbed advanced effective model for four different values of $J' \in \{0.25J, 0.15J, 0.05J, 0.01J\}$ as a function U/J. The system consists of four bosons on eight sites forming two square plaquettes linked by inter-plaquette hopping strength J'. Left: density imbalance Δn. Right: Loop current connected correlator $\langle J_{\square}^{P1} J_{\square}^{P2} \rangle_c = \langle J_{\square}^{P1} J_{\square}^{P2} \rangle - \langle J_{\square}^{P1} \rangle \langle J_{\square}^{P2} \rangle$. Both panels show a vertical line at $(U/J)^* \simeq 3.707J$, where the first excitation gap for $J' = J$ closes. This point closely coincides with the discontinuities of both density imbalance and loop current connected correlator lines for $J' = 0.25J$.

The extended-range analysis of the advanced effective theory for $J' = J$ confirms that the model successfully recovers the complete set of non-monotonic behaviors and sharp jumps observed in the exact results. The key features of these observables are described below. Fig. 3.21 (left), shows that the loop current J_{loop} exhibits a clear revival, located at the interaction strength $(U/J)^* \simeq 3.707$, which gets sharper in the limit of small shift perturbing the model ($\delta\phi \to 0$). This is mirrored in the current decomposition ($J_{\mathcal{V}}$, $J_{\mathcal{B}}$, $J_{\mathcal{J}}$), where all components follow the same non-monotonic behavior, localized at the exact point of the ground-state level crossing. The density imbalance Δn (Fig. 3.22, left) has a drastic, sharp rise at $(U/J)^*$, signaling a rapid redistribution of the bosonic density from the internal sites to the external ones. As shown in Fig. 3.22 (right) the loop current connected correlator recovers the sharp jump in correspondence of $(U/J)^*$, as well. As J'/J increases in Fig. 3.22, we observe a corresponding positive shift in the position of $(U/J)^*_r$, the point at which the first excited gap closes for each setting of the inter-plaquette hopping ratio $r = J'/J$. This also is in agreement with the results of the exact model in Fig. 3.9. Comparing this behavior with the trend of $J' = 0.25J$ (blue line in 3.22), confirms that one must increase J'/J beyond a certain threshold to recover the non-monotonic effects in this connected-plaquetted effective theory.

While this more advanced theory correctly reproduces the qualitative "jump" phenomenology of the exact model, the primary difference lies in their quantitative location. Furthermore, the qualitative agreement is also lost if the chosen inter-plaquette coupling regime is not strong enough to create the protective gap isolating the lowest energy manifold from the other orbitals retained in the theory.

Ultimately, the effectiveness of the advanced theory compared to the naive one is evident. Where the naive theory predicted a rigid, unchanging system with no current revival and incorrect negative correlations, the advanced theory pushes beyond this limits by incorporating non-perturbative orbital hybridization. It captures the competition between interaction-driven localization and coupling-driven hybridization ultimately leading to the non-trivial effects we have identified in this chapter.

Chapter 4

Two-plaquette correlations in the extended system

Having analyzed the two-plaquette system, we now understand the microscopic origin of the current revival and density reorganization as associated to the ground state level crossing. To address quantum phases rather than isolated many-body states, the next step is to move from this finite system to the thermodynamic limit. In this final chapter, we make this transition by extending the two-plaquette geometry to an infinite two-plaquette ladder. By tiling the vertically connected plaquettes along the x-direction, we obtain a system infinitely extended along one direction. This allows us to test whether the chiral dynamics and structural changes identified in the cluster persist in the macroscopic system or are confined to finite-size physics. The main challenge in extending the analysis to an infinite system is the exponential growth of the Hilbert space, which makes exact diagonalization infeasible. To connect the precise and controlled results of the local system with the thermodynamic limit, we employ the cluster Gutzwiller method. This approach retains the full many-body dynamics within a chosen cluster, preserving its accurate treatment as described in the previous chapter, while coupling the cluster to the rest of the lattice through a self-consistent mean field approach. This preserves the correlations between plaquettes in the y-direction, which are responsible for the non-monotonic behavior of the observables described earlier, while neglecting the correlations between plaquettes in the x-direction.
This chapter is structured as follows. First, we define the infinite two-plaquette ladder and its Hamiltonian. We then introduce the cluster Gutzwiller method and explain in which conditions it is well suited for determining the phase diagram of this geometry. Finally, we present the numerical results of the Gutzwiller analysis, using the two-plaquette cluster as the fundamental building block, to assess the stability of the non-monotonic effects and the emergence of chiral order in the thermodynamic limit.

4.1 The extended model: two-plaquette infinite ladder

To study the thermodynamic limit, we extend the two-plaquette system to an infinite two-plaquette ladder. The eight site geometry of the previous chapter is repeated along the x-direction and each cluster is coupled with the neighboring ones by means of a new hopping parameter J''. This parameter will later help us control the degree of approximation within the Gutzwiller method by specifically tuning down the couplings that are treated at the mean-field level. This general construction also allows us to recover the BBH structure in the limit $J'' = J'$.

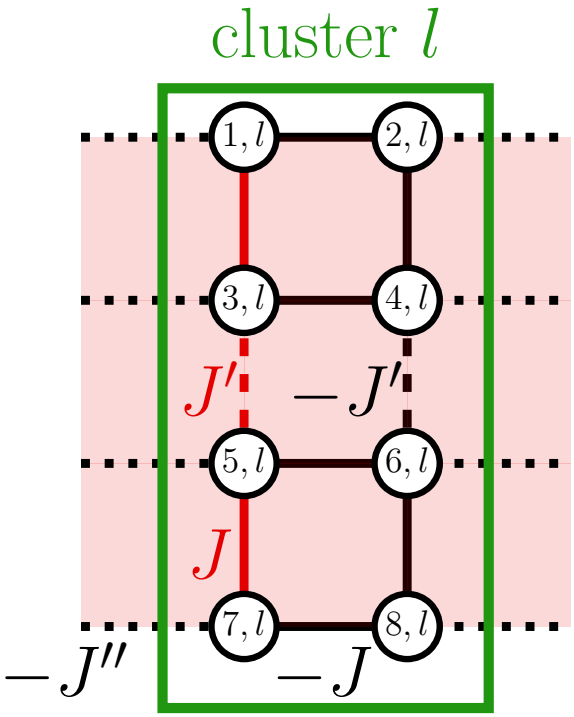

Figure 4.1: Sketch of the extended system: a cluster of two plaquettes repeated along the x-direction. Intra-plaquette bonds ($\pm J$) are shown as solid lines, intra-cluster inter-plaquette couplings ($\pm J'$) as dashed lines, while inter-cluster links are dotted lines. Lattice sites are represented by empty circles labeled by their intra-cluster index, $i \in \{1, \ldots, 8\}$, and cluster index, l. The uniform π-flux threading the whole system is represented by the red color. Links colored in red carry the sign change to implement the π-flux as specified by Landau gauge.

The Hamiltonian for the infinite system, H_{ladder}, is constructed by summing the local contributions of each unit cell l and the J''-hopping terms that connect adjacent cells. Following the conventions established for the isolated cluster, the Hamiltonian is given by:

$$H_{\text{ladder}} = \sum_{l} \left(H^{(l)}_{\text{exact}} + H^{(l,l+1)}_{J''} \right) , \tag{4.1}$$

where $H^{(l)}_{\text{exact}}$ is the Hamiltonian of the l-th unit cell containing the intra-cluster hopping parameters J and J' and the on-site interaction U (defined in Eq. (3.2) within the 8-site single-cluster Hilbert space). The new term, $H^{(l,l+1)}_{J''}$, describes the inter-cluster hopping of strength J'' that links the units along the x-direction,

$$H^{(l,l+1)}_{J''} = -J'' \sum_{i \in \{2,4,6,8\}} \left(b^{\dagger}_{i,l} b_{i-1,l+1} + \text{h.c.} \right) , \tag{4.2}$$

where now the site creation and annihilation operators are labeled by two indeces $(i,\, l)$. The first index, i, specifies the site position within each cluster, while the second, l identifies the cluster. With this convention, the Hamiltonian of the l-th unit cell is specified by

$$H^{(l)}_{\text{exact}} = H^{(l)}_{0} + H^{(l)}_{\text{int}} = -\sum_{\langle ij \rangle} \left(t_{ij}\, b^{\dagger}_{i,l} b_{j,l} + \text{h.c.} \right) + \frac{U}{2} \sum_{i} n_{i,l} \left(n_{i,l} - 1 \right) , \tag{4.3}$$

with the nonzero hopping strengths as specified in Eq. (3.4). Using the same sign convention for the hopping amplitudes within each cluster, as dictated by the Landau-like gauge choice of Eq. (3.4), is sufficient to generate a uniform magnetic flux through the entire lattice.
The resulting structure is a ladder of stacked plaquettes, which can also be seen as four parallel bosonic chains (rows) coupled vertically. Along the horizontal direction, each chain is built from alternating intra-plaquette hopping and inter-cluster hopping. Rows 1 and 2 form the upper plaquettes, connected internally by J and laterally by two J''-links. Rows 3 and 4 form the lower plaquettes, connected in the same way. The upper and lower plaquettes are linked by J'.

4.2 Cluster Gutzwiller Ansatz

To connect the exact two-plaquette results with the thermodynamic limit, we need a theoretical framework that avoids the exponential growth of the Hilbert space while retaining the essential internal dynamics of the 8-site cluster. A suitable scheme for these requirements is the extension of a single-site Gutzwiller approach [77] to a cluster Gutzwiller method [20, 74], treating the full two-plaquette cell as fundamental unit.
The Gutzwiller approach constructs a variational many-body state as a tensor product of localized wavefunctions. In the standard formulation these states live on individual lattice sites. In the cluster version used here, the infinite ladder is partitioned into unit cells indexed by l, each containing the full 8-site system. The global wavefunction of the system, $|\Psi_{\mathrm{CG}}\rangle$, is then assumed to factorize as a product state over these clusters. The global cluster Gutzwiller state is written as

$$|\Psi_{\mathrm{CG}}\rangle = \bigotimes_{l} |\Psi_l\rangle \,,$$

where $|\Psi_l\rangle$ is the many-body state of cluster l. Each cluster state is expanded in the complete Fock basis of the two-plaquette system. Using the multi-index vector $\vec{n} = (n_1, n_2, \ldots, n_8)$ to denote the occupation numbers on the eight sites, the local state takes the form:

$$|\Psi_l\rangle = \sum_{\vec{n}} C_{\vec{n}}^{(l)} |\vec{n}\rangle_l \,.$$

The complex amplitudes $C_{\vec{n}}^{(l)}$ are the variational parameters of the ansatz, directly analogous to the single-site coefficients $c_n(r)$ in the standard Gutzwiller approach. They satisfy the normalization condition $\sum_{\vec{n}} |C_{\vec{n}}^{(l)}|^2 = 1$. Assuming translational invariance along the ladder, all clusters share the same variational state, so the cluster index can be dropped and the problem reduces to solving for a single reference cluster state $|\Psi_l\rangle = |\Psi\rangle \quad \forall l$.
The assumption of a factorized wavefunction implies that there is no quantum entanglement between different clusters. Consequently, the expectation value of any inter-cluster operator factorizes into a product of intra-cluster expectation values. We exploit this property to decouple the hopping term $H_{\mathrm{hop}}^{(l,l+1)}$ that connects the horizontally adjacent plaquettes. We introduce the mean-field superfluid order parameters, defined as the expectation values of the bosonic annihilation operators at the boundary sites of the cluster:

$$\psi_i = \langle \Psi | b_i | \Psi \rangle \,,$$

where, in our case, $i \in \{1, \ldots, 8\}$ since every site of the two-plaquette system is connected to the neighboring clusters.
Following the standard mean-field decoupling used in Gutzwiller-type approaches, the hopping terms between cluster l and cluster $l+1$ are approximated by replacing the operators with their mean-field averages plus a small fluctuation. Keeping only terms linear in these fluctuations,

the inter-cluster hopping simplifies to a product between the quantum operators of sites at the boundaries of a given cluster and the classical mean-field generated by its neighbors:

$$b_{i,l}^{\dagger} b_{j,l+1} \approx \psi_i^* b_{j,l+1} + b_{i,l}^{\dagger} \psi_j - \psi_i^* \psi_j \,.$$

Within our chosen geometry, this mean-field decoupling replaces the hopping between the right side sites $\{2, 4, 6, 8\}$ of one cluster and the left-side sites $\{1, 3, 5, 7\}$ of the next with effective single-particle potentials.
By tracing out the rest of the infinite ladder, the problem reduces to finding the ground state of an effective non-linear Hamiltonian acting only on the Hilbert space of a single 8-site cluster. This Hamiltonian consists of the exact intra-cluster terms of the two-plaquette system together with the mean-field boundary contributions generated by the decoupled J'' links:

$$H_{\text{eff}} = H_{\text{exact}} - J'' \sum_{i \in \{2,4,6,8\}} \left(\psi_i^* b_{i-1} + b_i^{\dagger} \psi_{i-1} - \psi_i^* \psi_{i-1} + \text{h.c.} \right) .$$

Here, H_{exact} is the Hamiltonian of Eq. (3.2), defined in the Hilbert space of 8 sites. As this explicitly breaks the $U(1)$ global symmetry, particle number is not conserved. For this reason a chemical potential term $H_\mu = -\mu \sum_{i,l} n_{i,l}$ is added to the Hamiltonian to control the filling. Finding the ground state translates into a self-consistent eigenvalue problem.
The algorithmic implementation begins with an initial guess for the order parameters ψ_i. These local values of the mean field are substituted into H_{eff}, which is then exactly diagonalized within the truncated many-body Fock space of the 8-site cluster. The lowest-energy eigenvector provides a state $|\Psi\rangle$, from which we compute a new set of guess order parameters ψ_i. This feedback loop is iterated until convergence is reached, yielding the self-consistent ground state of the thermodynamic system under the cluster Gutzwiller approximation. Our implementation halts if two consecutive iterations yield ground state energies that differ by at most $E_{\text{err}}^{\max} = 10^{-7}$, or if the maximum number of iterations is reached: $\text{ITERATIONS}_{\max} = 4000$.
As previously stated for the isolated two-plaquette system, we focus our analysis on the case of half-filling, corresponding to an average density of $n = 0.5$ particles per site. In the grand canonical framework of the cluster Gutzwiller method, this filling is not an input parameter but must be enforced by appropriately tuning the chemical potential μ. To find the value of μ that yields the target density, we implement a root-finding procedure centered on the objective function $f(\mu) = \langle \sum_i n_i \rangle_\mu - N_c \cdot n$, where $N_c = 8$ is the number of sites in our two-plaquette cluster. We employ the Brent method (brentq) to numerically solve for $f(\mu) = 0$. This algorithm requires an initial bracketing interval $[\mu_{\min}, \mu_{\max}]$ such that the objective function changes sign at the boundaries, implying that the average occupation number at one extremum is below the target filling while the other is above. This defines a nested iteration scheme: for every evaluation of $f(\mu)$ requested by the root-finder, the algorithm must fully execute the internal self-consistent Gutzwiller loop described above to determine the stable many-body ground state $|\Psi\rangle$ and its associated density for that specific value of μ. In cases where the initial guess fails to bracket the root, our implementation is designed to automatically expand the search range by a safety margin $\Delta\mu$ until a valid interval is identified.
To ensure the robustness of our numerical results, we verify that the convergence of the algorithm is independent of the initial seed. We test various different configurations, including initializing the two plaquettes with opposite phase windings or applying a single phase winding across the entire cluster. In all cases, the system consistently converges to the same physical state. For example, in the superfluid regime, the ground state is always characterized by loop currents that share both orientation and magnitude between the two plaquettes. This confirms that the identified ground states are not artifacts of the initial guess, but identify stable chiral order. For completeness and following the methodology in [74], we initialize the complex order parameters ψ_i with a specific

phase winding. Specifically, the initial phases are set to $\{3\pi/4, \pi/2, 0, \pi/4\}$ for the first plaquette (sites $\{1, 2, 3, 4\}$), and the same pattern is repeated for the second plaquette (sites $\{5, 6, 7, 8\}$).
The improvement of this method with respect to the single-site Gutzwiller ansatz is that it treats all interactions, kinetic processes, and quantum fluctuations inside the cluster exactly. In our case, this means that the chiral loop currents, the structural rearrangements, and the localized vortex patterns of the two-plaquette system are fully captured without introducing mean-field artifacts.
However, because the wavefunction is factorized at the boundaries between clusters, this method neglects long-range entanglement and non-local quantum fluctuations beyond the 8-site unit cell. Gutzwiller-type approximations become exact in the limit of infinite coordination number, rendering them more suitable for higher spatial dimensions, consistently with the mean-field approximation. However, in quasi-one-dimensional geometries they typically overestimate the stability of ordered phases. While the intra-cluster physics is treated exactly and the method provides a reliable qualitative phase diagram, including the Mott-superfluid boundary, the location of critical points and the detailed long-distance behavior of correlations are not precisely captured in low spatial dimensions.
Furthermore, it is important to emphasize that the Gutzwiller approach is well-suited for describing the superfluid phase, where the nonzero order parameters provide a robust mean-field coupling that effectively captures the macroscopic coherence and continuous particle exchange across the lattice. Conversely, the method is fundamentally less reliable within the Mott insulating phase. Because the superfluid order parameters ψ_i vanish in the Mott state, the mean-field boundary terms in the effective Hamiltonian disappear. In this limit, the clusters become perfectly decoupled from one another, meaning that the theory fails to capture even the mean-field treatment of inter-cluster processes that are suppressed but still present in the true many-body insulator. For this reason, our interpretations in the subsequent analysis will focus primarily on the results obtained within the superfluid regime.

4.3 Numerical results of the two-plaquette cluster Gutwiller ansatz at filling $1/2$

With the theoretical and algorithmic framework of the cluster Gutzwiller method established, we now turn to the numerical results to investigate how the chiral and structural properties of the two-plaquette system translates to the infinite ladder. Our goal is to determine whether the current revival and shift in density imbalance persist as robust features of phases in the thermodynamic limit.
All the results are obtained at half filling ($n = 1/2$), and interaction strengths $U \in [0, 3]$ to enable a direct comparison with the previous section. To provide a comprehensive picture, we analyze the system across two distinct parameter regimes.
First, we focus on the weak inter-cluster regime ($J' = 10J''$), where the inter-plaquette coupling within the cluster (J') is significantly stronger than the coupling between different clusters (J''), while both are kept smaller than the intra-plaquette hopping J. This choice is motivated by the range of validity of the Gutzwiller approximation: keeping J'' small with respect to the other energy scales ensures that the mean-field decoupling acts only as a mild perturbation. This allows us to assess how robust the 8-site many-body states are when weakly connected to an infinite ladder, and to test whether the localized vortex physics of the isolated system can persist as the building block of a macroscopic phase.
Next, we remove spatial anisotropy in the hopping strengths by setting $J' = J''$. This regime recovers the standard bosonic Benalcazar-Bernevig-Hughes (BBH) model in a ladder configuration. While the BBH model has been studied using single-site and single-plaquette Gutzwiller approximations [74], our two-plaquette cluster approach goes a step further by exactly capturing plaquette correlations in the y-direction. This regime is particularly valuable because it allows us to bench-

mark our results against high-fidelity numerical methods like DMRG employed to study the BBH model, providing a rigorous check on the reliability of our cluster-based mean-field. Moreover, as shown in Subsection 3.2.2, the mirror symmetries non-trivial algebra suggests the possibility of relevant x-y correlations.
Finally, we offer additional considerations on the specific case where all inter-plaquette hopping strengths, including inter-cluster links, are set to $0.25J$. This choice reconnects the infinite-system analysis to the parameter regime used in the exact diagonalization study of the isolated two-plaquette system. It also defines a regime that can only be treated reliably within the two-plaquette cluster framework: for such relatively large inter-plaquette coupling, any smaller-cluster Gutzwiller approach would impose a harsh mean-field approximation risking failure in capturing the relevant internal dynamics of the system.
To characterize the phases and transitions of the infinite plaquette ladder, we monitor a specific set of observables that bridge our understanding of the local two-plaquette physics with the macroscopic properties of the extended lattice.

- **Superfluid order parameter** ($\psi_i = \langle b_i \rangle$), or rather, its magnitude (since in general it is a complex number). This quantity is the main diagnostic for the global phase of the system. A nonzero value of ψ_i reflects the spontaneous breaking of $U(1)$ gauge symmetry, identifying the superfluid phase. A transition to the the incompressible Mott insulating phase is signaled by a vanishing order parameter.

- **Loop Current** ($J_\square$, Eq. (3.16)). We compute the current circulating within each square unit. Given the symmetry of the ladder, which is not spontaneously broken in any of the explored parameter regimes, and our translationally invariant ansatz, the loop current remains identical for all plaquettes along the ladder. This behavior aligns with the current patterns observed in the previous sections: when present, vortices are confined to single plaquettes and share the same current magnitude and orientation. Plotting this observable allows us to check the presence of chiral order at the current level, and of non-monotonic behavior analogous to the one observed in the previous chapter.

- **Density imbalance** (Δn, Eq. 3.13). Building on our previous analysis, we study the population difference between the two mirror-distinct sets of sites: the external sites and the internal ones (see Subsection 3.2.2). Since the mirror symmetry of the ladder is not spontaneously broken in any studied parameter regime, this imbalance remains a robust measure of the structural reorganization of the bosons across the phase diagram.

- **Connected loop current correlator** ($\langle J_\square^{P1} J_\square^{P2} \rangle_c$, Eq. (3.18)). To investigate the collective chirality of the infinite system, we plot the connected correlator of the loop currents between top and bottom plaquettes. This reveals whether the chirality observed in the single cluster translates to chiral order upon extension to the thermodynamic limit.

4.3.1 Weak inter-cluster regime $J' = 10J''$

In the first parameter regime, the intra-cluster inter-plaquette coupling J' is an order of magnitude larger than the inter-cluster hopping J''. This choice introduces an anisotropy between the inter-plaquette coupling along the x and y directions, but it places the system in a parameter range where the cluster Gutzwiller ansatz is most reliable.
We characterize the existence of different macroscopic phases varying the on-site interaction strength U/J, and studying the order parameters $|\langle b_i \rangle|$ for different values of the inter-plaquette couplings, while maintaining their ratio fixed.

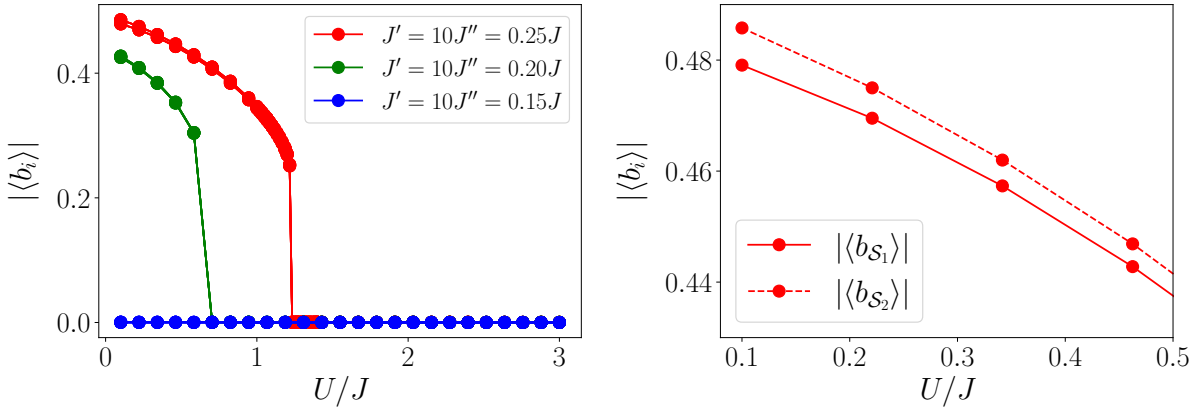

Figure 4.2: Superfluid order parameter as a function of the interaction strength U/J for the infinite two-plaquette ladder in the weak inter-cluster coupling regime ($J' = 10J''$) at filling 1/2.
Left: Phase diagram. Magnitude of the order parameter $|\langle b_i \rangle|$ for three different values of $J' = 10J'' \in \{0.25J, 0.20J, 0.15J\}$. The plot illustrates the transition from a macroscopic superfluid phase to a Mott insulating state, with the critical interaction strength U/J decreasing as the inter-plaquette coupling $J' = 10J''$ is reduced. Below a certain threshold of this parameter the phase transition occurs at U/J values below our numerical resolution, leaving the system effectively locked in the Mott insulator phase.
Right: Detailed view of the $J' = 10J'' = 0.25J$ case (red lines in both panels) for $U/J \in [0.1, 0.5]$, showing two distinct sets of order parameter values: one for the external sites $\mathcal{S}_1$ (full line), and one for the internal sites $\mathcal{S}_2$ (dashed line).

The behavior of the superfluid order parameter $|\langle b_i \rangle|$ as a function of U/J (Fig. 4.2, left) reveals a clear transition from a superfluid phase to a Mott insulating state. For $J' = 10J'' = 0.25J$, the system remains in the superfluid phase until approximately $U/J \simeq 1.2$, at which point the order parameter drops sharply to zero, signaling the entry into an incompressible Mott phase. As the inter-cluster coupling is reduced to $J' = 10J'' = 0.20J$, the superfluid phase becomes less stable, with the transition occurring at a much lower interaction strength of $U/J \simeq 0.7$. Interestingly, for the weakest coupling shown ($J' = 10J'' = 0.15J$), the order parameter remains at zero for the entire range, therefore the system seems "stuck" in the Mott insulator even for weak interactions. The kinetic energy scale is too low to delocalize bosons and the transition point is shifted at very low values of U/J not resolved by our numerics.
A closer inspection of the order parameter reveals that the "curves" in the main plot are actually composed of two closely spaced branches. As illustrated in the zoom for $J' = 10J'' = 0.25J$ (Fig. 4.2, left), the order parameters split into two distinct sets, $|\langle b_{\mathcal{S}_1} \rangle|$ and $|\langle b_{\mathcal{S}_2} \rangle|$, corresponding to the internal and external site sets of the two-plaquette cluster. The splitting reflects the internal symmetry and is linked to the different coordination numbers z characterizing the two sets ($z = 3$ for external sites and $z = 4$ for internal ones).
Within the interaction range $U/J \in [0, 3]$, we identify two distinct qualitative behaviors in the weak inter-cluster regime. Above a certain threshold of the inter-cluster coupling, exemplified by the case $J' = 10J'' = 0.25J$, the system undergoes a phase transition from a superfluid to a Mott insulator. Below this threshold, represented by $J' = 10J'' = 0.15J$, the system remains locked in the Mott insulating phase throughout the entire range of the considered interaction strengths. In the following, we analyze different observables for the parameter choice corresponding to both trends. We keep a consistent color scheme across all plots, assigning the same color to curves corresponding to the same value of $J' = 10J''$: $0.25J$ is red while $0.15J$ is blue. This ensures visual continuity throughout the section and allows direct comparison with the order parameter shown in Fig. 4.2, which is kept as reference plot.
We first analyze the loop currents to determine whether the ground state spontaneously sustains a

macroscopic current configuration in these two qualitatively distinct behavior regimes.

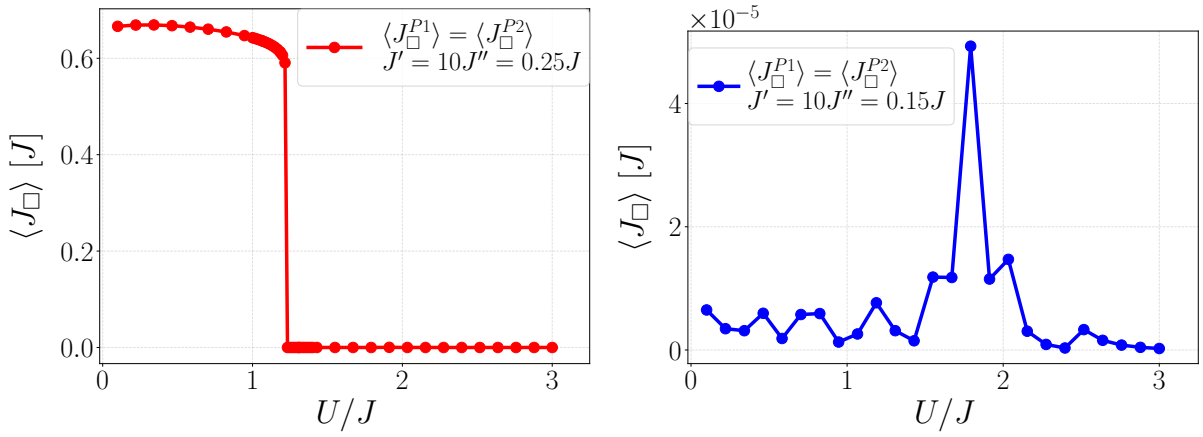

Figure 4.3: Loop current $\langle J_\square \rangle$ as a function of interaction strength U/J for the weak inter-cluster regime ($J' = 10J''$). Left: For $J' = 10J'' = 0.25J$, the system exhibits a chiral superfluid phase with substantial loop currents for $U/J < 1.2$, followed by a sharp transition to a Mott state. Right: For $J' = 10J'' = 0.15J$, the system remains in the Mott phase throughout. The negligible current magnitude (note the 10^{-5} scale) reflects the decoupling of clusters in the Gutzwiller Mott limit, simply mirroring the local physics of the isolated cluster without establishing macroscopic currents.

The loop current $\langle J_\square \rangle$ provides a direct measure of manifest chirality in the infinite ladder. In the $J' = 10J'' = 0.25J$ case (Fig. 4.3, left), we observe a significant current (starting at $\approx 0.7J$) in the low-interaction regime. The two plaquettes, and thus the whole extended system due to the imposed translational invariance, exhibit the same loop current, with equal magnitude and orientation. This is in agreement with the current patterns observed in the isolated two-plaquette system, and confirms that the superfluid phase is chiral, spontaneously breaking time-reversal symmetry. This macroscopic current persists until $U/J \simeq 1.2$, where it drops abruptly to zero, marking the transition to the Mott phase, where currents are suppressed. In contrast, for the $J' = 10J'' = 0.15J$ case (Fig. 4.3, right), the order parameter analysis previously showed that the system is entirely in the Mott phase in the explored U range. The loop current for this parameter choice exhibits a revival feature at $U/J \approx 1.9$, but it is critical to note the scale: the current is on the order of $10^{-5}J$, which is physically negligible.

While the individual loop current provides a clear signature of chirality in the superfluid phase, we must examine the loop current correlator to fully understand the chiral nature of the Mott insulating regimes. This observable allows us to look past the vanishing mean-field order parameters and detect the underlying quantum correlations that persist in the insulator.

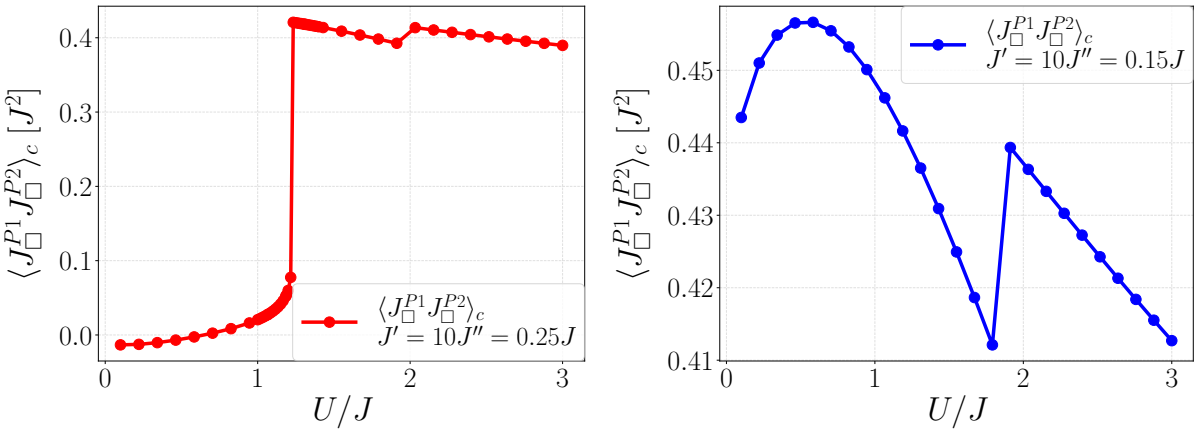

Figure 4.4: Loop current correlator $\langle J_\square^{P1} J_\square^{P2} \rangle_c$ as a function of interaction strength U/J for the weak inter-cluster regime ($J' = 10J''$). Left: For $J' = 10J'' = 0.25J$, the system transitions from a chiral superfluid to a chiral Mott state, with the transition in correspondence of a discontinuity in the correlator at $U/J \approx 1.2$. Right: For $J' = 10J'' = 0.15J$, the system remains in the Mott phase throughout. A strictly positive correlation between the loop currents of the two plaquettes reveals a chiral order even for this insulating phase.

The loop current connected correlator $\langle J_\square^{P1} J_\square^{P2} \rangle_c$ in Fig.4.4 remains strictly positive in the whole explored interaction range for $J' = 10J'' = 0.15J$. For larger values of the inter-plaquette couplings $J' = 10J'' = 0.25J$, we still observe chiral correlations for the Mott phase, which onsets at large values U/J. This signals that time-reversal symmetry is broken by quantum correlations even when the macroscopic current vanishes. Therefore, we expect that the Mott insulator phase we are observing in this parameter regime is actually a chiral Mott insulator.

Within the superfluid regime at weak interactions for $J' = 10J''$ (Fig. 4.3, left), the correlator shown in Fig. 4.4 (left) stays close to zero, being negative for small U/J and becoming positive when this ratio increases. This means that, even if the uniform-orientation vortex pattern in the superfluid phase breaks time-reversal symmetry, the vortex currents are actually not strongly correlated. As U/J increases, we observe two distinct discontinuities in the correlator. The first is a large and abrupt jump at $U/J \approx 1.2$ in correspondence with the superfluid-to-Mott (SF-MI) transition, while the second appears at a higher interaction strength of $U/J \approx 2$. In contrast, for $J' = 10J'' = 0.15J$ (Fig. 4.4, right), only a single discontinuity is present at $U/J \approx 1.9$, which coincides with the current revival artifact identified in Fig. 4.3 (right).

It is worth noting that the second discontinuity observed for $J' = 10J'' = 0.25J$ at higher values of U (Fig. 4.4, left) is likely driven by the same mechanism as the single discontinuity seen in the $J' = 10J'' = 0.15J$ case. Deep in the Mott regime, where the order parameters vanish and the clusters become effectively isolated, the system likely experiences the current revival phenomenon previously identified in the exact diagonalization of the two-plaquette system. While this feature is not visible in the loop current plot for the $J' = 0.25J$ case (Fig. 4.3, left), where the scale of the superfluid currents is several orders of magnitude larger, it becomes manifest in the current-current correlator. We do not investigate this behavior in the Mott insulator further as it is linked to the decoupling limits of the Gutzwiller approximation. The preliminary study of the isolated two-plaquette system ensures that we do not misinterpret these artifacts, as we can clearly trace their origin back to the localized physics of the 8-site cluster.

Finally, we examine the density imbalance Δn (Eq. (3.13)), which tracks the population difference between the sets of internal and external sites within the ladder. This observable provides a structural perspective on the phase transitions and further clarifies the relationship between the infinite ladder and its constituent clusters.

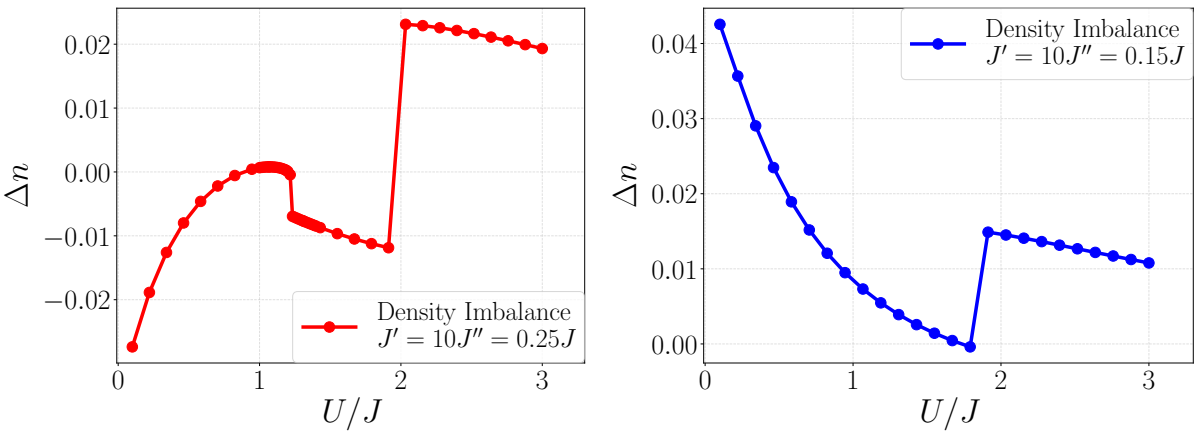

Figure 4.5: Density imbalance Δn between external and internal sites for the weak inter-cluster regime ($J' = 10J''$). Left: For $J' = 10J = 0.25J$, the imbalance, negative here, approaches zero as U/J is increased within the superfluid phase. As the system enters the Mott insulator at first there is an initial drop to lower Δn, then a sharp discontinuity brings the imbalance to positive values (external sites more populated). Right: For $J' = 0.05J$ and $J' = 0.01J$, the imbalance decays as U increases reaching zero. Then it experiences an upward jump and finally starts decaying again.

The density imbalance plots exhibit discontinuities that mirror those previously observed in the loop current correlators. In the $J' = 10J'' = 0.25J$ case (Fig. 4.5, left), the first discontinuity occurs at $U/J \approx 1.2$, directly corresponding to the chiral superfluid to chiral Mott transition. A second, much larger jump occurs at higher interaction strengths ($U/J \approx 2.0$). For the $J' = 10J'' = 0.15J$ case (Fig. 4.5, right), which remains in the Mott phase throughout the range of accessed interaction strengths, we observe a single discontinuity at $U/J \approx 1.8$. A notable feature in the $J' = 0.25J$ case is that the density imbalance crosses from negative to positive values as the interaction strength increases. However, because this reversal and the associated large jump occur deep within the Mott insulating regime, we do not assign any physical value to this behavior. As discussed in the context of the current-current correlators, these features likely signal the current revival and internal reorganization of the isolated 8-site cluster rather than a novel macroscopic phase of the extended ladder. By referencing our previous exact diagonalization results, we can confidently attribute these effects to residual single-cluster physics that becomes manifest once the Gutzwiller order parameter vanishes and the lattice effectively decouples.

In summary, within the weak inter-cluster regime,our analysis shows a transition from a chiral Mott insulator to a chiral superfluid phase that emerges only for sufficiently large inter-plaquette coupling strength $J' = 10J''$, whereas for lower coupling strengths, the system remains locked in a chiral Mott state across the entire (numerically resolved) interaction range. The chiral features of the Mott phase resemble similar results obtained in DMRG simulations of a two-leg ladder geometry in ref.[14] for $J'' = J'$. This regime will be treated in the following section.

4.3.2 BBH ladder regime $J' = J''$

We now study the case where the intra-cluster coupling J' and the inter-cluster hopping J'' are set to equal values ($J' = J''$). This configuration corresponds to the standard bosonic BBH model on a two-plaquette (or four-leg) ladder. By removing the separation between inter-cluster and (intra-cluster) inter-plaquette hopping used in the previous subsection, we can examine how the system behaves when the only source of anisotropy is the underlying lattice geometry, i.e. the contrast between the infinite longitudinal direction and the finite, four-site transverse dimension.
We begin by analyzing the phase diagram: the order parameter $|\langle b_i \rangle|$ as a function of the interaction

strength U/J for various hopping amplitudes.

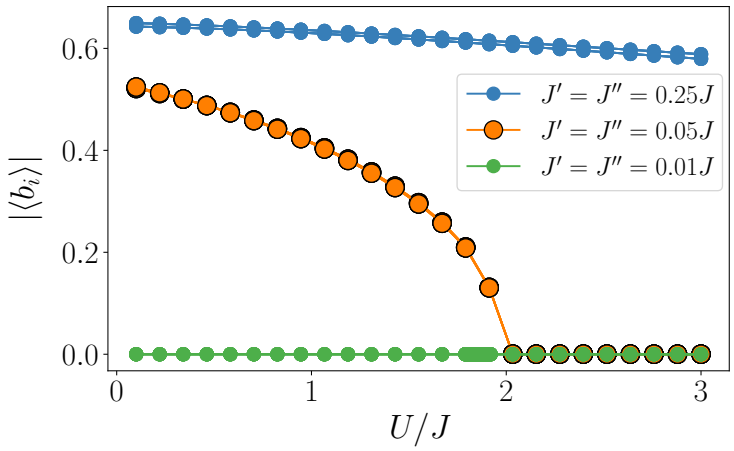

Figure 4.6: Superfluid order parameter magnitude $|\langle b_i \rangle|$ as a function of U/J for the balanced BBH ladder regime ($J' = J''$) at filling 1/2. For $J' = 0.25J$ (blue line), the system is a stable superfluid; for $J' = 0.05J$ (orange line), it undergoes a smooth transition to a Mott insulator at $U/J \approx 2$; and for $J' = 0.01J$ (green line), it remains in the Mott phase throughout the numerically resolved interaction range.

For the highest coupling considered, $J' = J'' = 0.25J$ (blue line in Fig. 4.6), the system remains entirely in the superfluid phase throughout the interaction range $U/J \in [0, 3]$. As we reduce the hopping strength to $J' = J'' = 0.05J$ (orange line in Fig. 4.6), a clear transition to the Mott insulating phase emerges. Notably, this transition appears significantly smoother than the sharp, abrupt drops observed in the weak inter-cluster regime ($J' = 10J''$, see Fig. 4.2), suggesting that the isotropic coupling allows for a continuous loss of macroscopic coherence as interactions increase. Finally, for the smallest hopping value of $J' = J'' = 0.01J$, the order parameter remains at zero for the entire range, indicating that the system is locked in a Mott insulating state even for weak interaction strengths due to the lack of sufficient kinetic energy to overcome the localizing effects of the lattice.

Following the analysis of the order parameter, we examine the loop currents $\langle J_\square \rangle$ in the BBH ladder regime to see how the restoration of spatial isotropy affects the chirality of the system. We consider the same three parameter choices to capture the distinct current behaviors associated with the fully superfluid, transitioning, and fully Mott regimes. We maintain the same color scheme: $J' = J'' = 0.25J$ data points are in blue, $J' = J'' = 0.05J$ in orange, while green lines identify $J' = J'' = 0.01$.

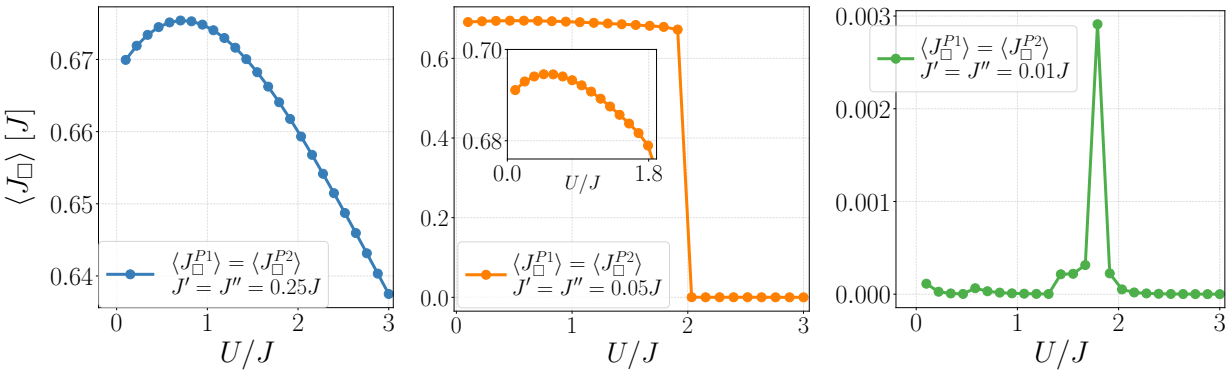

Figure 4.7: Loop current $\langle J_\square \rangle$ as a function of U/J for the BBH two-plaquette ladder ($J' = J''$). Left: For $J' = 0.25J$, the system shows a stable chiral current characteristic of the superfluid phase. This current exhibits non-monotonic behavior as U/J increases. Center: For $J' = 0.05J$, the current vanishes at the SF-MI transition point ($U/J \approx 2$). The inset provides a magnified view of the region $0 < U/J < 1.9$, highlighting that even at lower inter-plaquette coupling, the current does not increase linearly but reaches a local maximum near $U/J \approx 1$ before decreasing. Right: For $J' = 0.01J$, the system is in a Mott state, showing only a small revival peak attributable to the isolated cluster physics.

The behavior of the loop current reveals how the system's current response is modulated by both the interaction strength and the hopping amplitude. In the strongly coupled case where the system remains entirely in the superfluid phase ($J' = J'' = 0,25J$ Fig. 4.7, left), we observe a consistently high value of the loop current ($\approx 0.65J$). Interestingly, the current exhibits a non-monotonic behavior as a function of U/J. It initially increases, reaches a maximum, and then it starts declining. This trend is similar to the non-monotonicity observed in the isolated two-plaquette system in the previous chapter. This hints to a robust feature of the underlying two-plaquette geometry that survives the extension to the thermodynamic limit and causes a non-trivial current response to the variation of the on-site interaction. We will describe this behavior in more detail in the next subsection.

For intermediate coupling ($J' = J'' = 0.05J$, Fig. 4.7, center) the current starts at a magnitude similar to the previous case, exhibits a non-monotonicity of similar nature but of reduced range, signaling that this effect relies on the strength of J'. Then, the loop current drops abruptly to zero at $U/J \approx 1.5$, which coincides exactly with the vanishing of the superfluid order parameter, marking the transition from a chiral superfluid to a Mott insulator, where macroscopic particle exchange is suppressed. The presence of non-monotonic behavior in the superfluid for both parameters $J' = J'' = 0.25J$ and $J' = J'' = 0.05J$ indicates that it is a persistent feature of the system's current response across different dimerization strengths.

In the regime where the system is a Mott insulator for all explored interaction strengths ($J' = J'' = 0.01J$, Fig. 4.7, right), we once again observe a revival peak in the current at $U/J \approx 1.8$. While this revival is physically negligible compared to the superfluid currents, reaching a maximum of only $\approx 0.003J$, it is two orders of magnitude larger than the $10^{-5}J$ scale seen in the $J' = 10J''$ case and comparable to the inter-plaquette hopping strength $J' = J'' = 0.01J$. This suggests that as we approach the isotropic limit, the Gutzwiller artifact becomes slightly more pronounced, potentially indicating that these residual single-cluster features could become relevant in realizations of strongly-decoupled, isolated plaquette systems.

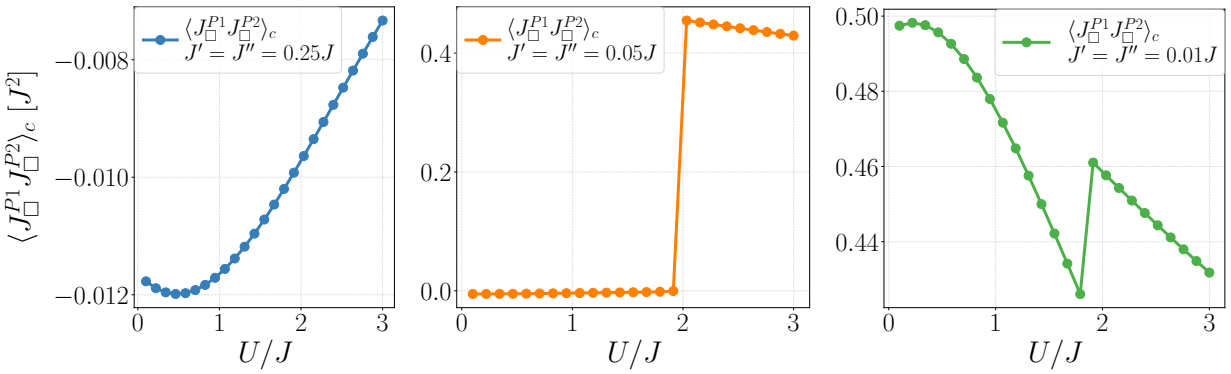

Figure 4.8: Connected loop current correlator $\langle J_{\square}^{P1} J_{\square}^{P2} \rangle_c$ as a function of U/J for the BBH two-plaquette ladder ($J' = J''$). Left: For $J' = 0.25J$, the vortex phase exhibits very weak correlations between plaquettes. Middle: For $J' = 0.05J$, a sharp transition at $U/J \approx 2$ marks the entrance into the chiral Mott insulator, characterized by a sudden onset of strong inter-plaquette current correlations. Right: For $J' = 0.01J$, the system is in the chiral Mott regime, maintaining high correlations across the entire interaction range.

The correlator behavior across the three hopping strengths highlights a fundamental shift in the system's quantum correlations. In the regime where the system is a stable superfluid (Fig. 4.8, left), we observe once again remarkably small correlations. Despite the fact that the vortices are aligned (producing a uniform macroscopic current), the connected correlator remains near zero (and slightly negative, on the scale of 10^{-2}). This suggests that the vortex order in the extended system under study is not linked to a local inter-plaquette entanglement.
Beyond the superfluid-to-Mott transition point at $U/J \approx 2$ in Fig. 4.8 (center), and for all values of the interaction strength in Fig. 4.8 (right), the correlator is characterized by positive values (≈ 0.45). As in the weak inter-cluster regime, this signals the presence of a chiral Mott state, where time reversal symmetry remains broken at the level of quantum correlations even though the observable current is zero.
To conclude our analysis of the BBH ladder regime, we examine the density imbalance Δn.

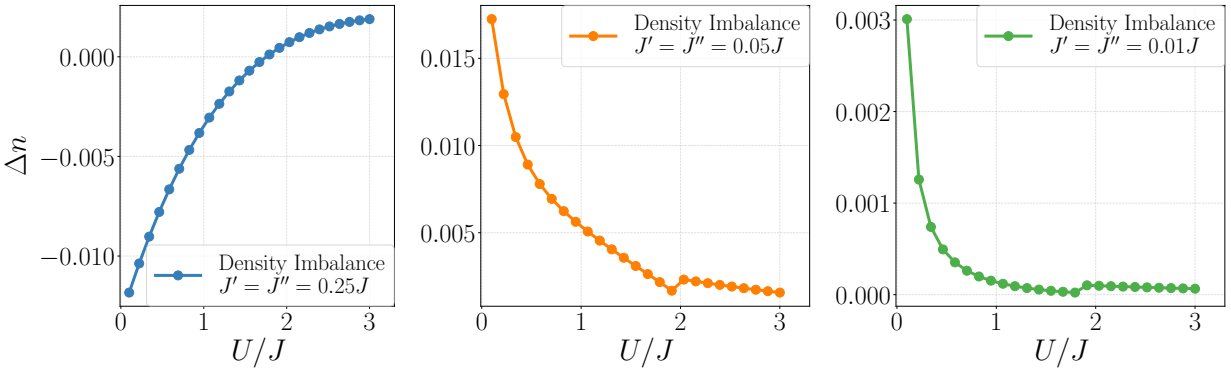

Figure 4.9: Density imbalance Δn between external and internal sites for the BBH two-plaquette ladder ($J' = J''$). Left: For $J' = 0.25J$, the imbalance exhibits a physical sign-switch within the superfluid phase, indicating a structural shift in the vortex lattice. Middle and Right: For $J' = 0.05J$ and $J' = 0.01J$, the imbalance decays as U increases, illustrating how the Mott regime drives the system toward site-homogeneity.

The most significant result in this observable occurs in the $J' = J'' = 0.25J$ case (Fig. 4.9, left), where the system remains entirely in the superfluid phase. Here, we observe the density imbalance switching sign as the interaction strength increases, crossing from negative to positive values at $U/J \approx 1.75$. Because this transition occurs well within the superfluid regime, where the Gutzwiller

ansatz is known to be robust, we can confidently identify this sign-switch as a physical feature of the vortex phase. This reversal signals a fundamental reorganization of the particle density from internal to external sites: a phenomenon we described for the two-plaquette cluster in the previous chapter. We will provide some final considerations on this behavior in the next, conclusive, subsection.
In contrast, for the $J' = 0.05J$ and $J' = 0.01J$ cases (central and left panel of Fig.4.9), the density imbalance remains consistently positive but trends rapidly toward zero as the interaction strength grows. While these plots exhibit small discontinuities around $U/J \approx 2$ and $U/J \approx 1.8$ respectively, we treat these as numerical artifacts of the Gutzwiller approximation near the phase transition and within the Mott regime. The primary physical observation here is that deep in the Mott insulator, the system penalizes any imbalance between external and internal sites, with the density profile tending toward a state of perfect balance.
In conclusion, the investigation of the BBH ladder regime ($J' = J''$) successfully captures the qualitative behavior of the chiral superfluid to chiral Mott transition, a phenomenon that has been explored in the BBH model for similar ranges of weak interaction strengths U/J and small inter-cell hopping parameter J'. Our results qualitatively align with these established findings, like the DMRG simulation that has been reviewed in Subsection 3.3.1 or recent studies employing a single-plaquette cluster Gutzwiller ansatz [74]. A key distinction between these two chiral phases as found in the present work lies in their observable signatures. The chiral superfluid is characterized by a significant macroscopic loop current, yet it exhibits remarkably low inter-plaquette current-current correlations. In contrast, while the chiral Mott insulator lacks any observable macroscopic current, the spontaneous breaking of time-reversal symmetry manifests through high, positive current-current correlations. This confirms that the transition is not merely a loss of chirality, but a shift in how that chirality is expressed: from a macroscopic flow of particles to an underlying structure of quantum current-current entanglement.
It is crucial to acknowledge a fundamental limitation of our translationally invariant cluster Gutzwiller ansatz. By enforcing that all clusters share the exact same variational state ($|\Psi_l\rangle = |\Psi\rangle$), we artificially constrain the maximum size of the magnetic and structural unit cell to our 8-site building block. Consequently, this approach inherently suppresses any macroscopic phase that lowers its energy by spontaneously breaking discrete translational symmetry over longer length scales. For instance, Charge-Density Wave (CDW) states with lower fractional fillings, or complex Vortex Lattices with a periodicity spanning multiple clusters, are mathematically prohibited from emerging in this framework. Therefore, the phase diagrams we have observed in this section must be understood as the landscape of competing orders that are strictly commensurate with the two-plaquette geometry.

4.3.3 Biased-Ladder Phase hypothesis and transverse correlations

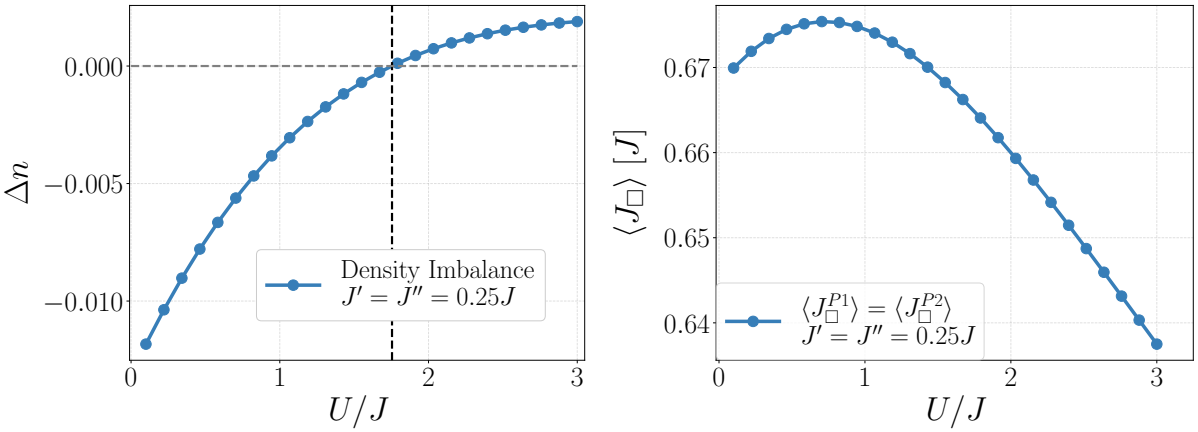

Figure 4.10: Detailed view of the structural and chiral observables for the two-plaqutte BBH ladder in the superfluid regime ($J' = J'' = 0.25J$), illustrating the most interesting results of this chapter. Left: The density imbalance Δn as a function of U/J. The continuous transition from negative to positive values (crossing at $U/J \simeq 1.755$) marks the reorganization of bosons from internal bridge sites to the external legs of the ladder. Right: The loop current $\langle J_\square \rangle$ exhibiting non-monotonic behavior, reminiscing of the local many-body physics of the isolated two-plaquette cluster. These plots, obtained employing the two-plaquette cluster Gutzwiller ansatz, and previously presented in the general analysis of Subsection 4.3.2, are reproduced here to highlight their connection with the rest of this thesis.

We conclude this analysis by bridging our macroscopic findings for the BBH two-plaquette ladder ($J' = J'' = 0.25J$) with the exact many-body physics of the isolated two-plaquette cluster. In the thermodynamic limit, the sharp ground-state level crossing observed in the isolated exact diagonalization is smoothed out by the macroscopic inter-cluster coupling. Nevertheless, its structural signatures seem to persist in the superfluid phase as continuous transitions. Specifically, the non-monotonic behavior of the chiral loop current is accompanied by a continuous shift in the density imbalance, which smoothly crosses from negative to positive values as the interaction strength increases. This continuous transition hints at a physical mechanism analogous to the Biased-Ladder Phase (BLP) found in strongly anisotropic two-leg ladders where bosons spontaneously prefer one leg over the other, as described in Section 2.4. As seen in Fig. 4.10 (left), at low interaction strengths ($U/J < 1.755$), the system favors the occupation of the internal sites, those that bridge the two plaquettes, to maximize the kinetic energy associated with the transverse hopping J'. However, for larger values of U, the energetic cost of particle overlap forces the bosonic fluid to reorganize, pushing the density outward to the external sites. This macroscopic density shift and the current non-monotonicity are fundamentally driven by the quantum correlations along the transverse (y) direction. This mechanism aligns with the known physics of two-leg ladders, where Biased Ladder Phases (BLP) are typically stabilized by strong rung anisotropy or enhanced transverse correlations. However, unlike the BLP, which breaks the discrete $\mathbb{Z}_2$ leg-exchange symmetry, the density pattern identified here preserves the mirror symmetries of the lattice. Instead, it displays two distinct profiles of density modulations along the y-direction ($\Delta n > 0$ and $\Delta n < 0$). By incorporating intra-cluster many-body signatures, our two-plaquette Gutzwiller approach illustrates how the complex internal dynamics of the isolated building block successfully scales to determine the structural and chiral order of the macroscopic superfluid. Nevertheless, a more rigorous assessment is required to definitively establish the existence of this candidate phase and fully characterize its properties. In particular, tracking the evolution of the density imbalance at larger values of J', deeper into the superfluid regime, would clarify whether these structural modulations are further enhanced, providing a more definitive signature of a stable thermodynamic phase. A definitive characterization

would necessitate an extensive study of suitable order parameters and a systematic comparison across multiple numerical methods, such as Density Matrix Renormalization Group (DMRG) simulations for the same BBH ladder configuration, to validate the cluster Gutzwiller predictions and determine if the observed density modulations survive the inclusion of full quantum fluctuations.

Conclusions

In this thesis, we investigate the interplay between on-site interactions and synthetic gauge fields within a quasi-one-dimensional π-flux lattice. After extensively reviewing the many-body quantum phases achievable in the flux-frustrated Bose-Hubbard model and their connection to topological phases of matter, our analysis begins with the study of a two-plaquette Benalcazar-Bernevig-Hughes (BBH) building block. A preliminary symmetry analysis of the model allows us to restrict our focus to a set of meaningful physical observables that fully characterize the local system. Using exact diagonalization, we identify remarkable non-monotonic behavior in these observables. The system exhibits a form of "interaction-assisted enhanced mobility", where loop currents undergo a revival at finite values of the on-site interaction. Simultaneously, the density profile of the system is redistributed from the internal sites toward the external ones, hinting at a non-trivial many-body effect that reshapes the ground-state configuration. We show how these effects are related to a ground-state level crossing in the many-body spectrum of the Hamiltonian. We employ a single-plaquette-based effective theory to describe the spectrum in terms of an emergent angular momentum, where the angular-momentum-maximizing ground state is linked to chiral vortex order. By constructing a more advanced, two-plaquette-based effective theory, we demonstrate that the peculiar features observed in the exact model, which elude the single-plaquette description, are qualitatively recovered when the inter-plaquette coupling is treated non-perturbatively and its dependence is retained in the low-energy orbitals defining the projection subspace of the theory. In light of these results, we consider an extension of the system to the thermodynamic limit by tiling the studied building block along the longitudinal direction. We employ a two-plaquette cluster Gutzwiller ansatz to reconstruct the phase diagram of this infinite two-plaquette ladder, providing a natural next step to studies focusing on single-site and single-plaquette Gutzwiller formulations. We successfully capture the transition from a chiral superfluid to a chiral Mott insulator, aligning with established findings from DMRG simulations. Remarkably, within the superfluid phase, where the Gutzwiller ansatz is most reliable, we observe a non-monotonic behavior of the loop current, which we link to the non-trivial current responses identified in the isolated cluster. Furthermore, this superfluid phase exhibits a non-homogeneous density profile which, as in the single-cluster case, shifts the occupation preference from internal sites to the external edges of the ladder. This suggests that the distinct phenomena analyzed in the isolated two-plaquette cluster are robust features that persist in the macroscopic superfluid system. This phase, which displays two distinct regimes characterized by the sign of the density imbalance, resembles, yet for symmetry reasons differs from, the Biased-Ladder phase reported for flux-frustrated two-leg ladders discussed earlier in this thesis.

While the cluster Gutzwiller method provides a reliable qualitative overview of the phase landscape, it possesses inherent limitations in low-dimensional geometries. Moving forward, we identify several avenues for research to deepen our understanding of these frustrated systems. To accurately account for the long-range entanglement and non-local quantum fluctuations that the Gutzwiller ansatz neglects, the system could be studied using Density Matrix Renormalization Group (DMRG) algorithms. This will allow for a precise determination of the critical points and the identification

of the exact nature of the phase transitions in the quasi-1D ladder geometry.
Further studies are required to characterize the "Biased-Ladder Phase" hypothesis suggested by our results. Defining and measuring new correlation functions and order parameters will be essential to distinguish this phase from a standard vortex superfluids.
A crucial technical improvement involves modifying the Cluster Gutzwiller implementation to allow for non-translational invariant solutions. By not imposing translational symmetry and allowing for multiple clusters in the variational state, the system could explore phases with larger magnetic unit cells or broken spatial symmetries. This modification is particularly important for investigating the Meissner phase, which is of great interest due to its characteristic border currents. Such currents are reminiscent of the chiral edge states found in Quantum Hall (QH) systems. In our current translationally invariant setup, these peculiar phases may be suppressed or hidden, and relaxing this constraint is the next step to search for topological signatures in the model.
The study of flux-frustrated bosonic lattices proves its value in probing how many-body interactions, geometry, symmetry, and magnetic frustration compete to realize unconventional phases. By connecting the local microscopic features of the isolated cluster to the collective behavior that emerges in the extended system, this work aims to contribute to the study of chiral states that are within the reach of quantum simulators. By improving numerical methods and techniques, our future goal is to precisely characterize interaction-driven chiral phases in the symmetric setting of the BBH model, and eventually discover lattice analogues of fractional quantum Hall physics, with fundamental implications for our understanding of correlated quantum matter.

Appendix A

A more direct construction of the advanced effective theory can be obtained by relaxing the constraint that the single-particle eigenstates defining the orbitals must be simultaneous eigenstates of both of H_0 (Eq. (3.5)) and M_x (Eq. (3.11)). Since the spectrum of H_0 is doubly degenerate, this usually requires the orthonormalization within each degenerate subspace of the single-particle eigenstates of H_0. By applying a Gram-Schmidt orthonormalization, we obtain a physically meaningful orthonormal basis inside each degenerate subspace. The (complex) orthonormalized eigenvectors corresponding to the lowest four energies are used to define single-particle orbitals. In this basis, all entries (256) of $V_{\alpha\beta\gamma\delta}$ are generically non-vanishing, and the tensor is characterized by 14 different possible coupling strengths. The following table summarizes the non-zero elements of the projected interaction tensor $V_{\alpha\beta\gamma\delta}$ in this basis.

Coefficient	**Index quadruples** (i,j,k,l)
$-\frac{r(4-r+r^2)}{4(4+r^2)^2}$	$\{(1,1,1,4) + P_1\}$
$\frac{r(4-r+r^2)}{4(4+r^2)^2}$	$\{(2,2,2,3) + P_1\}$
$-\frac{r(4+r+r^2)}{4(4+r^2)^2}$	$\{(3,3,3,2) + P_1\}$
$\frac{r(4+r+r^2)}{4(4+r^2)^2}$	$\{(4,4,4,1) + P_1\}$
$\frac{6+5r^2+r^4}{2(4+r^2)^2}$	$\{(1,1,1,1),(2,2,2,2),(3,3,3,3),(4,4,4,4)\}$
$\frac{6+r^2}{2(4+r^2)^2}$	$\{(1,1,4,4),(2,2,3,3) + P_1 + P_2\}$
$-\frac{r(2+r^2)}{4(4+r^2)^2}$	$\{(1,1,1,2),(1,1,1,3),(2,2,2,4),(3,3,3,4) + P_1\}$
$\frac{r(2+r^2)}{4(4+r^2)^2}$	$\{(1,2,2,2),(1,3,3,3),(2,4,4,4),(3,4,4,4) + P_1\}$
$\frac{1}{(4+r^2)^2}$	$\{(1,2,3,4) + P_1\}$
$-\frac{r^2}{4(4+r^2)^2}$	$\{(1,2,2,4),(1,3,3,4) + P_1 + P_2\}$
$\frac{r^2}{4(4+r^2)^2}$	$\{(1,1,2,3),(2,3,4,4) + P_1 + P_2\}$
$\frac{2+r^2}{2(4+r^2)^2}$	$\{(1,1,2,2),(1,1,3,3),(2,2,4,4),(3,3,4,4) + P_1 + P_2\}$
$-\frac{r}{2(4+r^2)^2}$	$\{(1,1,2,4),(1,1,3,4),(1,2,2,3),(1,2,3,3) + P_1 + P_2\}$
$\frac{r}{2(4+r^2)^2}$	$\{(1,2,4,4),(1,3,4,4),(2,2,3,4),(2,3,3,4) + P_1 + P_2\}$

Here P_1 and P_2 are, respectively, the 1-permutations and 2-permutations of the previously listed indeces.

This construction is perfectly equivalent to the one reported in Subsection 3.4.1, and is characterized by far simpler symbolic expressions of the coupling strengths. However, it is not directly comparable with the naive isolated-plaquette effective theory, thuerefore we detail the mirror symmetry-adapted construction in the main text.

Bibliography

[1] Ulrich Schollwöck. The density-matrix renormalization group in the age of matrix product states. *Annals of Physics*, 326(1):96–192, 2011. ISSN 0003-4916. doi: https://doi.org/10.1016/j.aop.2010.09.012. URL https://www.sciencedirect.com/science/article/pii/S0003491610001752. January 2011 Special Issue.

[2] D. J. Thouless, M. Kohmoto, M. P. Nightingale, and M. den Nijs. Quantized hall conductance in a two-dimensional periodic potential. *Phys. Rev. Lett.*, 49:405–408, Aug 1982. doi: 10.1103/PhysRevLett.49.405. URL https://link.aps.org/doi/10.1103/PhysRevLett.49.405.

[3] Lev Davidovich Landau et al. On the theory of phase transitions. *Zh. eksp. teor. Fiz*, 7(19-32): 926, 1937.

[4] Chetan Nayak, Steven H. Simon, Ady Stern, Michael Freedman, and Sankar Das Sarma. Non-abelian anyons and topological quantum computation. *Rev. Mod. Phys.*, 80:1083–1159, Sep 2008. doi: 10.1103/RevModPhys.80.1083. URL https://link.aps.org/doi/10.1103/RevModPhys.80.1083.

[5] K. v. Klitzing, G. Dorda, and M. Pepper. New method for high-accuracy determination of the fine-structure constant based on quantized hall resistance. *Phys. Rev. Lett.*, 45:494–497, Aug 1980. doi: 10.1103/PhysRevLett.45.494. URL https://link.aps.org/doi/10.1103/PhysRevLett.45.494.

[6] Christian Gross and Immanuel Bloch. Quantum simulations with ultracold atoms in optical lattices. *Science*, 357(6355):995–1001, 2017. doi: 10.1126/science.aal3837. URL https://www.science.org/doi/abs/10.1126/science.aal3837.

[7] Matthew P. A. Fisher, Peter B. Weichman, G. Grinstein, and Daniel S. Fisher. Boson localization and the superfluid-insulator transition. *Phys. Rev. B*, 40:546–570, Jul 1989. doi: 10.1103/PhysRevB.40.546. URL https://link.aps.org/doi/10.1103/PhysRevB.40.546.

[8] Immanuel Bloch, Jean Dalibard, and Wilhelm Zwerger. Many-body physics with ultracold gases. *Rev. Mod. Phys.*, 80:885–964, Jul 2008. doi: 10.1103/RevModPhys.80.885. URL https://link.aps.org/doi/10.1103/RevModPhys.80.885.

[9] D. Jaksch, C. Bruder, J. I. Cirac, C. W. Gardiner, and P. Zoller. Cold bosonic atoms in optical lattices. *Phys. Rev. Lett.*, 81:3108–3111, Oct 1998. doi: 10.1103/PhysRevLett.81.3108. URL https://link.aps.org/doi/10.1103/PhysRevLett.81.3108.

[10] Markus Greiner, Olaf Mandel, Tilman Esslinger, Theodor W. Hänsch, and Immanuel Bloch. Quantum phase transition from a superfluid to a Mott insulator in a gas of ultracold atoms. *Nature*, 415(6867):39–44, 2002. doi: 10.1038/415039a. URL https://doi.org/10.1038/415039a.

[11] A. Celi, P. Massignan, J. Ruseckas, N. Goldman, I. B. Spielman, G. Juzeliūnas, and M. Lewenstein. Synthetic gauge fields in synthetic dimensions. *Phys. Rev. Lett.*, 112:043001, Jan

2014. doi: 10.1103/PhysRevLett.112.043001. URL https://link.aps.org/doi/10.1103/PhysRevLett.112.043001.

[12] M. Aidelsburger, M. Atala, M. Lohse, J. T. Barreiro, B. Paredes, and I. Bloch. Realization of the hofstadter hamiltonian with ultracold atoms in optical lattices. *Physical Review Letters*, 111(18), October 2013. ISSN 1079-7114. doi: 10.1103/physrevlett.111.185301. URL http://dx.doi.org/10.1103/PhysRevLett.111.185301.

[13] Hirokazu Miyake, Georgios A. Siviloglou, Colin J. Kennedy, William Cody Burton, and Wolfgang Ketterle. Realizing the harper hamiltonian with laser-assisted tunneling in optical lattices. *Phys. Rev. Lett.*, 111:185302, Oct 2013. doi: 10.1103/PhysRevLett.111.185302. URL https://link.aps.org/doi/10.1103/PhysRevLett.111.185302.

[14] Marco Di Liberto and Nathan Goldman. Chiral orbital order of interacting bosons without higher bands. *Phys. Rev. Res.*, 5:023064, Apr 2023. doi: 10.1103/PhysRevResearch.5.023064. URL https://link.aps.org/doi/10.1103/PhysRevResearch.5.023064.

[15] Xiaopeng Li and W Vincent Liu. Physics of higher orbital bands in optical lattices: a review. *Reports on Progress in Physics*, 79(11):116401, 2016. URL https://iopscience.iop.org/article/10.1088/0034-4885/79/11/116401/.

[16] Rudolf Peierls. Zur theorie des diamagnetismus von leitungselektronen. *Zeitschrift für Physik*, 80(11–12):763–791, 1933. doi: 10.1007/BF01342591.

[17] M. Piraud, F. Heidrich-Meisner, I. P. McCulloch, S. Greschner, T. Vekua, and U. Schollwöck. Vortex and meissner phases of strongly interacting bosons on a two-leg ladder. *Phys. Rev. B*, 91:140406, Apr 2015. doi: 10.1103/PhysRevB.91.140406. URL https://link.aps.org/doi/10.1103/PhysRevB.91.140406.

[18] S. Greschner, M. Piraud, F. Heidrich-Meisner, I. P. McCulloch, U. Schollwöck, and T. Vekua. Symmetry-broken states in a system of interacting bosons on a two-leg ladder with a uniform abelian gauge field. *Phys. Rev. A*, 94:063628, Dec 2016. doi: 10.1103/PhysRevA.94.063628. URL https://link.aps.org/doi/10.1103/PhysRevA.94.063628.

[19] Wladimir A. Benalcazar, B. Andrei Bernevig, and Taylor L. Hughes. Quantized electric multipole insulators. *Science*, 357(6346):61–66, 2017. doi: 10.1126/science.aah6442. URL https://www.science.org/doi/abs/10.1126/science.aah6442.

[20] Dirk-Sören Lühmann. Cluster gutzwiller method for bosonic lattice systems. *Phys. Rev. A*, 87:043619, Apr 2013. doi: 10.1103/PhysRevA.87.043619. URL https://link.aps.org/doi/10.1103/PhysRevA.87.043619.

[21] Y. Aharonov and D. Bohm. Significance of electromagnetic potentials in the quantum theory. *Phys. Rev.*, 115:485–491, Aug 1959. doi: 10.1103/PhysRev.115.485. URL https://link.aps.org/doi/10.1103/PhysRev.115.485.

[22] Akira Tonomura, Nobuyuki Osakabe, Tsuyoshi Matsuda, Takeshi Kawasaki, Junji Endo, Shinichiro Yano, and Hiroji Yamada. Evidence for aharonov-bohm effect with magnetic field completely shielded from electron wave. *Phys. Rev. Lett.*, 56:792–795, Feb 1986. doi: 10.1103/PhysRevLett.56.792. URL https://link.aps.org/doi/10.1103/PhysRevLett.56.792.

[23] J. M. Luttinger. The effect of a magnetic field on electrons in a periodic potential. *Phys. Rev.*, 84:814–817, Nov 1951. doi: 10.1103/PhysRev.84.814. URL https://link.aps.org/doi/10.1103/PhysRev.84.814.

[24] Douglas R. Hofstadter. Energy levels and wave functions of bloch electrons in rational and

irrational magnetic fields. *Phys. Rev. B*, 14:2239–2249, Sep 1976. doi: 10.1103/PhysRevB.14.2239. URL https://link.aps.org/doi/10.1103/PhysRevB.14.2239.

[25] Qian Niu, D. J. Thouless, and Yong-Shi Wu. Quantized hall conductance as a topological invariant. *Phys. Rev. B*, 31:3372–3377, Mar 1985. doi: 10.1103/PhysRevB.31.3372. URL https://link.aps.org/doi/10.1103/PhysRevB.31.3372.

[26] Joseph E. Avron and Ruedi Seiler. Quantization of the hall conductance for general, multiparticle schrödinger hamiltonians. *Phys. Rev. Lett.*, 54:259–262, Jan 1985. doi: 10.1103/PhysRevLett.54.259. URL https://link.aps.org/doi/10.1103/PhysRevLett.54.259.

[27] John Cardy. *Scaling and renormalization in statistical physics*, volume 5. Cambridge university press, 1996.

[28] Pasquale Calabrese and John Cardy. Entanglement entropy and quantum field theory. *Journal of Statistical Mechanics: Theory and Experiment*, 2004(06):P06002, jun 2004. doi: 10.1088/1742-5468/2004/06/P06002. URL https://doi.org/10.1088/1742-5468/2004/06/P06002.

[29] Thierry Giamarchi. *Quantum physics in one dimension*, volume 121. Clarendon press, 2003.

[30] E. Orignac and T. Giamarchi. Meissner effect in a bosonic ladder. *Phys. Rev. B*, 64:144515, Sep 2001. doi: 10.1103/PhysRevB.64.144515. URL https://link.aps.org/doi/10.1103/PhysRevB.64.144515.

[31] Alexander Impertro, SeungJung Huh, Simon Karch, Julian F. Wienand, Immanuel Bloch, and Monika Aidelsburger. Strongly interacting meissner phases in large bosonic flux ladders. *Nature Physics*, 21(6):895–901, 2025. doi: 10.1038/s41567-025-02890-0.

[32] G. Blatter, M. V. Feigel'man, V. B. Geshkenbein, A. I. Larkin, and V. M. Vinokur. Vortices in high-temperature superconductors. *Rev. Mod. Phys.*, 66:1125–1388, Oct 1994. doi: 10.1103/RevModPhys.66.1125. URL https://link.aps.org/doi/10.1103/RevModPhys.66.1125.

[33] Dean Johnstone, Patrik Öhberg, and Callum W. Duncan. Interacting bosons on crystalline and quasiperiodic ladders in a magnetic field. *Phys. Rev. Res.*, 5:023195, Jun 2023. doi: 10.1103/PhysRevResearch.5.023195. URL https://link.aps.org/doi/10.1103/PhysRevResearch.5.023195.

[34] Quantum phases in the extended bose–hubbard ladder. *Physica A: Statistical Mechanics and its Applications*, 623:128838, 2023. ISSN 0378-4371. doi: https://doi.org/10.1016/j.physa.2023.128838. URL https://www.sciencedirect.com/science/article/pii/S037843712300393X.

[35] Mohammadamin Jaberi and Fatemeh Heydarinasab. Bose-hubbard model in the presence of artificial magnetic fields: Ground state and thermal phase diagrams, 2025. URL https://arxiv.org/abs/2507.11914.

[36] Johannes Hauschild, Jakob Unfried, Sajant Anand, Bartholomew Andrews, Marcus Bintz, Umberto Borla, Stefan Divic, Markus Drescher, Jan Geiger, Martin Hefel, Kévin Hémery, Wilhelm Kadow, Jack Kemp, Nico Kirchner, Vincent S. Liu, Gunnar Möller, Daniel Parker, Michael Rader, Anton Romen, Samuel Scalet, Leon Schoonderwoerd, Maximilian Schulz, Tomohiro Soejima, Philipp Thoma, Yantao Wu, Philip Zechmann, Ludwig Zweng, Roger S. K. Mong, Michael P. Zaletel, and Frank Pollmann. Tensor network Python (TeNPy) version 1. *SciPost Phys. Codebases*, page 41, 2024. doi: 10.21468/SciPostPhysCodeb.41. URL https://scipost.org/10.21468/SciPostPhysCodeb.41.

[37] Steven R. White. Density matrix formulation for quantum renormalization groups. *Phys. Rev.*

Lett., 69:2863–2866, Nov 1992. doi: 10.1103/PhysRevLett.69.2863. URL https://link.aps.org/doi/10.1103/PhysRevLett.69.2863.

[38] Pasquale Calabrese and John Cardy. Entanglement entropy and quantum field theory. *Journal of Statistical Mechanics: Theory and Experiment*, 2004(06):P06002, jun 2004. doi: 10.1088/1742-5468/2004/06/P06002. URL https://doi.org/10.1088/1742-5468/2004/06/P06002.

[39] Xiao-Gang Wen. Colloquium: Zoo of quantum-topological phases of matter. *Rev. Mod. Phys.*, 89:041004, Dec 2017. doi: 10.1103/RevModPhys.89.041004. URL https://link.aps.org/doi/10.1103/RevModPhys.89.041004.

[40] Michael Victor Berry. Quantal phase factors accompanying adiabatic changes. *Proceedings of the Royal Society of London. A. Mathematical and Physical Sciences*, 392(1802):45–57, 03 1984. ISSN 0080-4630. doi: 10.1098/rspa.1984.0023. URL https://doi.org/10.1098/rspa.1984.0023.

[41] Di Xiao, Ming-Che Chang, and Qian Niu. Berry phase effects on electronic properties. *Rev. Mod. Phys.*, 82:1959–2007, Jul 2010. doi: 10.1103/RevModPhys.82.1959. URL https://link.aps.org/doi/10.1103/RevModPhys.82.1959.

[42] Ching-Kai Chiu, Jeffrey C. Y. Teo, Andreas P. Schnyder, and Shinsei Ryu. Classification of topological quantum matter with symmetries. *Rev. Mod. Phys.*, 88:035005, Aug 2016. doi: 10.1103/RevModPhys.88.035005. URL https://link.aps.org/doi/10.1103/RevModPhys.88.035005.

[43] Xie Chen, Zheng-Cheng Gu, and Xiao-Gang Wen. Local unitary transformation, long-range quantum entanglement, wave function renormalization, and topological order. *Phys. Rev. B*, 82:155138, Oct 2010. doi: 10.1103/PhysRevB.82.155138. URL https://link.aps.org/doi/10.1103/PhysRevB.82.155138.

[44] X. G. WEN. Topological orders in rigid states. *International Journal of Modern Physics B*, 04(02):239–271, 1990. doi: 10.1142/S0217979290000139. URL https://doi.org/10.1142/S0217979290000139.

[45] R. B. Laughlin. Anomalous quantum hall effect: An incompressible quantum fluid with fractionally charged excitations. *Phys. Rev. Lett.*, 50:1395–1398, May 1983. doi: 10.1103/PhysRevLett.50.1395. URL https://link.aps.org/doi/10.1103/PhysRevLett.50.1395.

[46] Frank Wilczek. Quantum mechanics of fractional-spin particles. *Phys. Rev. Lett.*, 49:957–959, Oct 1982. doi: 10.1103/PhysRevLett.49.957. URL https://link.aps.org/doi/10.1103/PhysRevLett.49.957.

[47] Alexei Kitaev and John Preskill. Topological entanglement entropy. *Phys. Rev. Lett.*, 96:110404, Mar 2006. doi: 10.1103/PhysRevLett.96.110404. URL https://link.aps.org/doi/10.1103/PhysRevLett.96.110404.

[48] X. G. Wen. Chiral luttinger liquid and the edge excitations in the fractional quantum hall states. *Phys. Rev. B*, 41:12838–12844, Jun 1990. doi: 10.1103/PhysRevB.41.12838. URL https://link.aps.org/doi/10.1103/PhysRevB.41.12838.

[49] C. L. Kane and Matthew P. A. Fisher. Thermal transport in a luttinger liquid. *Phys. Rev. Lett.*, 76:3192–3195, Apr 1996. doi: 10.1103/PhysRevLett.76.3192. URL https://link.aps.org/doi/10.1103/PhysRevLett.76.3192.

[50] D. C. Tsui, H. L. Stormer, and A. C. Gossard. Two-dimensional magnetotransport in the extreme quantum limit. *Phys. Rev. Lett.*, 48:1559–1562, May 1982. doi: 10.1103/PhysRevLett.48.1559. URL https://link.aps.org/doi/10.1103/PhysRevLett.48.1559.

[51] Andreas P. Schnyder, Shinsei Ryu, Akira Furusaki, and Andreas W. W. Ludwig. Classification of topological insulators and superconductors in three spatial dimensions. *Phys. Rev. B*, 78: 195125, Nov 2008. doi: 10.1103/PhysRevB.78.195125. URL https://link.aps.org/doi/10.1103/PhysRevB.78.195125.

[52] Alexei Kitaev. Periodic table for topological insulators and superconductors. *AIP Conference Proceedings*, 1134(1):22–30, 05 2009. ISSN 0094-243X. doi: 10.1063/1.3149495. URL https://doi.org/10.1063/1.3149495.

[53] Frank Pollmann, Erez Berg, Ari M. Turner, and Masaki Oshikawa. Symmetry protection of topological phases in one-dimensional quantum spin systems. *Phys. Rev. B*, 85:075125, Feb 2012. doi: 10.1103/PhysRevB.85.075125. URL https://link.aps.org/doi/10.1103/PhysRevB.85.075125.

[54] Xie Chen, Zheng-Cheng Gu, Zheng-Xin Liu, and Xiao-Gang Wen. Symmetry-protected topological orders in interacting bosonic systems. *Science*, 338(6114):1604–1606, 2012. doi: 10.1126/science.1227224. URL https://www.science.org/doi/abs/10.1126/science.1227224.

[55] Daniel S. Freed. Short-range entanglement and invertible field theories, 2014. URL https://arxiv.org/abs/1406.7278.

[56] Michael Levin and Zheng-Cheng Gu. Braiding statistics approach to symmetry-protected topological phases. *Phys. Rev. B*, 86:115109, Sep 2012. doi: 10.1103/PhysRevB.86.115109. URL https://link.aps.org/doi/10.1103/PhysRevB.86.115109.

[57] Yuanbo Zhang, Yan-Wen Tan, Horst L. Stormer, and Philip Kim. Experimental observation of the quantum Hall effect and Berry's phase in graphene. *Nature*, 438(7065):201–204, 2005. doi: 10.1038/nature04235. URL https://doi.org/10.1038/nature04235.

[58] K. S. Novoselov, A. K. Geim, S. V. Morozov, D. Jiang, M. I. Katsnelson, I. V. Grigorieva, S. V. Dubonos, and A. A. Firsov. Two-dimensional gas of massless Dirac fermions in graphene. *Nature*, 438(7065):197–200, 2005. doi: 10.1038/nature04233. URL https://doi.org/10.1038/nature04233.

[59] M. Serlin, C. L. Tschirhart, H. Polshyn, Y. Zhang, J. Zhu, K. Watanabe, T. Taniguchi, L. Balents, and A. F. Young. Intrinsic quantized anomalous hall effect in a moiré heterostructure. *Science*, 367(6480):900–903, 2020. doi: 10.1126/science.aay5533. URL https://www.science.org/doi/abs/10.1126/science.aay5533.

[60] Jiaqi Cai, Eric Anderson, Chong Wang, Xiaowei Zhang, Xiaoyu Liu, William Holtzmann, Yinong Zhang, Fengren Fan, Takashi Taniguchi, Kenji Watanabe, Ying Ran, Ting Cao, Liang Fu, Di Xiao, Wang Yao, and Xiaodong Xu. Signatures of fractional quantum anomalous Hall states in twisted $MoTe_2$. *Nature*, 622(7981):63–68, 2023. doi: 10.1038/s41586-023-06289-w. URL https://doi.org/10.1038/s41586-023-06289-w.

[61] F. D. M. Haldane. Model for a quantum hall effect without landau levels: Condensed-matter realization of the "parity anomaly". *Phys. Rev. Lett.*, 61:2015–2018, Oct 1988. doi: 10.1103/PhysRevLett.61.2015. URL https://link.aps.org/doi/10.1103/PhysRevLett.61.2015.

[62] B. A. Bernevig, L. Fu, L. Ju, A. H. MacDonald, K. F. Mak, and J. Shan. Fractional quantization in insulators from hall to chern. *Nature Physics*, 21(11):1702–1713, 2025. ISSN 1745-2481. doi: 10.1038/s41567-025-03072-8. URL https://doi.org/10.1038/s41567-025-03072-8.

[63] T. Senthil and Michael Levin. Integer quantum hall effect for bosons. *Phys. Rev. Lett.*, 110:

046801, Jan 2013. doi: 10.1103/PhysRevLett.110.046801. URL https://link.aps.org/doi/10.1103/PhysRevLett.110.046801.

[64] Siddharth A. Parameswaran, Rahul Roy, and Shivaji L. Sondhi. Fractional quantum hall physics in topological flat bands. *Comptes Rendus Physique*, 14(9):816–839, 2013. ISSN 1631-0705. doi: https://doi.org/10.1016/j.crhy.2013.04.003. URL https://www.sciencedirect.com/science/article/pii/S163107051300073X. Topological insulators / Isolants topologiques.

[65] Anders S. Sørensen, Eugene Demler, and Mikhail D. Lukin. Fractional quantum hall states of atoms in optical lattices. *Phys. Rev. Lett.*, 94:086803, Mar 2005. doi: 10.1103/PhysRevLett.94.086803. URL https://link.aps.org/doi/10.1103/PhysRevLett.94.086803.

[66] M. Hafezi, A. S. Sørensen, E. Demler, and M. D. Lukin. Fractional quantum hall effect in optical lattices. *Phys. Rev. A*, 76:023613, Aug 2007. doi: 10.1103/PhysRevA.76.023613. URL https://link.aps.org/doi/10.1103/PhysRevA.76.023613.

[67] Julian Boesl, Rohit Dilip, Frank Pollmann, and Michael Knap. Characterizing fractional topological phases of lattice bosons near the first mott lobe. *Phys. Rev. B*, 105:075135, Feb 2022. doi: 10.1103/PhysRevB.105.075135. URL https://link.aps.org/doi/10.1103/PhysRevB.105.075135.

[68] Gregory Moore and Nicholas Read. Nonabelions in the fractional quantum hall effect. *Nuclear Physics B*, 360(2):362–396, 1991. ISSN 0550-3213. doi: https://doi.org/10.1016/0550-3213(91)90407-O. URL https://www.sciencedirect.com/science/article/pii/055032139190407O.

[69] Eyal Cornfeld and Eran Sela. Chiral currents in one-dimensional fractional quantum hall states. *Phys. Rev. B*, 92:115446, Sep 2015. doi: 10.1103/PhysRevB.92.115446. URL https://link.aps.org/doi/10.1103/PhysRevB.92.115446.

[70] Alexandru Petrescu, Marie Piraud, Guillaume Roux, I. P. McCulloch, and Karyn Le Hur. Precursor of the laughlin state of hard-core bosons on a two-leg ladder. *Physical Review B*, 96(1), July 2017. ISSN 2469-9969. doi: 10.1103/physrevb.96.014524. URL http://dx.doi.org/10.1103/PhysRevB.96.014524.

[71] Frank Schindler, Ashley M. Cook, Maia G. Vergniory, Zhijun Wang, Stuart S. P. Parkin, B. Andrei Bernevig, and Titus Neupert. Higher-order topological insulators. *Science Advances*, 4(6):eaat0346, 2018. doi: 10.1126/sciadv.aat0346. URL https://www.science.org/doi/abs/10.1126/sciadv.aat0346.

[72] Wladimir A. Benalcazar, B. Andrei Bernevig, and Taylor L. Hughes. Electric multipole moments, topological multipole moment pumping, and chiral hinge states in crystalline insulators. *Phys. Rev. B*, 96:245115, Dec 2017. doi: 10.1103/PhysRevB.96.245115. URL https://link.aps.org/doi/10.1103/PhysRevB.96.245115.

[73] Koji Kudo, Tsuneya Yoshida, and Yasuhiro Hatsugai. Higher-order topological mott insulators. *Phys. Rev. Lett.*, 123:196402, Nov 2019. doi: 10.1103/PhysRevLett.123.196402. URL https://link.aps.org/doi/10.1103/PhysRevLett.123.196402.

[74] Maria Lanaro, Lorenzo Maffi, and Marco Di Liberto. Emergent chiral Higgs mode in π-flux frustrated lattices, 2026. URL https://arxiv.org/abs/2601.08925. arXiv:2601.08925 [cond-mat.quant-gas].

[75] Phillip Weinberg and Marin Bukov. QuSpin: a Python package for dynamics and exact diagonalisation of quantum many body systems. Part II: bosons, fermions and higher spins.

SciPost Phys., 7:020, 2019. doi: 10.21468/SciPostPhys.7.2.020. URL https://scipost.org/10.21468/SciPostPhys.7.2.020.

[76] Wolfram Research, Inc. Mathematica, Version 14.3. URL https://www.wolfram.com/mathematica. Champaign, IL, 2025.

[77] Werner Krauth, Michel Caffarel, and Jean-Philippe Bouchaud. Gutzwiller wave function for a model of strongly interacting bosons. *Phys. Rev. B*, 45:3137–3140, Feb 1992. doi: 10.1103/PhysRevB.45.3137. URL https://link.aps.org/doi/10.1103/PhysRevB.45.3137.

[78] A. Rançon and N. Dupuis. Quantum xy criticality in a two-dimensional bose gas near the mott transition. *Europhysics Letters*, 104(1):16002, oct 2013. doi: 10.1209/0295-5075/104/16002. URL https://doi.org/10.1209/0295-5075/104/16002.

[79] Eslam Khalaf. Higher-order topological insulators and superconductors protected by inversion symmetry. *Phys. Rev. B*, 97:205136, May 2018. doi: 10.1103/PhysRevB.97.205136. URL https://link.aps.org/doi/10.1103/PhysRevB.97.205136.